Elucidating Structural Effects of Conjugated Polymers on Charge Transport and Durability for Organic Electronics and Development of Stretchable Semiconducting Materials

Viktoria Pakhnyuk

A dissertation

submitted in partial fulfillment of the

requirements for the degree of

Doctor of Philosophy

University of Washington

2019

Reading Committee:

Christine Luscombe, Chair

Matthew Bush

Alshakim Nelson

Program Authorized to Offer Degree:

Chemistry

University of Washington

Abstract

Elucidating Structural Effects of Conjugated Polymers on Charge Transport and Durability for Organic Electronics and Development of Stretchable Semiconducting Materials

Viktoria Pakhnyuk

Chair of the Supervisory Committee:
Professor Christine Luscombe
Department of Materials Science and Engineering

Understanding structure-property relationships of π-conjugated polymers is key to the development of functional materials for organic electronics. Molecular structure and polymer chain order strongly influence the electrical and mechanical performance of materials. First described is the theoretical and experimental quantification of polaron sizes in polythiophene polymers. Intramolecular and intermolecular charge delocalization length were studied to elucidate prior research relating polymer structure and packing morphology to electrical performance. Polythiophenes were also studied through the analysis of previously reported molecular dynamic simulations. Comparison of these models to experimental neutron scattering experiments revealed the requirement for updated parameters to accurately simulate polymer behavior. Polythiophenes are further described for the development of stretchable electronic materials. Improved compatibility in an elastomer/π-conjugated polymer composite was achieved by the introduction

of bromide functional groups. Functionalization led to altered intermolecular interactions and reactive covalent bonding which enhanced mechanical performance.

Table of Contents

List of Figures

List of Schemes

List of Tables

List of Equations

Acknowledgements

I would firstly like to thank my advisor Professor Christine Luscombe for your guidance and patience in my graduate studies. I am grateful for all the lab group members I had the opportunity to work with and the undergraduate researchers I had the joy of mentoring. Thank you to the research facility staff for your aid and responsiveness. Thank you also to the professors and laboratory technicians I grew with during my years of teaching. I am thankful for the many resources and opportunities that were offered by the University of Washington.

I would like to recognize all the collaborators for your work and effort. Thank you to Annabel Chew, Raja Ghosh, Emily C. Davidson, and professors Frank Spano, Alberto Salleo, and Rachel Segalman for your contributions to the polaron research projects. Thank you to Caitlyn Wolf, Kiran Kanekal, Yeneneh Yimer, Madhusudan Tyagi, Souleymane Omar-Diallo, and professors Jim Pfaendtner and Lilo Pozzo for your contributions to the molecular dynamics and neutron scattering research.

I would like to thank the mentors I had in my undergraduate studies who provided early exposure to research. Thank you to my mentor Delwin Elder, and advisors Professor Larry Dalton and Dr. Werner Kaminsky as well as mentor Benjamin Leipzig and Professor Julia Kovacs for the impactful undergraduate research experience.

I must also recognize all the meaningful relationships I formed in my time at Highline College. Thank you to Rich Bankhead, Barbara Clinton, Heather Price, Steve Marfiak, Jeff Owens, and Dusty Wilson for your faith in me.

Finally, I would like to acknowledge the support and influence of my family, friends and church. Your prayers and encouragement were instrumental to keep me going. I am especially grateful for my closest friends who were able to listen, empathize, and cheer me on during the ups and downs.

DEDICATION

This dissertation is dedicated to my dad, the best friend I lost too soon

Vasil Pakhnyuk

(1954-2017)

I would not have made it this far if it was not for your encouragement, wisdom and humor.

Until we meet again.

Miss you.

Introduction to Structure-Property Relationships of π-Conjugated Polymers

π-Conjugated polymers are attractive candidates to utilize in electronics because they are solution-processable, lightweight, and structurally modular.[1] Most notably, simple and inexpensive processing gives them greater potential for scaled manufacturing compared to traditional inorganic devices which require complex and expensive fabrication techniques.[2,3] One of the attractive aspects of π-conjugated polymers is their ability to tune properties by modifications in the chemical structure, which can be achieved by alteration of the adjacent solubilizing side chain.[4–6] In this work, we focus on polythiophene π-conjugated backbones and study the electrical and mechanical properties correlating to different side chain structures. Polymers discussed in this work include poly(3-hexylthiophene), poly(3-(2′-ethyl)hexylthiophene), poly(3-(6-mercaptohexylthiophene)) and poly(3-(6-bromohexylthiophene). (**Figure 1**).

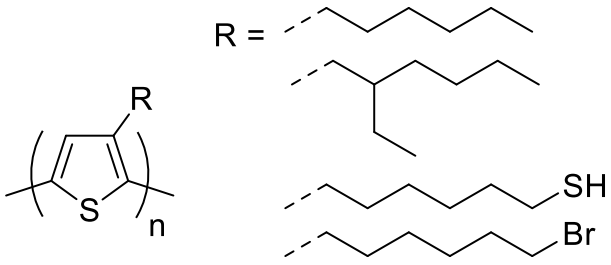

Figure 1*: Polythiophene backbone discussed in this work with hexyl, 2-ethylhexyl, 6-mercaptohexyl and 6-bromohexyl side chains.*

In addition to the structure of the side chain, the regioregularity - the relative positioning of the side chain on the thiophene ring, is an important consideration since it is also reflected in charge mobility (**Figure 2**). Highly regioregular poly(3-hexylthiophene) (P3HT) containing primarily head-tail coupling lends a charge mobility of ~10^{-2} cm^2 V^{-1} s^{-1}, while regiorandom polymers have drastically lower charge mobilities on the order of 10^{-6} cm^2 V^{-1} s^{-1}.[7–10] This stems from more planar conformation of the regioregular polymer

which allows for greater charge transport across the material through more ordered and interconnected packing morphology .[10]

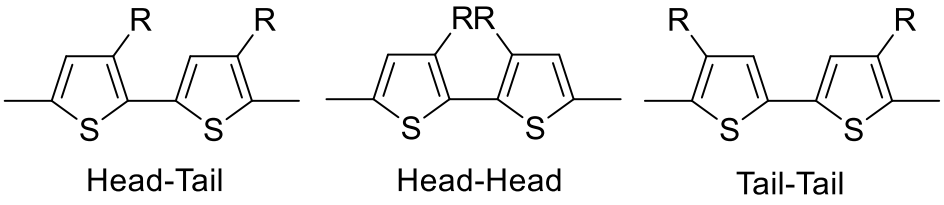

Figure 2: Possible coupling of thiophene monomers, where highly regioregular polymers have predominantly head-tail orientation.

Along with side chain structure and regioregularity, the molecular weight of polythiophenes is also known to affect electrical performance, with greater charge mobility for longer chains.[11–16] It was thus critical to prepare quality samples with controlled and narrow molecular weight distributions. This was regulated by nickel catalyzed polymerization to yield targeted molecular weights with high regioregularity.[17,18] Side chain structure, regioregularity and molecular weight were three factors considered for the synthesis and experimentation of polythiophenes.

The work presented herein has three main focuses. First, the direct measure of polaron size is presented computationally and experimentally for several polythiophenes. A polaron is an induced charge that is coupled to its distorted lattice over a given area and is a dominant influence of charge transport in π-conjugated polymers.[19–24] The polarons allow π-conjugated polymers to generate charge flow intramolecularly along a polymer backbone and intermolecularly across multiple polymer chains (Figure 3). Charge induced by the presence of chemical dopants produces bound polarons which are confined in size due to charge interactions.[25,26] Alternatively, unbound polarons, which are larger in size, are induced either optically or electrically, the latter of which is discussed here.[26,27] The author contributed to this collaborative research through the synthesis of polymers. Key findings are reported, while further details can be found

in their respective publications.[28,29] The bound and unbound polaron sizes presented herein supplement the known effects of P3HT packing arrangements on charge mobility.[9–13,30,31]

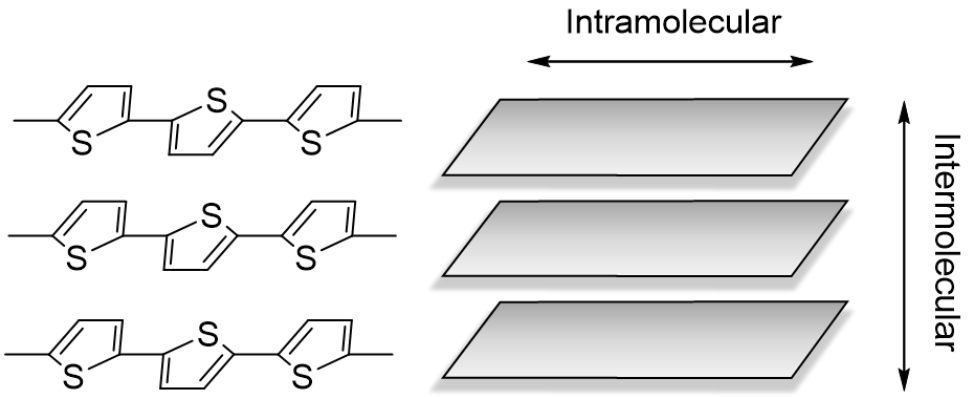

Figure 3: Diagram of intramolecular and intermolecular interactions in polythiophenes.

The second focus in this work lies in the assessment of reported molecular dynamics simulations for poly(3-hexylthiophene). Computations representative of experimental behavior of the conjugated polymer are necessary in order to study its detailed electrical behavior accurately. Existing models were evaluated against the gathered experimental x-ray and neutron scattering data, and inconsistencies between models were identified. This research highlights the need for improved P3HT modeling parameters, especially in the π-conjugated backbone which is responsible for electrical performance.

The last focus of this thesis applies side chain functionalization for the development of stretchable electronic materials. For the project, side chain modification was used to improve the mechanical durability in a composite polymer blend, which consists of a π-conjugated polymer and elastomer. This approach uses side chains to alter packing within the semiconducting polymer to affect its interaction with the elastomer. Furthermore, the functional group is used to chemically bond to the elastomer and strengthen the composite's resistance to strain-induced cracking. The combination of altered polymer packing and chemical bonding showed significant improvement in the composite's crack onset strain, while also retaining electrical conductivity comparable to the neat π-conjugated polymer.

1: Theoretical and Experimental Determination of Polaron Coherence Lengths in Polythiophenes

1.1 Background and Motivation

The goal of this project was to isolate and quantify local polaron delocalization under an applied electric field. This work studied known polythiophenes to describe the origins of each material's charge mobility. Polaron delocalization occurs in the intramolecular (1D) direction along the conjugated backbone and in the intermolecular (2D) direction across π-π stacks between polymer chains (**Figure 3**). The studied polymers each have a distinct packing assembly influenced by structure of the side chain. Regioregular polymers have identical or nearly identical monomer orientation, whereas regiorandom polymers bond with varying positioning of the side chain. To compare 1D and 2D delocalization, three polymers chosen for study: regiorandom poly(3-hexylthiophene) (RRa P3HT), poly(3-(2'-ethyl)hexylthiophene) (P3EHT), and regioregular poly(3-hexylthiophene) (RR P3HT) (**Figure 4**). RR P3HT was studied with a series of molecular weights, 3.6-30 kg/mol, since its charge mobility is strongly correlated with molecular weight. Furthermore, a RR P3HT sample was tested without the use of a self-assembled monolayer (SAM) to modify the substrate surface, which is widely used to enhance charge mobility in organic field-effect transistors (OFETs).

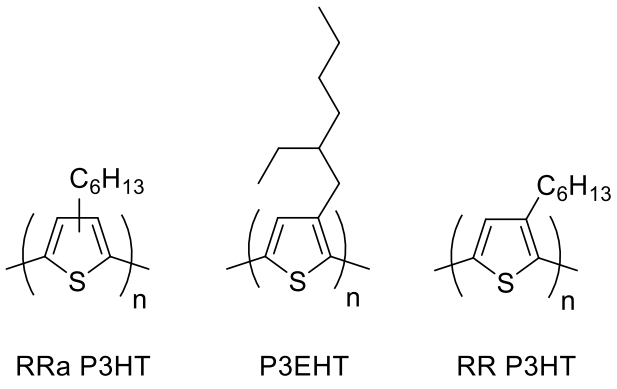

Figure 4: Polythiophene structures examined for polaron delocalization.

Computational modeling was performed for the polythiophenes to calculate 1D and 2D polaron lengths. Experimental work was executed by charge modulation spectroscopy (CMS) which directly measures polaron absorption in a configuration identical to OFETs. Polaron delocalization for each of the polythiophenes was represented throughout by the polaron coherence number, N, reported as the number of thiophene monomer units (Table 1). This number was compared to each sample's persistence length, the length over which a polymer retains a similar backbone vector. Stiffer polymers are better aligned over longer distances and have higher persistence lengths, while flexible chains are aligned over shorter distances and have smaller persistence lengths. N was also compared to the coherence lengths of the corresponding polythiophenes, which is the size of polymer crystallites. Together, this information was used to quantitively depict the polaron delocalization length to each polythiophene and relate this to its packing structure and charge mobility.

Table 1: Intramolecular and intermolecular polar coherence lengths (N) of polymer samples reported in number of thiophene monomer units.

Polymer	**N_{intra}**	**N_{inter}**
RRa P3HT	3	-
P3EHT	4.8	1.1
RR P3HT 3.6 kg/mol	4.5	1.9
RR P3HT 6.7 kg/mol	5.1	2.0
RR P3HT 12.6, 20, 30 kg/mol	5.2	5.0
RR P3HT w/o SAM 30 kg/mol	4.8	1.8

1.2 Results and Discussion

1.2.1 Regiorandom Poly(3-heylthiophene)

RRa P3HT is a highly disordered CP with low charge mobility (10^{-6} cm^2 V^{-1} s^{-1}).[32] Its disorder is indicated by UV-vis spectroscopy where films have very similar absorption to solutions without aggregate peaks to suggest organized solid polymer arrangement.[33] Due to the low absorption of RRa P3HT by CMS, computational work was instead fit to its photoinduced absorption (PIA) spectrum.[34] Computational work calculated N_{intra} to be ~3 thiophene monomers localized to a single chain. This length of 0.8 nm is near the polymer's 1 nm persistence length.[35] It is concluded from this data that the polaron size in RRa P3HT is restrained by polymer conformation, limiting its charge mobility.

1.2.2 Poly(3-(2′-ethyl)hexylthiophene)

P3EHT is more ordered than RRa P3HT, yet produces a low charge mobility (10^{-5} cm^2 V^{-1} s^{-1}) not significantly greater than RRa P3HT.[36] The polymer arranges in a herringbone structure with longer π-π stacking distance between chains due to the steric hindrance of side chains.[4] RR side chains of P3EHT lead to semicrystalline packing as demonstrated by x-ray diffraction patterns.[4] Computational work quantified N_{intra} to be ~5 monomers in length, (1.6 nm) and a N_{inter} of ~1 monomer which agrees with experimental CMS data (**Figure 5**). These results show that the increased order of P3EHT led to a substantially higher N_{intra} than RRa P3HT but was still localized to a single chain. P3EHT's N_{intra} is lower than its persistence length of 3.1 nm and its thickness-dependent coherence length of 6-10 nm.[35,36] This denotes that other defects in the polymer landscape must be reducing polaron delocalization. The low charge mobility of P3EHT despite its larger N_{intra} and improved packing order, is attributed to its lack of interchain polaron delocalization.

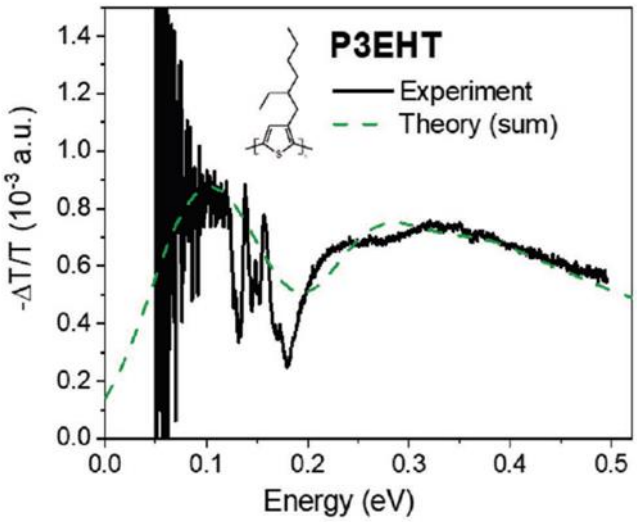

Figure 5: Overlay of theoretical and experimental CM spectra of P3EHT. Reprinted with permission.[28] Copyright 2019 Wiley.

1.2.3 Regioregular Poly(3-hexylthiophene)

The last polymer structure examined was RR P3HT, which has a moderate to high charge mobility (up to 10^{-2} cm^2 V^{-1} s^{-1}).[11] Its charge mobility is known to depend the polymer's molecular weight, which increases charge mobility with longer chains.[11,15,12] Like P3EHT, RR P3HT is semicrystalline, as observed by AFM and x-ray diffraction, with more crystallinity detected for shorter polymers.[11–13] Computational work coupled with experimental CMS data quantified a N_{intra} of ~5 for all molecular weights. A N_{inter} of ~2 was calculated for lower molecular weights which increased to ~5 for molecular weights 12.6 kg/mol and above. While, P3EHT and RR P3HT have very similar N_{intra}, the substantially larger N_{inter} of RR P3HT here is shown to contribute to its much higher charge mobility, which can delocalize across multiple chains due to closer π-π stacking.[31,37] Interestingly, though the size of polarons levels off beyond 12.6 kg/mol, charge mobility of RR P3HT still increases with greater molecular weight (**Figure 6**).[11,15] This is understood to be because of tie chains, connecting polymer chains that link crystallites and increase charge mobility.[38] This work shows

that increased N strongly influences charge mobility for shorter chains but is not the reason for increased charge mobility for molecular weights >12.6 kg/mol.

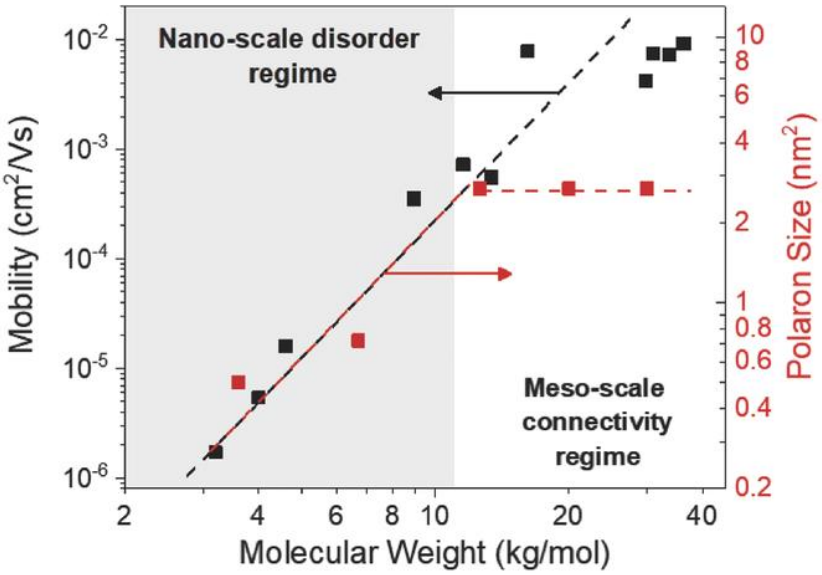

Figure 6: Plot of RR P3HT charge mobility and polaron size as a function of molecular weight. Reprinted with permission.[28] Copyright 2019 Wiley.

All films to this point have been applied onto an octadecyl SAM on the substrate. Surface modification is frequently implemented to improve charge mobility of OFETs, however, its origin has not been well understood. A sample without this SAM was test for 30 kg/mol RR P3HT. Experimental and computational CM spectra of these films showed a decrease in N_{intra}, and especially N_{inter} by excluding the SAM (Figure 7). For the first time, this shows that substrate modification improves charge mobility because of increased polaron size at the substrate interface.

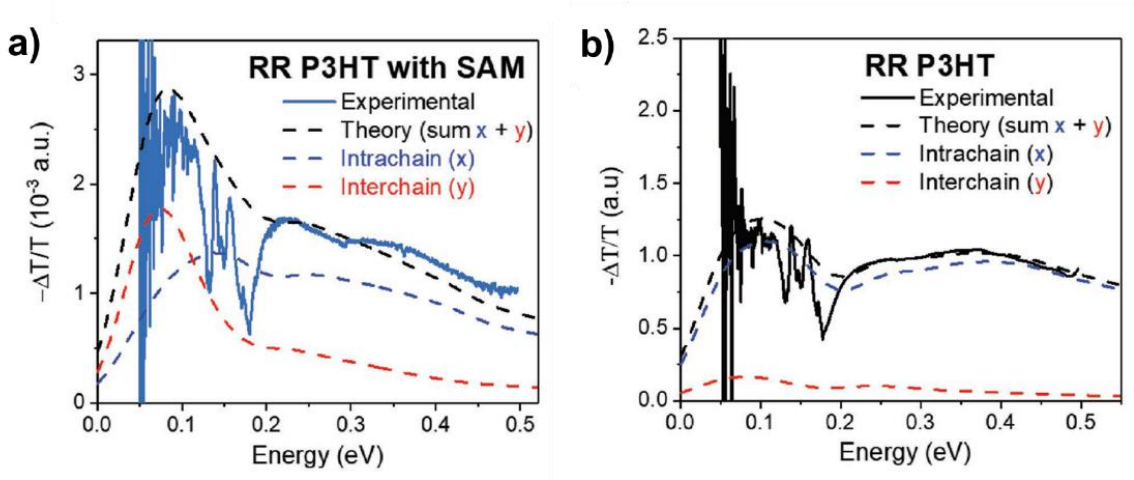

Figure 7: Experimental and theoretical CM spectra of 30 kg/mol RR P3HT deposited on a substrate (a) with and (b) without a SAM. Reprinted with permission.[28] Copyright 2019 Wiley.

1.3 Conclusion

This work examined polaron delocalization of RRa P3HT, P3EHT, RR P3HT and related it to each polymer's distinct polymer packing and charge mobility. Data was compared computationally and experimentally by CMS which produces charge by an applied electric field. While improved backbone order from RRa P3HT to P3EHT increased N_{intra}, charge mobility remained low. An increase in both N_{intra} and N_{inter}, however was demonstrated to substantially increase charge mobility, as depicted by RR P3HT. Because RR P3HT is highly dependent on chain length, N was also investigated for molecular weights 3.6-30 kg/mol. N_{intra} was unchanged while N_{inter} increased with molecular weight only up to 12.6 kg/mol, indicating that charge mobility increase at higher chain lengths was not due to polaron size. Furthermore, it was found that hydrophobic surface modification by a SAM improved charge mobility through larger N_{inter} at the substrate interface. Overall, the quantification of N by both theoretical and experimental methods in this work confirms that the charge mobility of semiconducting polymers is dependent on polaron size.

2: Decoupling Intramolecular and Intermolecular Infrared Polaron Absorption in Doped Poly(3-hexylthiophene)

2.1 Background and Motivation

In this work, we study the IR absorption of RR P3HT chemically doped by 2,3,5,6-tetrafluoro-7,7,8,8-tetracyanoquinodimethane (F4TCNQ) and deconvolute the IR polaron absorption to its intramolecular and intermolecular components (**Figure 3**). This is done by first simulating different effects on the absorption spectrum and then comparing to experimental absorption of RR P3HT. Simulations were tested for multiple variables to study its effects on IR absorption and polaron size. These include the dopant distance and relative position to the polymer, effects of polymer length, as well as comparison of bound (chemically doped) and unbound (electrically or optically doped) polarons. Similar to previous work, the size of the polarons is defined by the polaron coherence number, N, reported as the number of consecutive thiophene monomers. N_{coh} is defined as the coherence "area," which is approximately the product of N_{intra} and N_{inter}.

The polaron IR absorption of P3HT in question here are two peaks at 0.1-0.15 eV (800-1200 cm^{-1}) and 0.35-0.7 eV (2800-5600 cm^{-1}), which will be referred to as peaks A and B, respectively. Peak A is narrower, less intense and overlaps with IR-active bond vibrations, while peak B is broader and more intense. Originally, peak A was assigned to the interchain polaron absorption and peak B the intrachain polar absorption.[39,40] However, this is contradicted by the presence of peak A in RRa P3HT, unaggregated P3HT, and P3HT electrically doped in the intramolecular direction.[34,41,42] Peak A can also "borrow" from peak B by the Herzberg–Teller coupling as described elsewhere.[43] Here we distinguish the contribution of intramolecular and intermolecular absorption to both of these peaks for chemically doped P3HT. Greater delocalization of polarons is influenced by more organized polymer conformation,[22,34] and further dopant distance[44,45] which is reflected in the redshift and intensity of peaks A and B.

2.2 Results and Discussion

2.2.1 Theoretical Studies

In the first simulation, a varying anion dopant distance is simulated for 10-mer P3HT containing one hole (**Figure 8**). The dopant was positioned in plane with the 10-mer at the midpoint of the chain between the 5th and 6th monomers. It is worth noting that simulations used a point charge and that an anion distance (d_{anion}) of at least 0.4 nm presents a more accurate simulation since F4TCNQ has a delocalized charge. Positioning the anion directly across a thiophene rather than the midpoint yielded only minor differences for $d_{anion} > 0.5$ nm. The simulated IR spectra shows that both peaks A and B were present for $d_{anion} \geq 0.6$ nm (**Figure 9**). As the distance increased, both peaks presented peak growth and redshift. These calculations show that moving the dopant further away from the chain leads to larger polarons on P3HT. An infinite distance was also tested to represent an unbound polaron. For this simulation, both peaks A and B are depicted. This demonstrates that both IR peaks are present through any charge induction method, and neither peak is assigned entirely to the presence of a bound polaron.

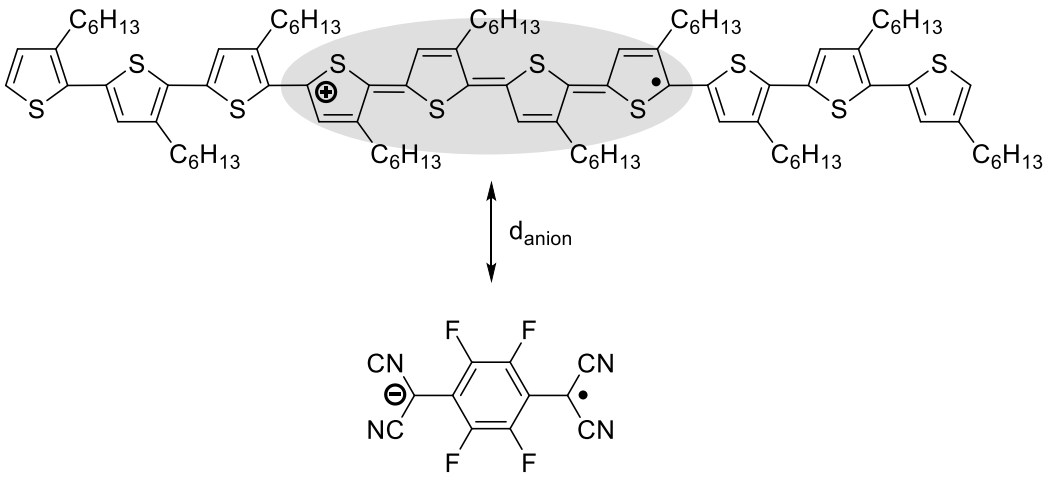

Figure 8: Structural simulation of RR 10-mer P3HT doped by F4TCNQ with increasing dopant distance (d_{anion}). The shaded region depicts polaron coherence number (N_{coh}) delocalized over P3HT.

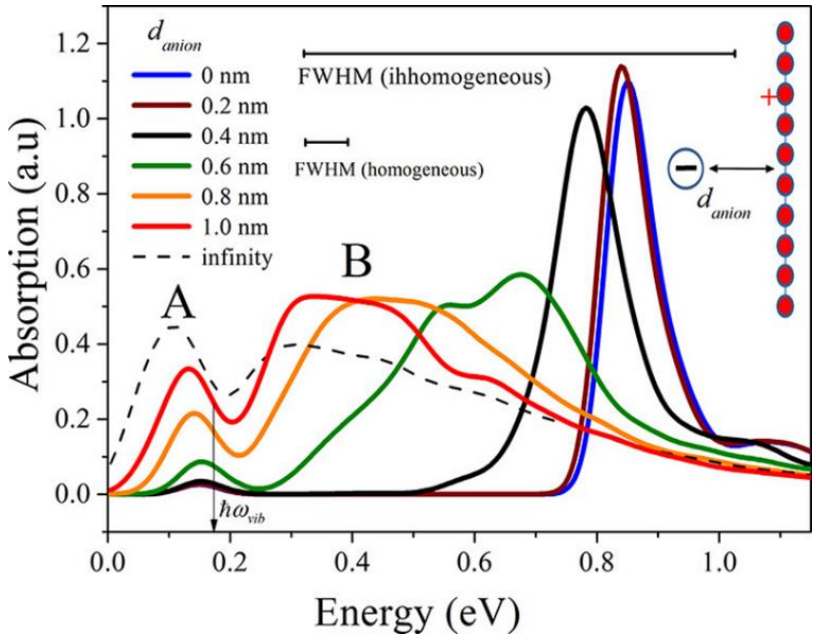

Figure 9: Simulated polaron IR spectra of doped P3HT with increasing dopant distance (d_{anion}) shown at right inset. Reprinted with permission.[29] Copyright 2019 American Chemical Society.

N_{coh} was also extracted from the simulations of varying d_{anion} (Figure 10). Near the P3HT chain, the polaron delocalized over ~2 monomers. As d_{anion} increased, N_{coh} reached ~5 monomer units, which leveled off at distances beyond 1.5 nm. From this information, we can conclude that the intensity growth and redshift of peaks A and B in the IR spectrum are directly related to the polaron size, which is dependent on dopant distance.

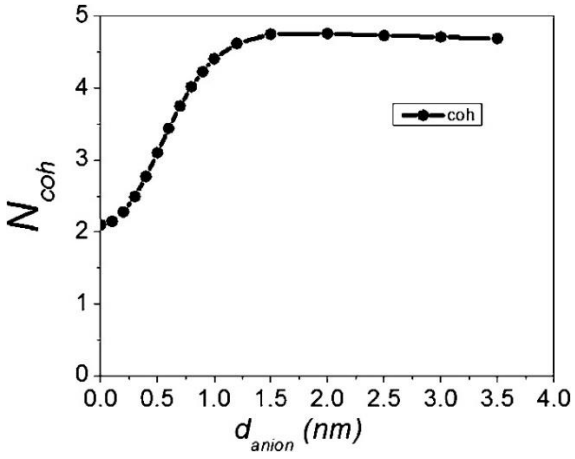

Figure 10: Polaron coherence number (N_{coh}) as a function of dopant distance (d_{anion}). Reprinted with permission.[29] Copyright 2019 American Chemical Society.

The next simulation explored changes in the IR spectrum and N_{coh} as the length of P3HT increased from 2 to 10 monomers (**Figure 11**) where $d_{anion} = \infty$. With longer P3HT, peaks A and B became more intense and redshifted, similar to the previous simulation. N_{coh} also increased with polymer length up to an 8-mer, from an area covering ~2 thiophenes up to ~5. Beyond 8 thiophenes, the IR absorption and N_{coh} remained constant. These results indicate that the delocalization of the polarons is dependent not only on dopant distance but also the length of P3HT, which is unchanged by a length longer than 8 monomer units.

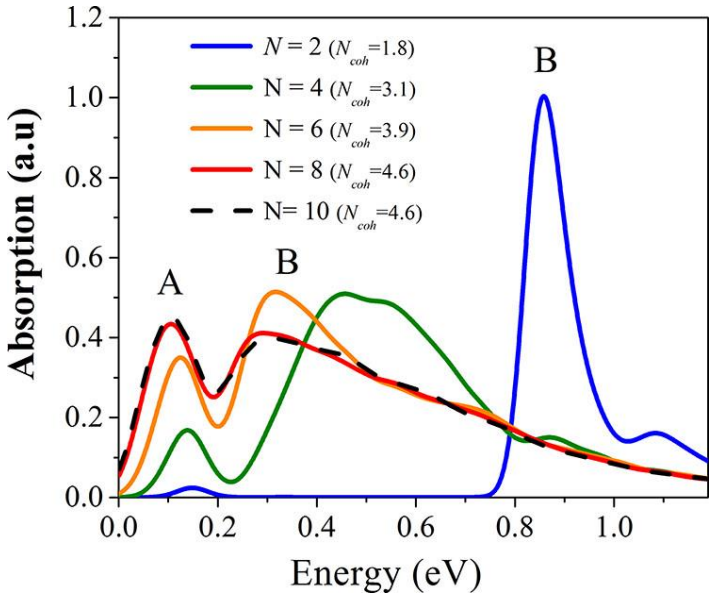

Figure 11: Simulated polaron IR spectra of doped P3HT as a function of increasing polymer length. Reprinted with permission.[29] Copyright 2019 American Chemical Society.

The next simulation studied the absorption in 5 stacks of 10-mer P3HT for bound (chemically doped) and unbound (electrically and optically doped) polarons. Calculations simulated the IR spectra and N_{coh}, which was divided into intramolecular and intermolecular polaron coherence numbers, N_{intra} and N_{inter} (Figure 12). As before, the anion was positioned at a constant distance in the plane of the stacks at the midpoint of the chains. Placing the anion above the plane of the stacks had minimal changes to final spectra. In both bound and unbound simulations, intrachain delocalization contributed to the absorption more than interchain delocalization with $N_{intra} > N_{inter}$. In the bound polaron case, the spectrum consisted almost exclusively of the intrachain polaron absorption with peak B more intense than peak A. The reverse was true in the unbound case, where peak A was more intense than peak B. Polaron sizes were quantitatively compare, with a N_{coh} of 16.6 for the unbound case, which is almost 3 times larger than the bound N_{coh} of 5.95. N_{intra} of 5.03 and N_{inter} of 2.75 for the unbound simulation are markedly larger than for the bound case. The bound polaron was localized to a single with a N_{intra} of 3.80 and N_{inter} of 1.47. The small

intermolecular polaron span of the doped P3HT coincides with experimental records which require high dopant concentrations to induce sufficient bulk charge transfer.[46]

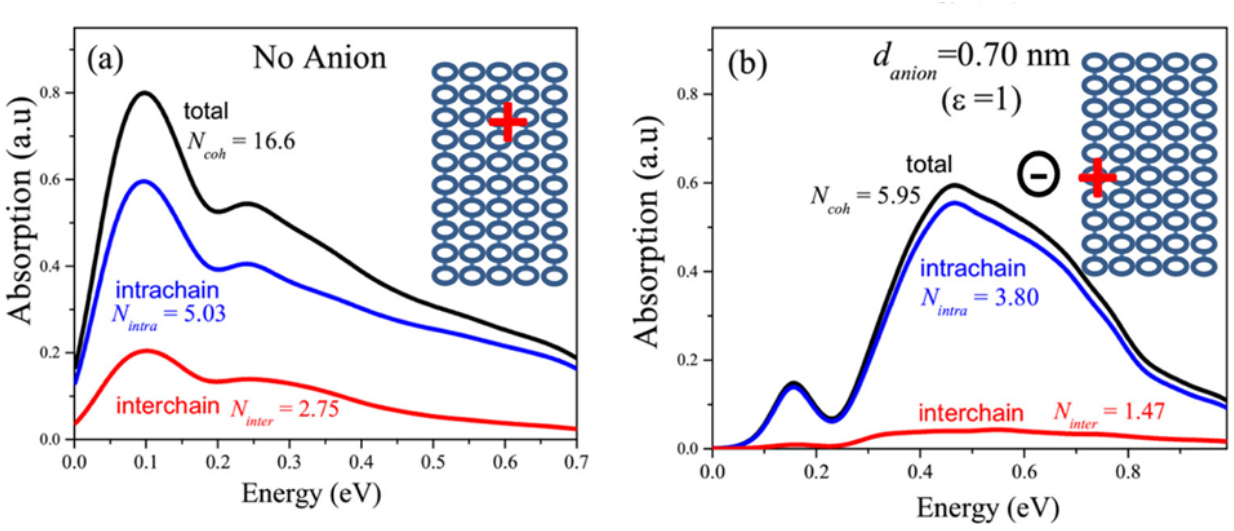

Figure 12: Simulated polaron IR absorption for (a) unbound and (b) bound polarons in 5x10-mer P3HT as shown in right insets. Reprinted with permission.[29] Copyright 2019 American Chemical Society.

2.2.2 Experimental Analysis

All of the simulations were used to determine parameters for fitting experimental IR absorbance spectra of F4TCNQ-doped P3HT and to calculate N_{intra} and N_{inter}. Experimental spectra were first examined for low molecular weight 3.6 kg/mol P3HT (**Figure 13**). This experimental spectrum shows a substantially larger peak B than peak A, comparable to the bound polaron simulation. The fit for this spectrum was performed similar to previous simulations using 5 10-mer stacks containing one hole with an anion placed in the plane of the stacks. The full spectrum revealed a fit of more than d_{anion}, at 0.50 nm and 0.85 nm from the stack in a 3:1 ratio. The two distances are thought to originate from P3HT polymorphs, where P3HT organizes with either with or without interdigitated side chains.[47] At both distances, polarons are localized to the chain with N_{inter} of 1.27 for the nearer 0.50 nm d_{anion} and 1.64 for the further 0.85 nm d_{anion}. Overall, delocalization was greater for the further anion with a N_{coh} of 7.60 (N_{intra} = 3.11), compared to a N_{coh} of 4.09

(N_{intra} = 4.27) for the nearer d_{anion}. The experimental IR absorption of doped P3HT demonstrates that the spectrum results from a combination of anion distances from P3HT.

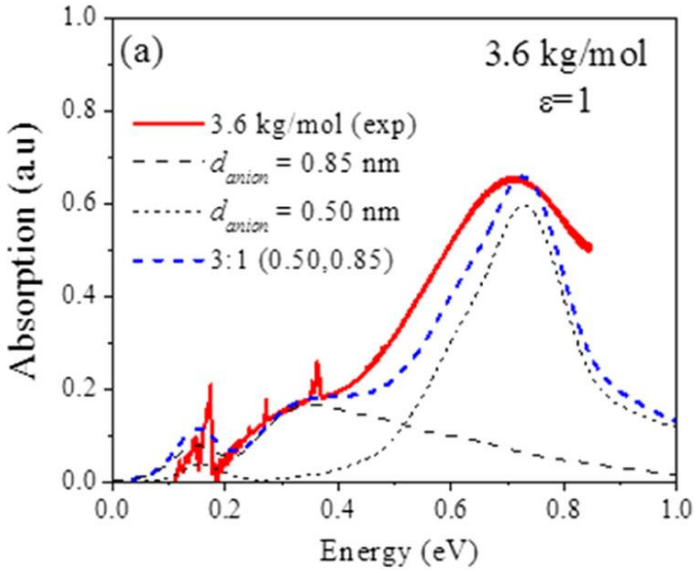

Figure 13: Experimental IR spectrum of 3.6 kg/mol RR P3HT with fitted absorption consisting of two d_{anion}. Reprinted with permission.[29] Copyright 2019 American Chemical Society.

An experimental spectrum was also studied for doped high molecular weight of 30 kg/mol P3HT (Figure 14). When compared to 3.6 kg/mol P3HT, peak A for 30 kg/mol P3HT is more intense, though still smaller than peak B. The large peak B indicates a bound polaron, in agreement with simulation. The considerable redshift of peak B for the high molecular weight P3HT indicates larger d_{anion} as calculated theoretically. Similar to the 3.6 kg/mol P3HT, the fit of the 30 kg/mol P3HT also consisted of more than one d_{anion}. The fit here consisted of two anion distances, 0.70 nm and 1.1 nm in a 2:1 ratio, nearly doubling d_{anion} of low molecular weight P3HT. The larger d_{anion} is likely derived from high molecular weight P3HT packing that excludes dopant molecules.[42,48] The average N_{coh} of 7.35 for 30 kg/mol P3HT is greater than the low molecular weight average, and similar to the larger d_{anion} of 3.6 kg/mol P3HT. The doped P3HT polaron at 30 kg/mol is still bound to a single chain with a N_{inter} of 1.62 but is spread over a larger area in the intramolecular direction with a N_{intra} of 4.04.

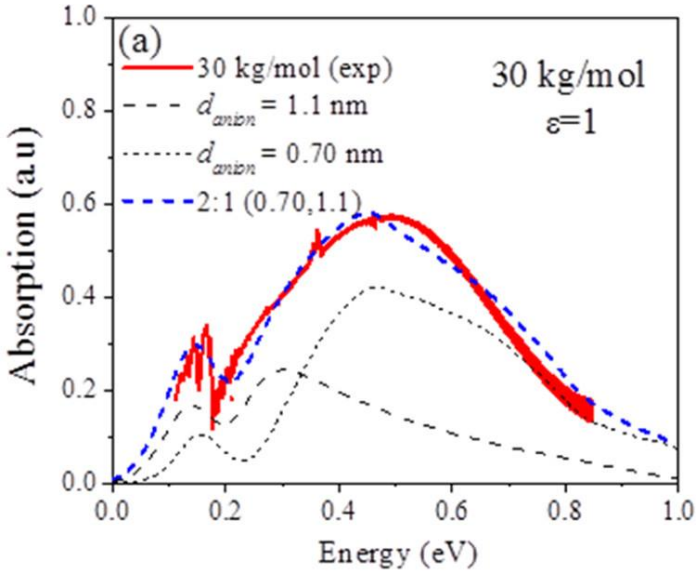

Figure 14: Experimental IR spectrum of 30 kg/mol RR P3HT with fitted absorption consisting of two d_{anion}. Reprinted with permission.[29] Copyright 2019 American Chemical Society.

2.3 Conclusion

In this report, experimental polaron IR absorption was fit to theory to explain the origins of peaks A and B. It was found that for chemically doped P3HT, both peaks arise primarily from intrachain polaron absorption, which is more delocalized, rather than the interchain polarons, which are limited to a single chain. Simulations found that the polaron coherence number, N, increased with the anion distance, d_{anion} up to 1.5 nm, after which N_{coh} leveled off. This was reflected in simulated IR spectra with the growth of peak A and redshift of peak B. Simulations also showed that increasing the P3HT length up to an 8-mer led to larger N, which was similarly reflected in the IR. It was also found computationally that peak B intensity is greater than peak A when polarons were bound by the dopant. Experimentally, IR spectra of doped P3HT presented a redshift of peak B for high molecular weight P3HT (30 kg/mol), indicating greater polaron delocalization than low molecular weight P3HT (3.6 kg/mol). Both high and low molecular weight P3HT were a combination of two d_{anion} which corresponding to known polythiophene polymorphs. IR spectra was also accompanied by calculations indicating greater N and d_{anion} of high molecular weight P3HT in

agreement with theory and known charge mobility trends. The theoretical and experimental quantification of these results supplement previous works relating P3HT performance to its packing structure.

3: Analysis of Poly(3-hexylthiophene) Molecular Dynamics Simulations and Evaluation by Experiment

3.1 Background and Motivation

The goal of this work was to assess a few existing models that computationally simulate a conjugated polymer and compare them to experimental measurements. The use of accurate molecular dynamics is important in order to develop a more detailed understanding of the local charge transport in electronic polymers. However, these models are only useful if they are validated by experiment, and limited studies have explored both simulations and experiment of conjugated polymers side by side.[49–57] This research assesses simulations by Moreno *et al.,* Huang *et al.*, and Bhatta *et al.* which apply varying parameters for their force fields.[58–60] These models were compared to each other and to the experimental wide angle x-ray scattering (WAXS) and quasi-elastic neutron scattering (QENS) data presented herein. The findings show that further developments are needed for accurate simulations, particularly in the π-conjugated backbone segment.

Poly(3-hexylthiophene) (P3HT) is an exemplary structure in the field of organic electronics and was selected for this study. While regioregular P3HT has improved electrical performance over regiorandom P3HT, it is also more complicated morphologically containing both amorphous and crystalline packing. Regiorandom P3HT, on the other hand, is a fully amorphous polymer. Furthermore, regiorandom (RRa) P3HT packing and performance does not exhibit the same dependence on other factors such as molecular weight and processing conditions like regioregular P3HT and was a more appropriate choice for the work.

3.2 Results and Discussion

3.2.1 Simulation and Experiment Comparison

Experimental data was gathered for RRa P3HT with either a hydrogenated or deuterated side chain. Simulations used structures with average length and regioregularity of experimental sample polymers. Of the models considered, the Bhatta force field were modified in this study to correct for a more flexible alkyl side chain. The Moreno model includes 3 force fields with different atomic parameters. Detailed experimental and computational procedures may be found in the respective publication.[61]

The first assessment was executed for hydrogenated RRa P3HT by comparing the static structure factor, *i.e.* x-ray scattering pattern, of experimental WAXS data to molecular dynamics simulations. All models – the modified Bhatta force field, Huang force field and the 3 Moreno force fields – displayed reasonable agreement with the experimental peak location and intensity over the tested temperatures (Table 2). Peak 1 is ascribed to the intermolecular distance between thiophene rings and peak 2 is attributed to the distance between adjacent alkyl side chains, both appearing broad due to the lack of long range order in RRa P3HT.[62,63] Because of the similarity and agreement between the data sets, it was necessary to compare models in more detail by other experimental methods.

Table 2: Comparison of WAXS peak location of 5 force fields to experiment across 3 temperatures. Reproduced with permission from the Royal Society of Chemistry.[61]

	Peak location 1 ($Å^{-1}$)			Peak location 2 ($Å^{-1}$)		
Simulation force field	273 K	373 K	473 K	273 K	373 K	473 K
Experimental	0.38	0.39	0.39	1.46	1.36	1.30
Moreno FF1	0.45	0.44	0.42	1.45	1.39	1.34
Moreno FF2	0.45	0.44	0.42	1.43	1.41	1.35
Moreno FF3	0.47	0.45	0.42	1.45	1.40	1.34
Huang	0.45	0.43	0.42	1.47	1.42	1.36
Mod. Bhatta	0.42	0.40	0.38	1.46	1.41	1.36

To further analyze the simulated force fields, experimental data was gathered by QENS to provide molecular information about the polymer at scales comparable to molecular dynamics. Data was gathered for two RRa P3HT polymers, taking advantage of isotope labeling with either a hydrogenated or deuterated side chain. Hydrogen is sensitive to QENS and its replacement with deuterium in the alkyl side chain reduces its scattering signal from 93% down to 25%. The allows us to isolate the contributing signals of the π-conjugated thiophene backbone which does not have classical behavior like the alkyl side chain due to its charge transport capabilities. Movement in the polymers was quantified by the mean square displacement (MSD) and compared to QENS data across temperature ranges from 50 K to 523 K. All simulations had reasonable agreement with experiment for the fully hydrogenated sample. Beginning at 50 K, there is a steady increase in the motion of the polymer as temperature increases. On the other hand, all simulations had poor fit to the experimental signals of the deuterated sample. Simulations overestimated the contribution of the thiophene, showing steady increase in motion that is similar but smaller than the hydrogenated sample. Experimental data instead revealed an increase in movement only after temperatures of at least 400 K were reached. This demonstrates that the motions of the thiophene backbone are distinct from the side chain, and that force field parameters must be modified to accurately reflect P3HT behavior for clearer modeling of P3HT behavior.

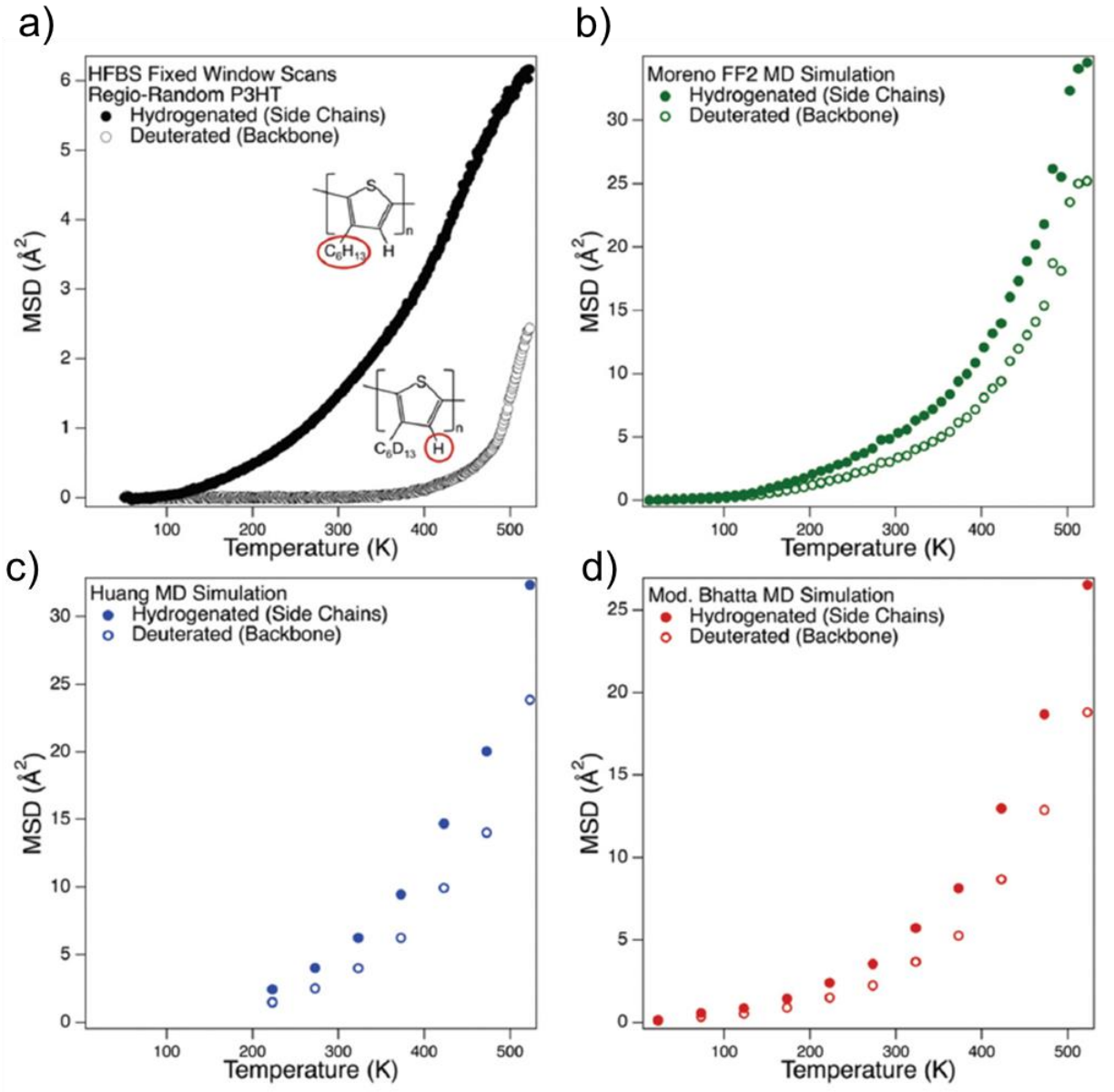

Figure 15: (a) Experimental QENS and simulations from (b) Moreno FF2, (c) Huang, (d) modified Bhatta force fields of RRa P3HT samples containing hydrogenated or deuterated side chain. Reproduced with permission from the Royal Society of Chemistry.[61]

3.2.2 Analysis of Computational Models

The Moreno, Huang, and modified Bhatta force fields were compared to each other to mark parameter variation and their effects in structural simulations for RRa P3HT. One assessment is of the

torsion potentials, or the energies associated with different dihedral angles in the polymer. First, dihedral angles labeled β_1-β_5 were analyzed, which lie in the carbon bonds along the alkyl side chain (**Figure 16a**). All models agree on the β_2-β_5 torsion potentials, which mimic polyethylene, but show discrepancies in the β_1 torsion potential adjacent to the thiophene (**Figure 16b**). The Huang force field shows negligible energy barriers for β_1, while Moreno exhibits potentials similar but less intense than polyethylene. The modified Bhatta force field gives preference to dihedral angles that are different from the other models, with an energy valley near 90° in contrast to 60°. From these comparisons, it is evident that the parameters of each force field yield different torsion potentials for the side chain. Such differences are important to consider since they influence the computation for electrical properties and lead to varying results depending on the method chosen.

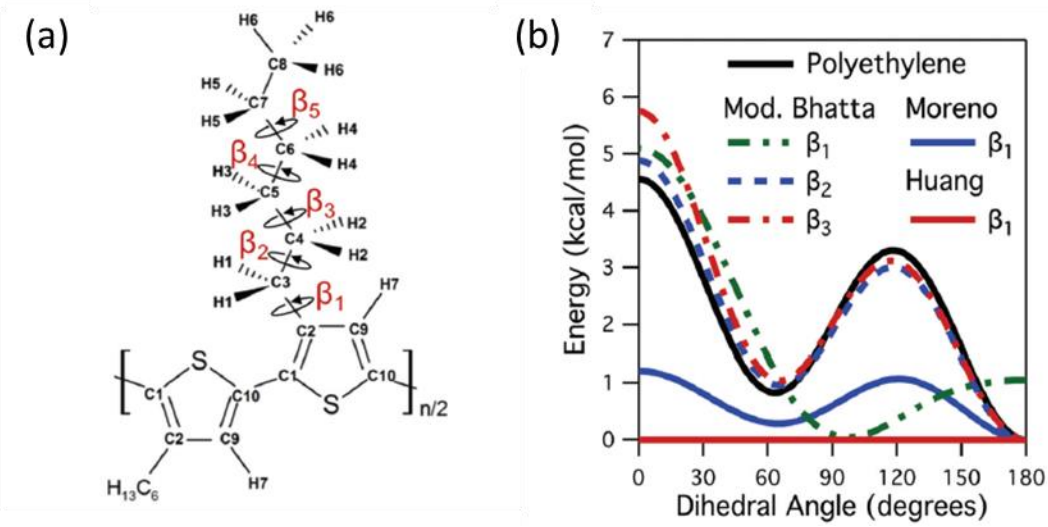

Figure 16: (a) Illustration of the β dihedral angle locations within the molecular structure and (b) torsion potential for side chain dihedral angles determined from different models. Reproduced with permission from the Royal Society of Chemistry.[61]

Another component evaluated between the force fields was the torsion potential for the α dihedral angle, which is located between thiophene monomers (**Figure 17a**). The energies of the models provide

contrasting preferences for cis or trans conformations of the thiophenes at 0° or 180° dihedral angles, respectively (Figure 17b). The modified Bhatta and Moreno models have the lowest energy at 180°, showing preference for the trans conformation, while the Huang has its lowest energy at 0°, preferring cis conformation. Previous experimental studies point to a trans arrangement in P3HT monomers.[64,65] This conformational disagreement further indicates the need for updated force fields for P3HT models to align with experimental data.

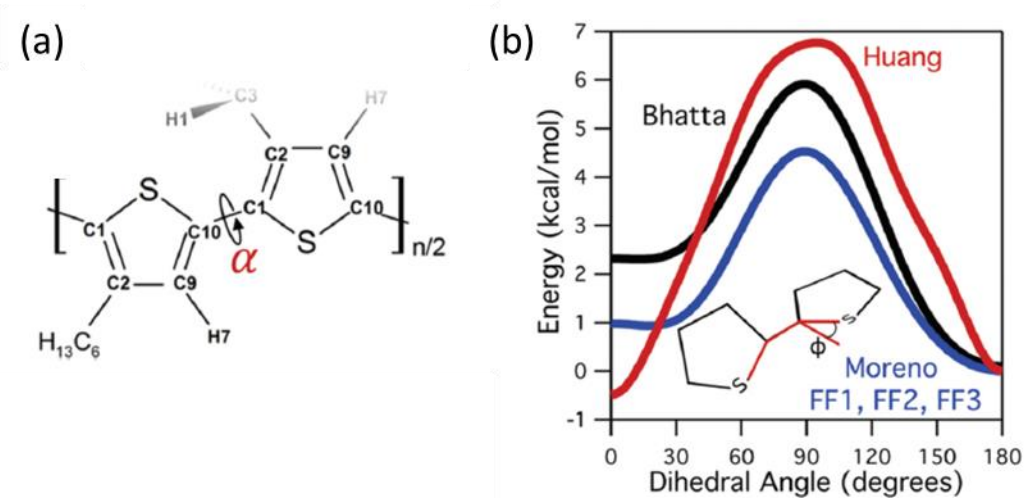

Figure 17: (a) Illustration of the α dihedral angle location along the molecular structure and (b) torsion potential for the dihedral angle from different models. Reproduced with permission from the Royal Society of Chemistry.[61]

In addition to the torsion potentials, the torsion populations, or the distribution of monomers at a given α dihedral angle, were extracted from models. The modified Bhatta, Huang and Moreno 1 force field identified the majority of the population in the trans conformation, while Moreno 2 and 3 show higher population at the cis conformation. Except for the Huang force field, it is also noted that the parameters of the models shift the cis and trans angles to 30° and 150°, instead of 0° and 180° which is attributed to differences in the assigned partial charges on the atoms. The Moreno model which differs only by partial charges in each of its three force fields gives dissimilar torsion populations, highlighting how influential the choice of partial charge is to the polymer's preferred conformation.

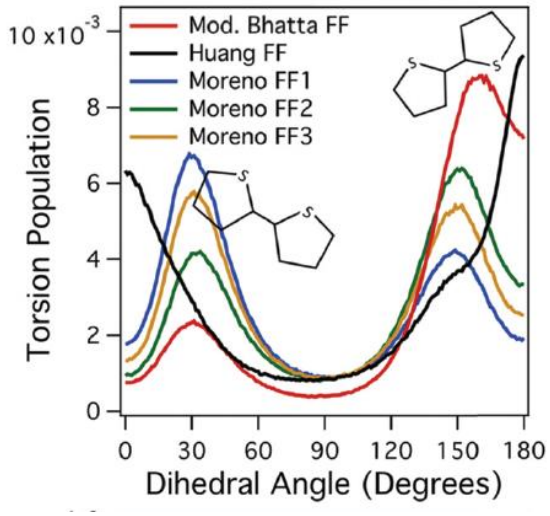

Figure 18: Torsion populations of thiophene rings about the α dihedral angle plotted for the modified Bhatta, Huang and Moreno force fields. Reproduced with permission from the Royal Society of Chemistry.[61]

One major inconsistency in the force fields is the assigned partial charges on P3HT, particularly on the thiophene ring. Not only is there disagreement in the magnitude of the charge on carbon and sulfur atoms, but most carbons in each thiophene monomer are also in disagreement on the sign of the charge, a fundamental parameter (Table 3). It has already been demonstrated by the torsion populations in the Moreno model that variable charges are problematic because they directly affect the structural modeling of P3HT and would lead to inaccurate calculation of its charge transport. An updated model of P3HT is necessary to reflect its properties accurately, especially in the backbone.

Table 3: Partial charges of atoms used for each discussed force field. Italicized rows indicate disagreement of sign. Labeled atoms correspond to the numbering system in figure 2b. Reproduced with permission from the Royal Society of Chemistry.[61]

Atom classes	Bhatta	Huang	Moreno FF1	Moreno FF2	Moreno FF3
S1	*−0.2171*	*−0.1496*	*0.0180*	*−0.1200*	*−0.0510*
C1	*−0.0441*	*0.0748*	*−0.0090*	*0.0000*	*−0.0045*
C2	*0.0318*	*−0.1817*	*0.0000*	*−0.0300*	*−0.0150*
C3	*0.1278*	*0.0617*	*−0.1200*	*0.0300*	*−0.0450*
C4	−0.0926	−0.1200	−0.1200	−0.1200	−0.1200
C5	*0.0189*	*−0.1200*	*−0.1200*	*−0.1200*	*−0.1200*
C6	*0.0289*	*−0.1200*	*−0.1200*	*−0.1200*	*−0.1200*
C7	−0.1396	−0.1200	−0.1200	−0.1200	−0.1200
C8	−0.0670	−0.1800	−0.1800	−0.1800	−0.1800
C9	−0.3128	−0.1817	−0.1150	−0.1800	−0.1475
C10	*0.1762*	*0.0748*	*−0.0090*	*0. 0000*	*−0.0045*
H1	0.0039	0.0600	0.0600	0.0600	0.0600
H2	0.0290	0.0600	0.0600	0.0600	0.0600
H3	0.0036	0.0600	0.0600	0.0600	0.0600
H4	0.0069	0.0600	0.0600	0.0600	0.0600
H5	0.0536	0.0600	0.0600	0.0600	0.0600
H6	0.0200	0.0600	0.0600	0.0600	0.0600
H7	0.2356	0.1817	0.1150	0.1800	0.1475

Differences in the models were also compared by a few other analyses. The radial distribution function was calculated for each force field, which determines the probable distance between two monomers – effectively the intermolecular π-π stacking distance. The modified Bhatta, Huang and Moreno models gave very similar results with the likeliest distance of 6 Å or higher, and a slightly higher probability at 6 Å for the Moreno 1 force field. However, it should be noted that previous discussion has underlined that these models do not simulate representative interactions of P3HT and its π-conjugation. The models also disagree on mass densities, appearing lower than the experimental results. The discrepancy between the Bhatta, Huang and Moreno models ultimately relate to the charge transfer integral, which would lead to inaccurate calculations of interchain and intrachain charge hopping. Our evaluation of current P3HT computational models elucidates their mismatch to each other and to experimental data and highlights the need for a model that can accurately simulate the behavior of a real sample.

3.3 Conclusion

We can conclude from this work that computational models of P3HT reasonably fit to experimental WAXS and QENS data for fully hydrogenated samples but fail to replicate the activity of the conjugated thiophene backbone. The thiophene backbone is of utmost importance to simulate by molecular dynamics due to its charge transport properties which differ from classical structures like the alkyl side chain. This work is the first example to compare multiple conjugate polymer force fields and validate by experimental data. Differing torsion potentials, partial charges, and intermolecular spacing between force fields were identified and bring to light the need for updated parameters in the P3HT model that accurately simulate its molecular properties.

4: Improved Strain Resistance of Elastomer/π-Conjugated Polymer Blends Through Side Chain Functionalization

4.1 Stretchable Electronics Overview

The field of stretchable electronics[66] has gained interest in recent years with exciting findings reported for solar cells,[67] batteries,[68] light-emitting diodes (LEDs),[69] and sensors,[70] as well as wearable electronics[70,71] such as implants[72] and electronic skin.[73] While great strides have been made to improve the electrical performance of organic electronics,[74–77] the mechanical stability of π-conjugated polymers has not received as much attention and must be considered for them to become feasible materials for stretchable devices.[78–80]

One approach to produce stretchable conductive materials is by taking advantage of the inherent properties of π-conjugated polymers and elastomers though polymer blending.[81–94] Insulating elastomers can tolerate and recover from high, repeated strain. On the other hand, π-conjugated polymers are brittle due to the rigid, planar backbones and π-π interactions that generate charge transport.[95] Comparison of both electrical and mechanical performance in these elastomer/π-conjugated polymer blends indicates a competition between the elastic and conductive behavior. Thus, it is key to develop techniques where mechanical durability in such composites is enhanced without compromising electrical performance.

Some studies suggest that greater miscibility can reduce the mechanical/electrical property tradeoff,[88–90] yet elastomer/π-conjugated polymer blends are typically phase segregated.[90–93] Enhanced compatibility for traditional insulating polymers can be achieved by improving interfacial adhesion by several techniques.[96–98] One method is to modify the chemical structure to promote better intermolecular interactions, such as hydrogen bonding, between the two polymer types. Another approach is to reactively bond across domains and form covalent bonds, which strengthens the interfaces and the overall composite. The third technique uses compatibilizing agents, which are tailored chemical additives, often block

copolymers, that are miscible in both polymers that reduce phase segregation. The first two approaches are applied in this research for elastomer/π-conjugated polymer blends. Reactive bonding has been explored for π-conjugated polymers with alkyl side chains functionalized by bromide, oxetane, azide, and other groups.[99–101] Devices with crosslinked polymers demonstrated enhanced thermal stability, resistance to solvent, and overall lifetime improvement.[102–110] While crosslinking has been studied with insulators and π-conjugated polymers individually, reactive compatibilization in elastomer/π-conjugated polymer composites has yet to be reported. In the following studies, we demonstrate improved compatibility in these blends through side chain functionalization of the π-conjugated polymer to regulate morphology and improve mechanical performance.

The approach of π-conjugated polymer functionalization in this work promotes compatibility by introducing backbone disorder to weaken π-π interactions, leading to reduced domain sizes and interfacial tension. Functionalization is further utilized as a reactive compatibilizer to strengthen interfaces between segregated polymer. Unsaturated elastomers containing butadiene monomers were chosen as the elastomer due to the ability of this alkene group to undergo crosslinking.[111–113] The π-conjugated polymer utilized was poly(3-hexylthiophene) functionalized by thiol or bromide groups. The added functional groups act to modify polymer packing and double as a photoreactive bonding site. With the presence of a radical initiator, thiols are able to bond with alkenes via an addition reaction.[114–117] The bromide group is thought to undergo homolytic cleavage at the C-Br bond under UV light activation, initiating radical-mediated crosslinking.[106,118–120] Bromide side chains in several π-conjugated polymers, including P3Br$_{0.1}$HT, have shown negligible effects on the packing order of conjugated backbones before and after crosslinking, as determined by UV-vis and X-ray diffraction, but this is the first example to study P3Br$_x$HT with a broad range and high concentration of functionalization in both neat and elastomer-blended films.[105–110] The solution processability of the elastomer and π-conjugated polymer, as well as light-activated crosslinking of films,

presents a simple and scalable system to enhance mechanical properties for more robust stretchable electronic materials.

4.2 Experimental Procedures

4.2.1 Materials

The following chemicals were purchased from Sigma-Aldrich: sodium methoxide, 1,6-dibromohexane, magnesium, iodine, [1,3-bis(diphenylphosphino)propane]nickel(II) chloride, anhydrous diethyl ether, 3-bromothiophene, aqueous hydrobromic acid (48%), iodobenzenediacetate, nickel(II) bromide, triphenylphosphine, 2-bromotoluene, potassium thioacetate, 2.0 M dimethylamine in THF, anhydrous methanol, 60% sodium hydride in oil, 2,2':5',2"-terthiophene, phenylbis(2,4,6-trimethylbenzoyl)phosphine oxide, commercially known as Irgacure 819 (I819), 3,5-di-*tert*-butyl-4-hydroxytoluene (BHT), hexamethyldisilazane (HMDS), and isopropyl magnesium chloride solution in THF which was titrated prior to use according to literature procedure.[121] The following polymers were purchased from Sigma-Aldrich: 100 kg/mol poly(styrene-*co*-butadiene) 45% (w/w) styrene with 20% *cis*, 60% *trans*, 20% *vinyl* butadiene isomers (SBco), and 200-300 kg/mol *cis*-polybutadiene rubber (PB).

The following chemicals were purchased from TCI chemicals: 4-methoxyphenol, 2-bromo-3-hexyl-5-iodothiophene, 1,3-bis(diphenylphosphino)propane, anhydrous dichloromethane, dithiothreitol, and 1,4-butanediol bis(thioglycolate) (BIS). *N*-bromosuccinimide was purchased from Oakwood Chemical and recrystallized in water (10 g/100 mL) prior to use. Anhydrous tetrahydrofuran (THF) was dried in a DriSolv solvent dispensing system. 200 proof ethanol was purchased from Decon labs and dried under activated Fisher brand 3Å molecular sieves. All other materials were used without further purification. Heavily boron doped silicon wafers with a 300 ± 5 nm thermal oxide layer were purchased from WRS Materials. The detergent used for cleaning substrates was Meri-Suds dishwashing liquid from CH2O. CLEVIOS P VP AI 4083

aqueous dispersion of poly(3,4-ethylenedioxythiophene) polystyrene sulfonate (PEDOT/PSS) was purchased from Heraeus. The Dow Corning Sylgard 184 kit was used to cure polydimethylsiloxane (PDMS).

4.2.2 NMR

Synthesized products were characterized by ^{1}H NMR on Bruker 300 MHz AVance series instrument and by ^{13}C NMR on 500 MHz Bruker AV series instrument in deuterated chloroform and referenced to the residual chloroform peak (Figure 19 - Figure 39).

4.2.3 SEC

Size exclusion chromatography (SEC) for polymers was performed in tetrahydrofuran on a Shimadzu Prominence HPLC referenced to polystyrene standards for high molecular weight polymers (~20 kg/mol). The Malvern Viscotek TDA 305 gel permeation chromatography (GPC) was coupled to a UV and refractive index detector for low molecular weight polymers (<10 kg/mol) at room temperature and for commercial poly(styrene-*co*-butadiene) at 50° C in tetrahydrofuran referenced to polystyrene standards.

4.2.4 MALDI-TOF

MALDI-TOF was performed on the Bruker Autoflex II using 2,2′:5′,2′′-terthiophene matrix casted from chloroform solution.

4.2.5 Monomer synthesis

6-(4-methoxyphenoxy)hexyl bromide (1): Anhydrous ethanol (460 mL) was added to a dry flask containing sodium methoxide (21.64 g, 0.40 mol), followed by the addition of 4-methoxyphenol (40.99 g, 0.33 mol) and 1,6-dibromohexane (200 mL, 1.30 mol). The reaction was refluxed for 2 hr with monitoring by TLC and cooled to room temperature. The product was extracted with diethyl ether and washed with DI water. The aqueous layer was extracted with diethyl ether 3x and the collected organic phase was dried with $MgSO_4$ and rotary evaporation. Excess 1,6-dibromohexane was removed by heated vacuum distillation, and the product was purified by recrystallization in hexane (10 g/100 mL) to yield a white solid in 26% yield. **^{1}H NMR** (300 MHz, $CDCl_3$), δ (ppm): 6.82 (s, 4H), 3.91 (t, 2H), 3.76 (s, 3H), 3.41 (t, 2H), 1.89 (m, 2H), 1.77 (m, 2H), 1.50 (m, 4H). **^{13}C NMR** (500 MHz, $CDCl_3$), δ (ppm): 154.1, 153.4, 115.7, 114.9, 68.6, 55.9, 33.8, 32.9, 29.4, 28.1, 25.5.

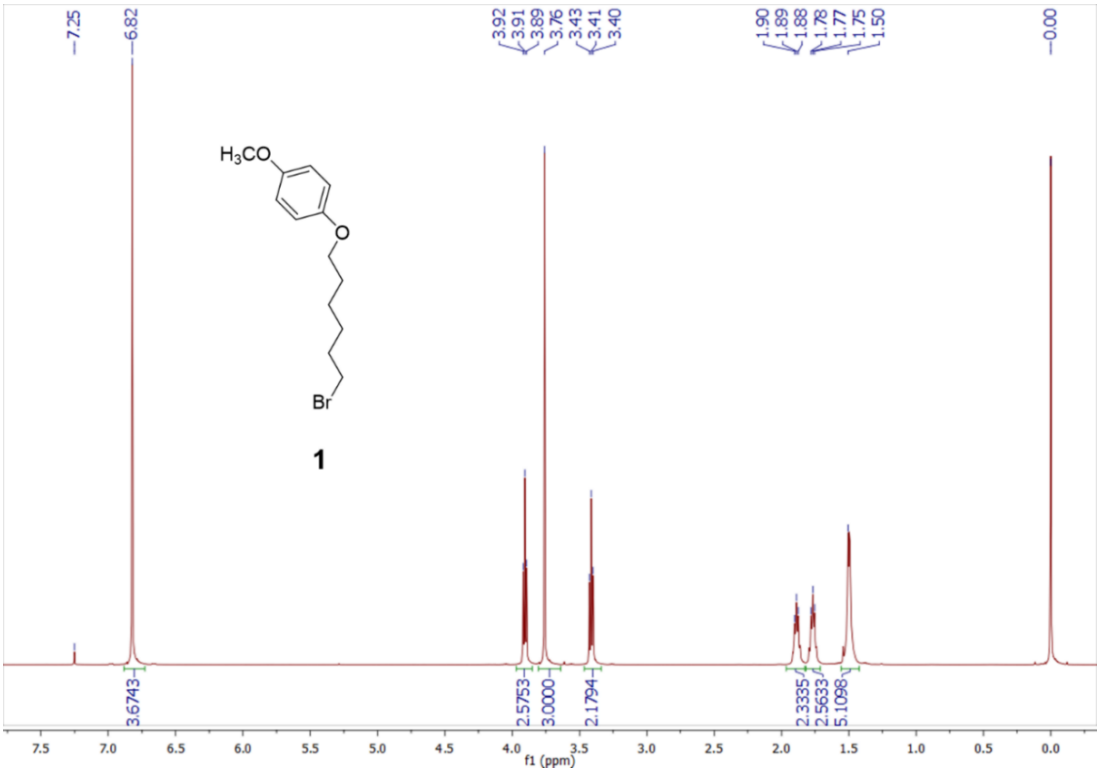

Figure 19: *[1]H NMR of **1**, 6-(4-methoxyphenoxy)hexyl bromide*

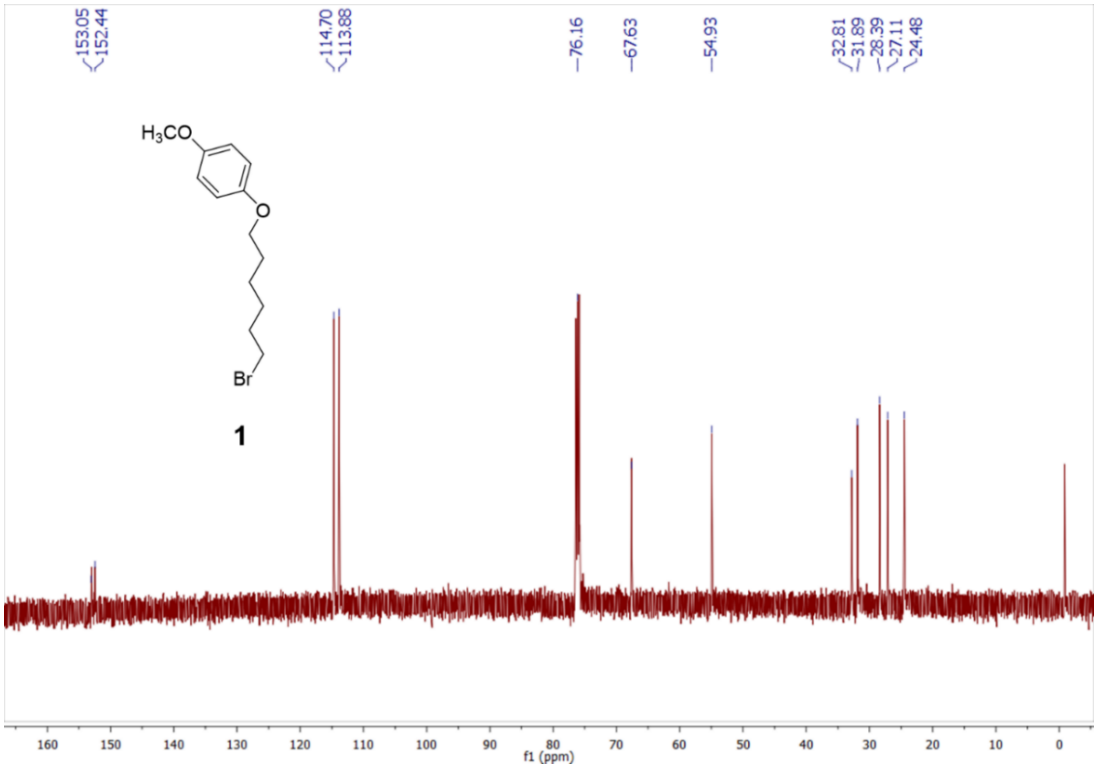

Figure 20: *[13]C NMR of **1**, 6-(4-methoxyphenoxy)hexyl bromide*

3-(6-(4-methoxyphenoxy)hexyl)thiophene (2): *All steps of the reaction were performed under nitrogen.* Magnesium (2.41 g, 99 mmol) was flame dried in a flask under vacuum and a pinch of iodine was added once cooled. An addition funnel was attached to the flask and filled with anhydrous diethyl ether (150 mL). A second addition funnel containing solid **(1)** (25.20 g, 88 mmol) was stacked on the first addition funnel and melted into the bottom funnel. A portion of the **(1)**/ether mixture was dripped into the magnesium turnings and the reaction was initiated with gentle heating and crushing of magnesium. The remaining mixture was then added dropwise and stirred overnight, followed by 3 hr at reflux with TLC monitoring. A separate flask was prepared with [1,3-bis(diphenylphosphino)propane]nickel(II) chloride (0.0888 g, 0.154 mmol) and 3-bromothiophene (7.48 mL, 80. mmol). To this flask, Grignard reagent **(1)** was slowly added in an ice bath shielded from light, refluxed overnight and monitored by TLC. The reaction was quenched by cooling the flask to 0° C and slowly adding 1 M HCl (20 mL). The product was extracted by dichloromethane and washed with water followed by drying of the organic layer with $MgSO_4$ and rotary evaporation. Brown solid impurities were removed by filtration in hot hexane, and the remaining product was purified by silica gel column chromatography in 1:1 hexane:dichloromethane (v/v). A white crystal solid was collected in 26% yield. **^{1}H NMR** (300 MHz, $CDCl_3$), δ (ppm): 7.28 (m, 1H), 6.97 (m, 2H), 6.87 (s, 4H), 3.95 (t, 2H), 3.81 (s, 3H), 2.69 (t, 2H), 1.81 (m, 2H), 1.71 (m, 2H), 1.54 (m, 2H), 1.45 (m, 2H). **^{13}C NMR** (500 MHz, $CDCl_3$), δ (ppm): 153.9, 153.5, 143.2, 128.4, 125.2, 120.0, 115.7, 114.8, 68.8, 55.9, 30.6, 30.3, 29.5, 29.2, 26.0.

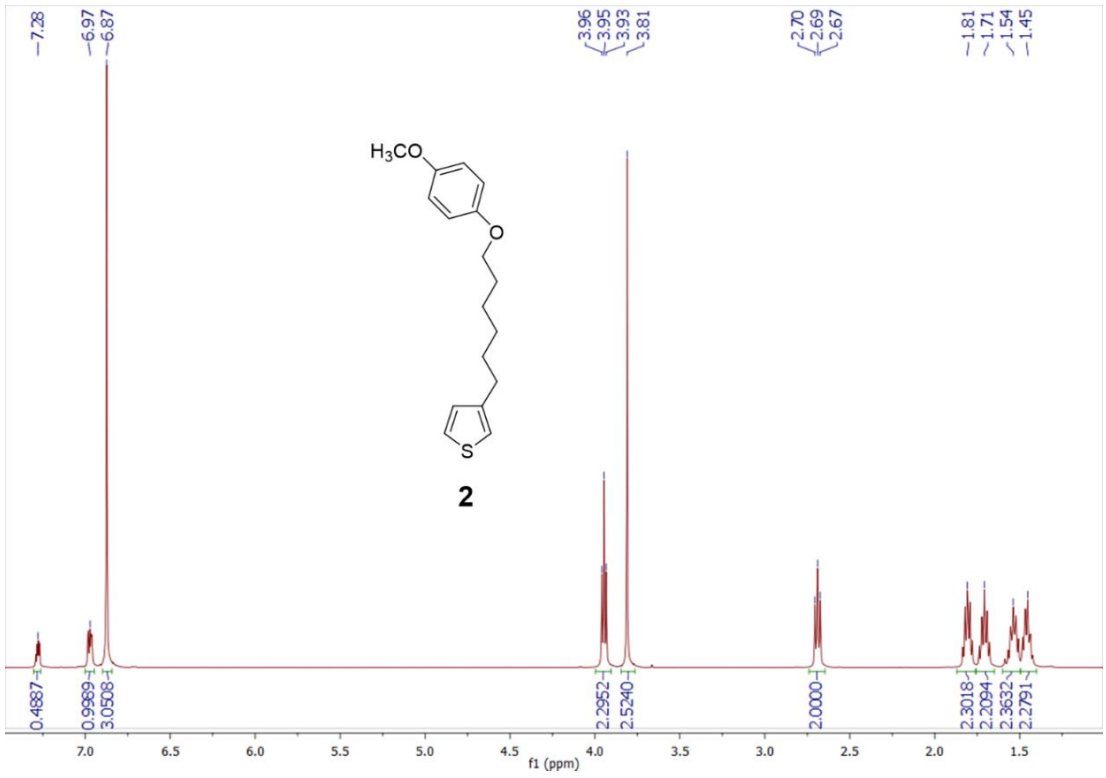

*Figure 21: ^{1}H NMR of **2**, 3-(6-(4-methoxyphenoxy)hexyl)thiophene*

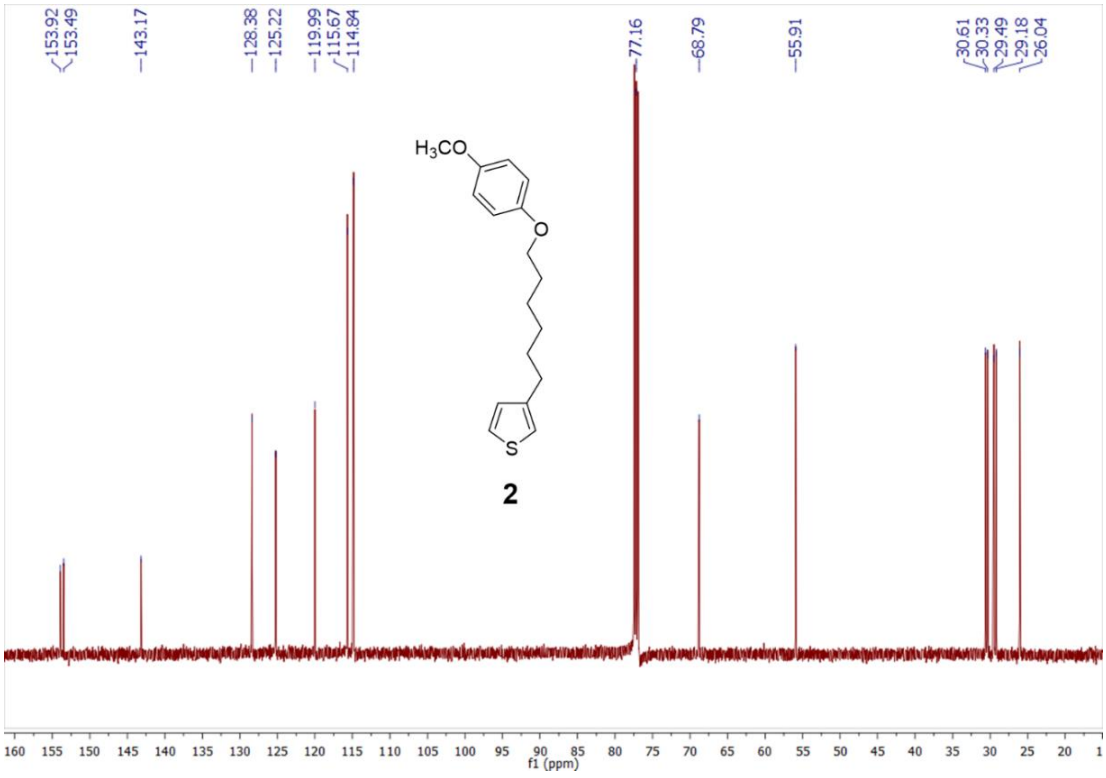

*Figure 22: ^{13}C NMR of **2**, 3-(6-(4-methoxyphenoxy)hexyl)thiophene*

3-(6-bromohexyl)thiophene (3): In air, **(2)** (8.22 g, 29 mmol) was dissolved in acetic anhydride (26.8 mL) with gentle heating. Aqueous HBr (48%, 19.4 mL, 171 mmol) was added dropwise in an ice bath, then refluxed for 24 hr at 100° C. The mixture was diluted with DI water, then extracted with diethyl ether and washed with saturated $NaHCO_3$. The organic layer was dried with $NaSO_4$ and concentrated *in vacuo*. Brown by-products were removed by precipitating in hexane and filtering. The filtrate was further purified through a silica gel column in hexane to collect a clear, colorless oil in 77% yield. **^{1}H NMR** (300 MHz, $CDCl_3$), δ (ppm): 7.23 (m, 1H), 6.93 (m, 2H), 3.40 (t, 2H), 2.64 (t, 2H), 1.86 (m, 2H), 1.64 (m, 2H), 1.34-1.51 (m, 4H). **^{13}C NMR** (500 MHz, $CDCl_3$), δ (ppm): 142.8, 128.2, 125.2, 119.9, 33.9, 32.8, 30.4, 30.2, 28.4, 28.0.

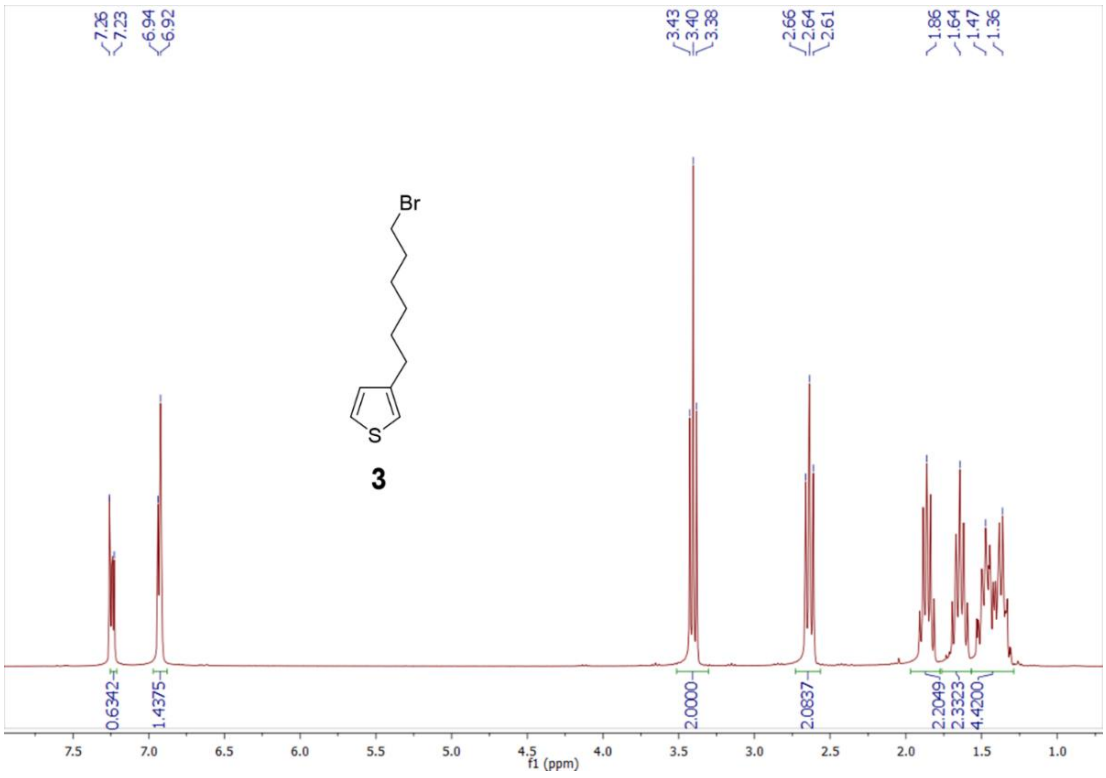

*Figure 23: [1]H NMR of **3**, 3-(6-bromohexyl)thiophene*

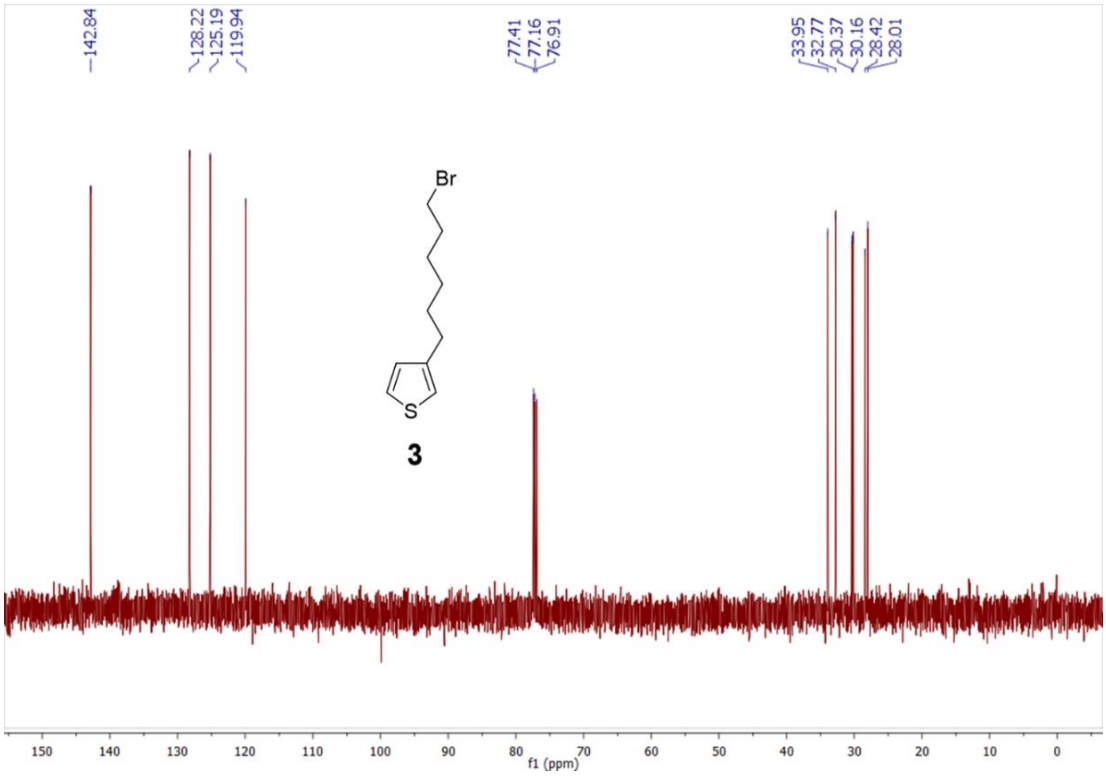

*Figure 24: [13]C NMR of **3**, 3-(6-bromohexyl)thiophene*

2-bromo-3-(6-bromohexyl)thiophene (4): First, **(3)** (3.24 g, 17.8 mmol) was dissolved in anhydrous THF (90 mL) and cooled in an ice bath. Slowly, *N*-bromosuccinimide (3.18 g, 17.5 mmol) was added and stirred for 1 hr under nitrogen at 0° C. The contents were washed with DI water, and extracted with diethyl ether. The organic layer was washed sequentially with 10% (m/v) $Na_2S_2O_3$, 10% (m/v) NaOH, and saturated NaCl, then dried with Na_2SO_4. Solvent removal was completed *in vacuo* to yield a yellow oil in 92% yield. **^{1}H NMR** (300 MHz, $CDCl_3$), δ (ppm): 7.20 (d, 1H), 6.81 (d, 2H), 3.41 (t, 2H), 2.59 (t, 2H), 1.87 (m, 2H), 1.62 (m, 2H), 1.49 (m, 2H), 1.38 (m, 2H). **^{13}C NMR** (500 MHz, $CDCl_3$), δ (ppm): 141.6, 128.2, 125.3, 108.9, 33.9, 32.7, 29.5, 29.2, 28.3, 28.0.

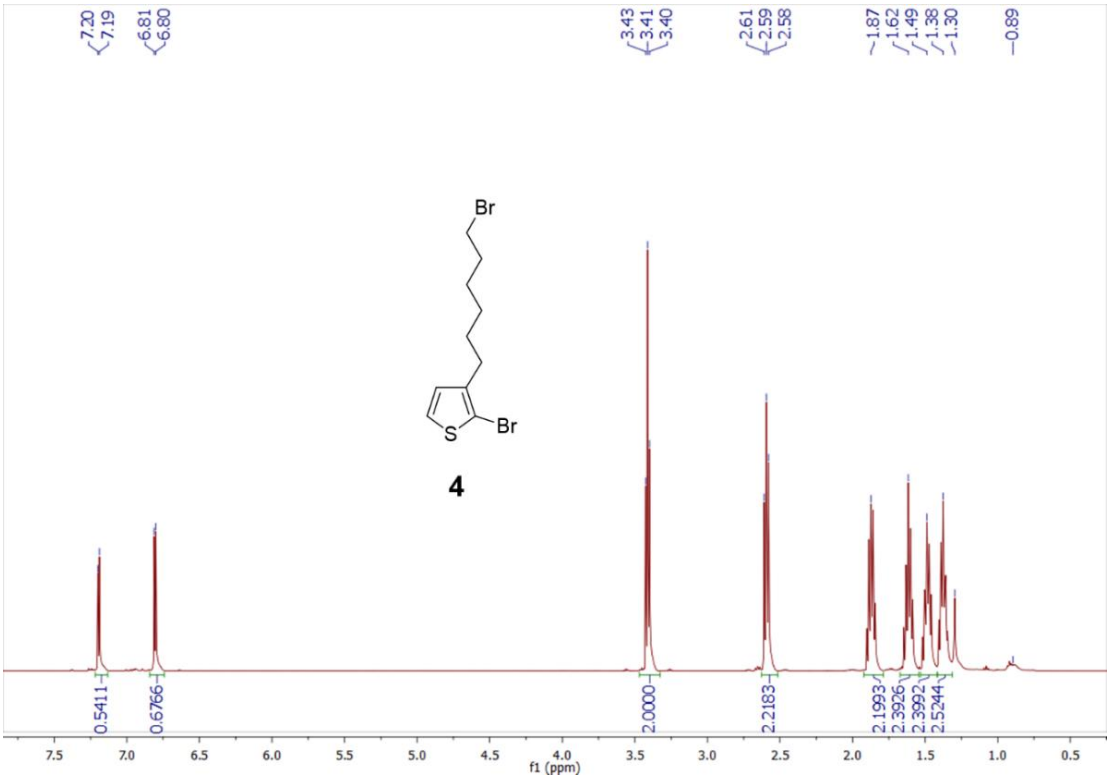

*Figure 25: ^{1}H NMR of **4**, 2-bromo-3-(6-bromohexyl)thiophene*

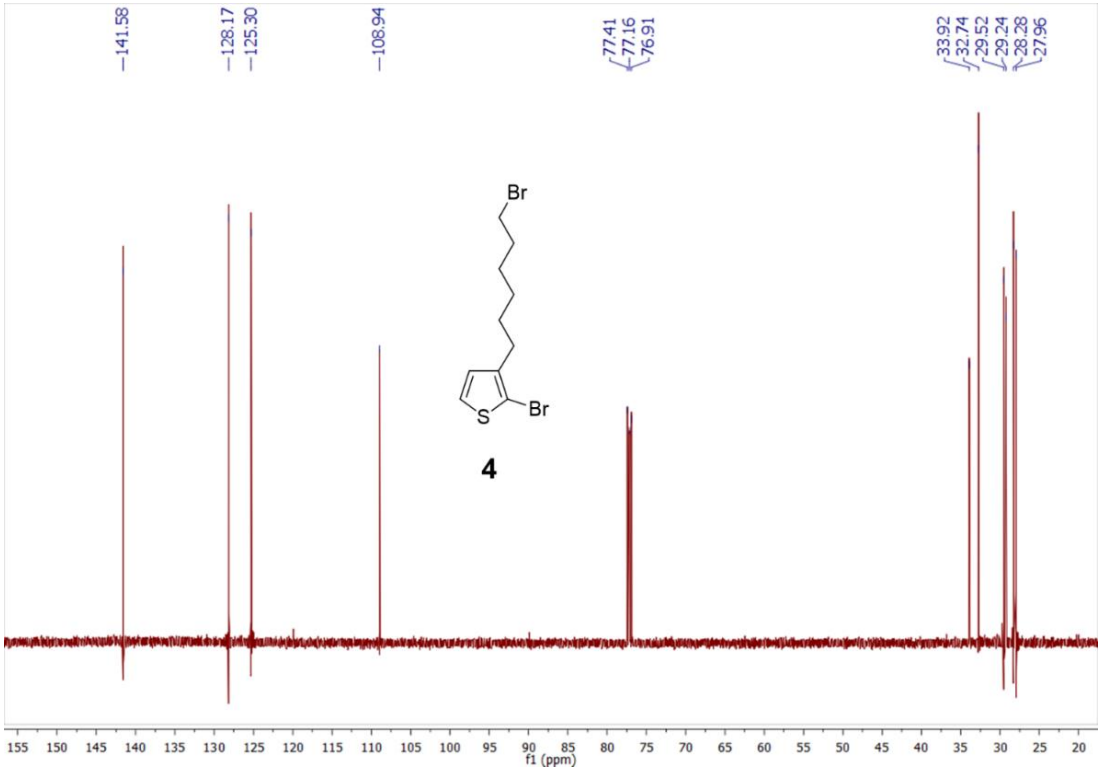

*Figure 26: ^{13}C NMR of **4**, 2-bromo-3-(6-bromohexyl)thiophene*

2-bromo-5-iodo-3-(6-bromohexyl)thiophene (5): In anhydrous dichloromethane (200 mL), **(4)** (7.80 g, 30 mmol) was dissolved, shielded from light, and cooled in an ice bath under nitrogen. Iodine (4.18 g, 16.5 mmol) and iodobenzenediacetate (5.80 g, 18 mmol) were added to the solution. After stirring for 1 hr under nitrogen, the ice bath was removed and stirring continued overnight. The crude product was collected by washing sequentially with 10% (m/v) $Na_2S_2O_3$, saturated $NaHCO_3$, and saturated NaCl. The organic layer was dried with Na_2SO_4 and removed *in vacuo.* The product was further purified by running through a silica gel plug in hexane. Following *in vacuo* solvent removal, the remaining by-product was removed under reduced pressure with gentle heating (40-50° C) to collect a faint yellow oil in 94% yield. **^{1}H NMR** (300 MHz, $CDCl_3$), δ (ppm): 6.96 (s, 1H), 3.40 (t, 2H), 2.53 (t, 2H), 1.86 (m, 2H), 1.56 (m, 2H), 1.46 (m, 2H), 1.34 (m, 2H). **^{13}C NMR** (500 MHz, $CDCl_3$), δ (ppm): 144.0, 137.0, 111.9, 71.4, 34.0, 32.7, 29.5, 29.1, 28.3, 28.0.

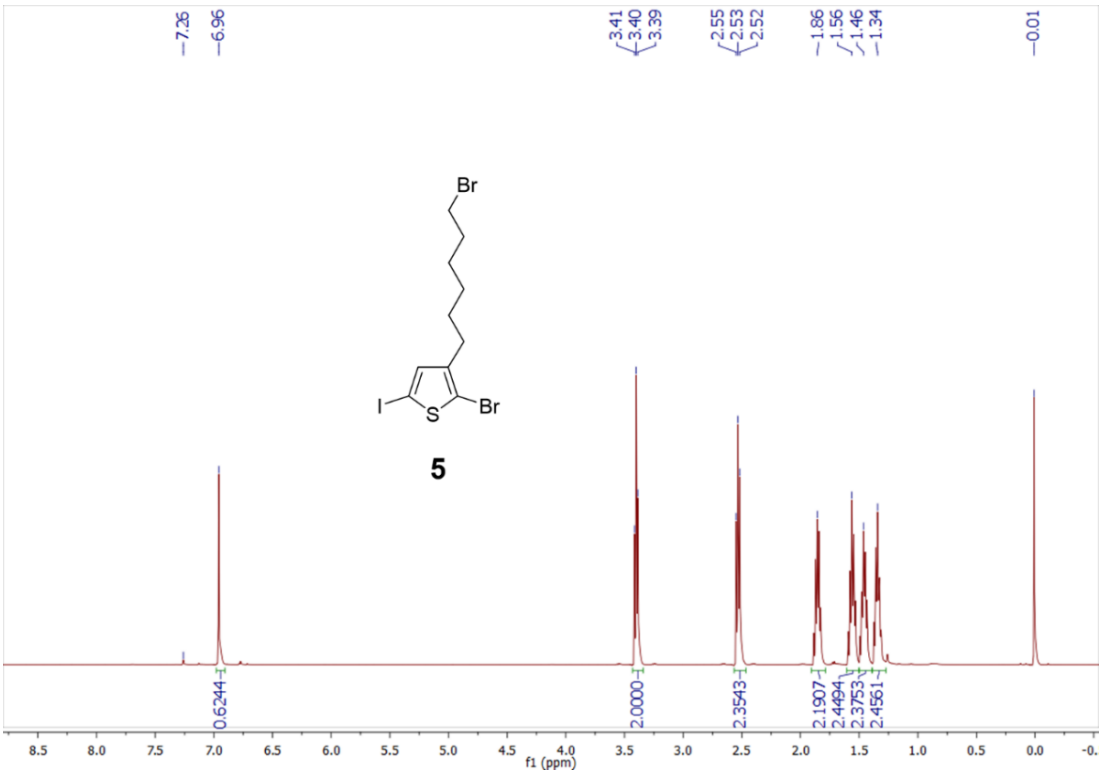

*Figure 27: [1]H NMR of **5**, 2-bromo-5-iodo-3-(6-bromohexyl)thiophene*

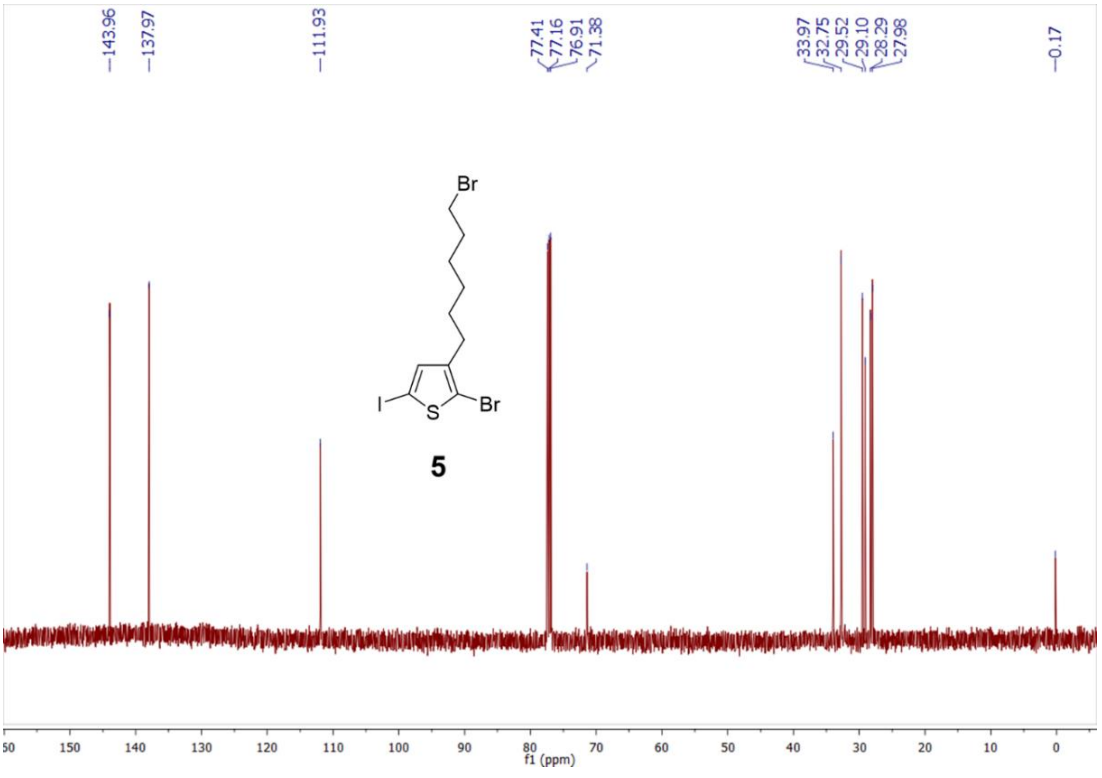

*Figure 28: [13]C NMR of **5**, 2-bromo-5-iodo-3-(6-bromohexyl)thiophene*

2-bromo-5-iodo-3-(6-hexylthioacetate)thiophene (6): Under nitrogen, **(5)** was dissolved (195 mg) in anhydrous THF (80 mL) and potassium thioacetate (480 mg) was added. The mixture was shielded from light and refluxed for 24 hr at 70° C. The mixture was purified by flash column chromatography in hexane and dried *in vacuo* to collect yellow-orange crystals in 91% yield. **^{1}H NMR** (300 MHz, $CDCl_3$), δ (ppm): 6.95 (s, 1H), 2.86 (t, 2H), 2.52 (t, 2H), 2.32 (s, 3H), 1.55 (m, 4H), 1.35 (m, 4H).

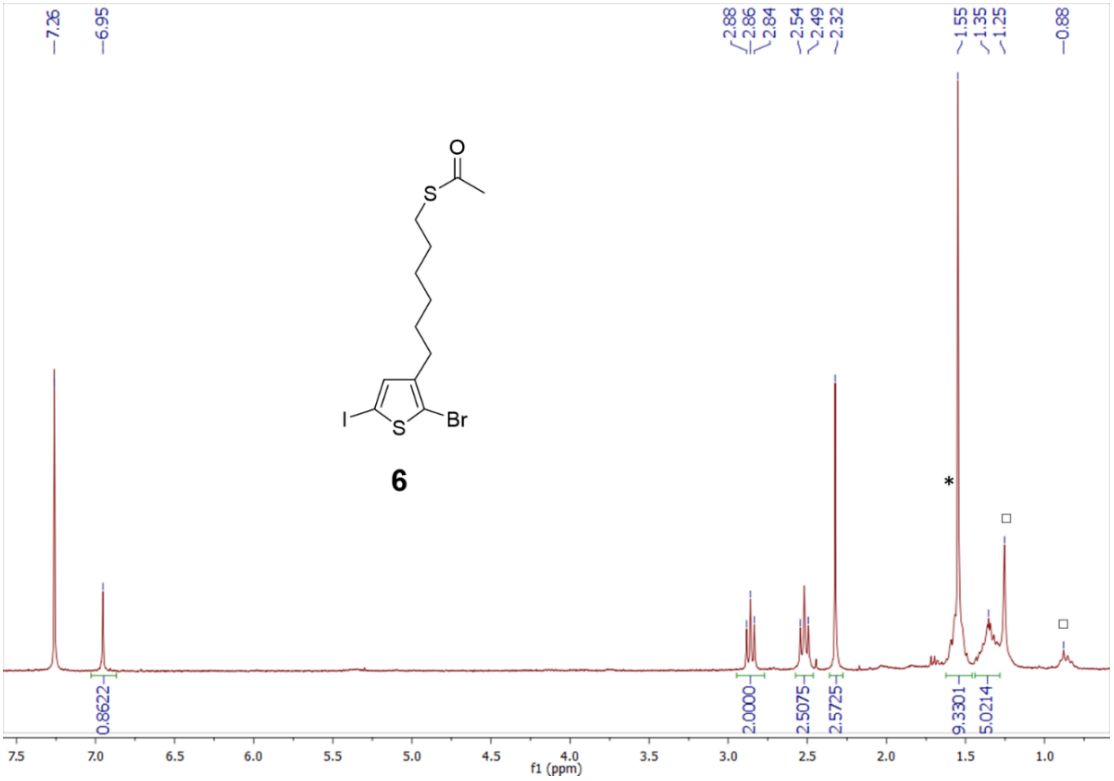

*Figure 29: ^{1}H NMR of **6**, 2-bromo-5-iodo-3-(6-hexylthioacetate)thiophene *water □grease*

2-bromo-5-iodo-3-(6-mercaptohexyl)thiophene (7): In nitrogen atmosphere, **(6)** (34 mg) was dissolved in THF (10 mL) degassed by freeze-pump-thaw cycles and 2.0 M dimethylamine in THF was added (3.0 mL). The reaction was stirred at room temperature for 8 hr and monitored by TLC. The crude reaction mixture was dried and purified by column chromatography in hexane. The product was dried *in vacuo* and collected in 12% yield. **^{1}H NMR** (300 MHz, $CDCl_3$), δ (ppm): 6.96 (s, 1H), 2.67 (t, 2H), 2.53 (t, 2H), 1.68 (m, 2H), 1.55 (m, 2H), 1.38 (m, 4H).

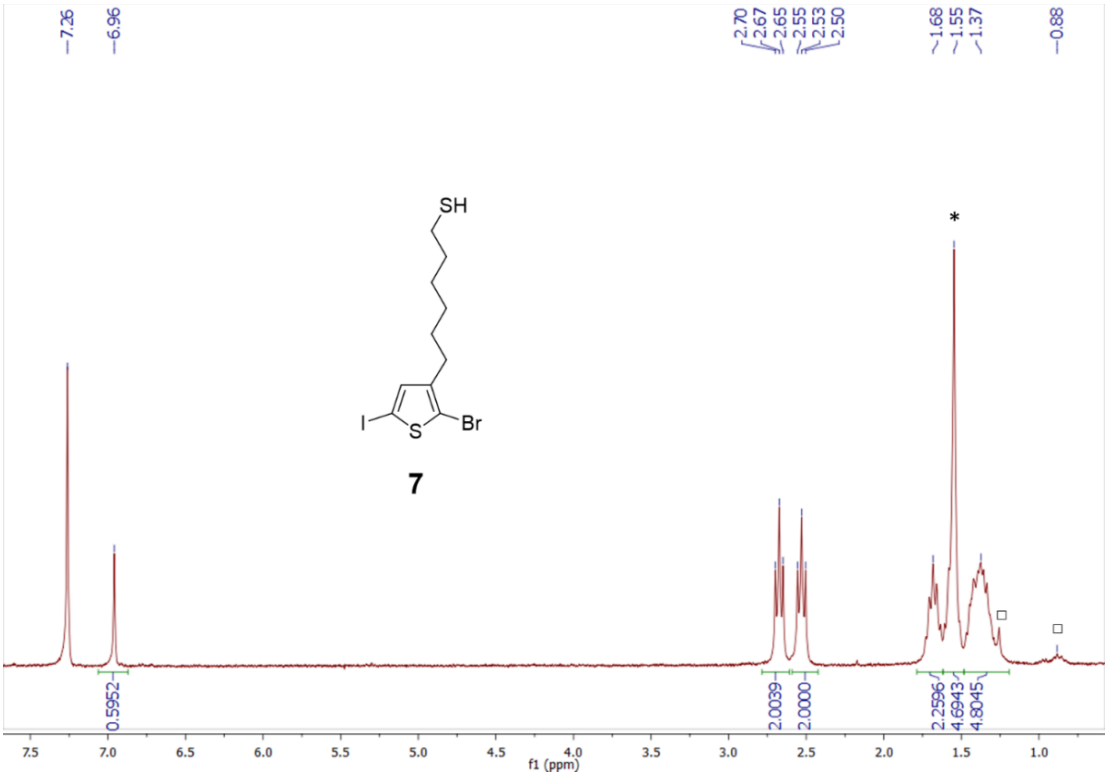

*Figure 30: ^{1}H NMR of 7, 2-bromo-5-iodo-3-(6-mercaptohexyl)thiophene *water □grease*

(o-tolyl)bis-(triphenylphosphine)nickel(II) bromide: *All steps of the reaction were performed under nitrogen.* In a dried flask, nickel(II) bromide (2.16 g, 9.9 mmol) and triphenylphosphine (5.20 g, 19.8 mmol) were stirred in anhydrous THF (15 mL) and refluxed for 2 hr at 65° C. A solution of 2-bromotoluene (1.20 mL, 10.0 mmol) in anhydrous THF (10 mL) was transferred to an addition funnel and added dropwise to a flask of dried magnesium turnings (0.29 g, 12.1 mmol), then stirred for 1 hr. The Grignard solution was added to the nickel solution and stirred for 20 min. In air, the product was vacuum filtered and washed with methanol, then dried *in vacuo* to yield a light orange powder. **^{31}P NMR** (300 MHz, $CDCl_3$), δ (ppm): 22.17.

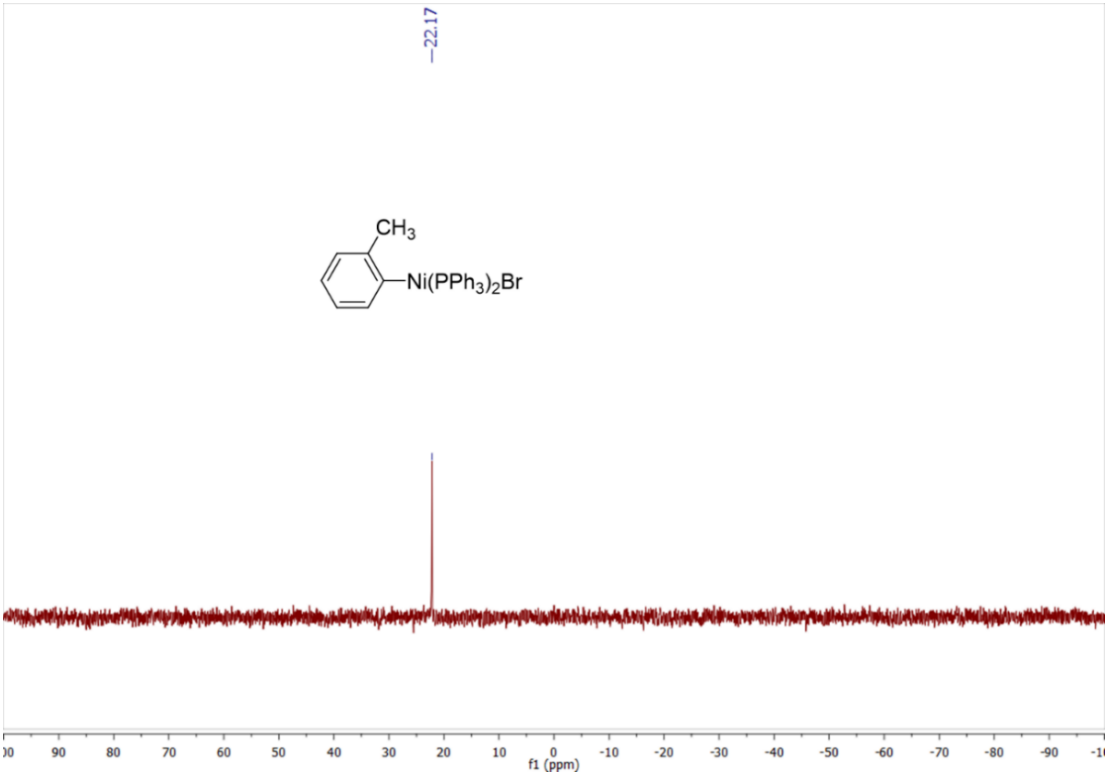

Figure 31: ^{31}P NMR of (o-tolyl)bis-(triphenylphosphine)nickel(II) bromide

4.2.6 Polymerization

α-2-thiol-3-hexylthiophene-5-yl-ω-2-thiol-3-hexylthiophene-5-yl-poly(3-hexylthiophene-2,5-diyl) (SH-P3HT-SH) [122]: Synthesis was synthesized carried out according to literature procedure to collect a dark solid in 15% yield. **^{1}H NMR** (300 MHz, $CDCl_3$), δ (ppm): 6.98 (s, 1H), 2.80 (t, 2H), 1.71 (m, 2H), 1.34-1.46 (m, 6H), 0.91 (t, 3H).

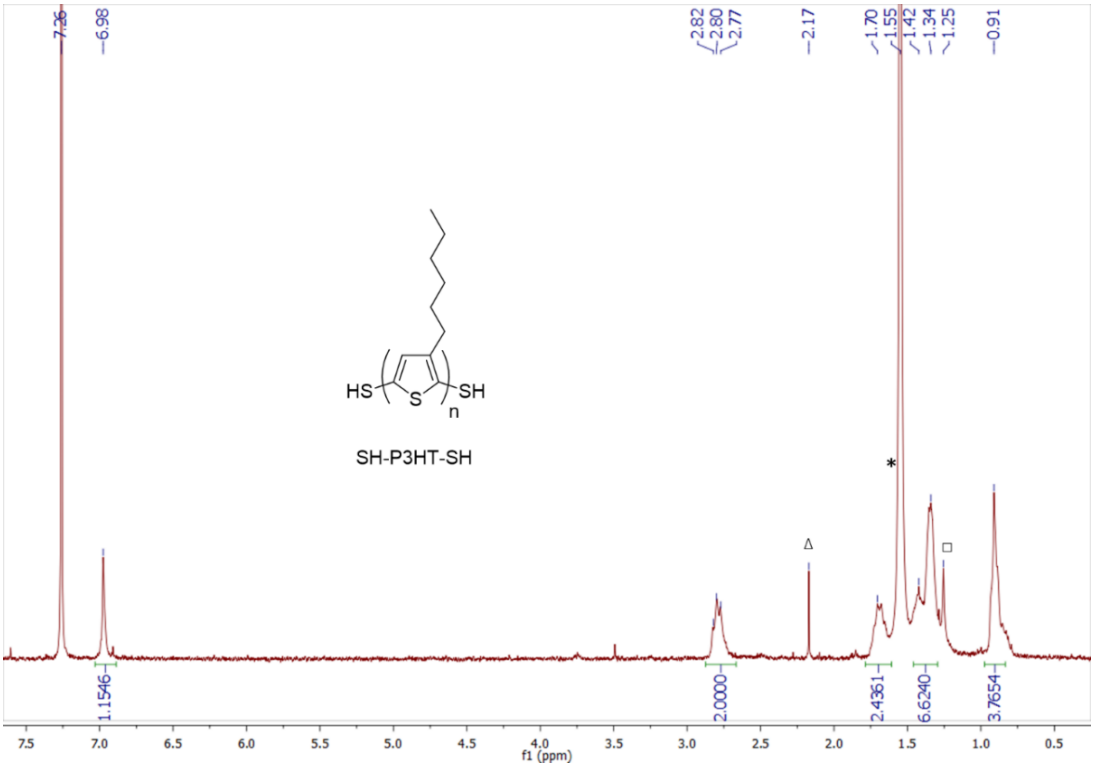

*Figure 32: ^{1}H NMR of SH-P3HT-SH, thiol-capped poly(3-hexylthiophene) Δacetone *water □grease*

Pre-functionalization polymerization (8, 9, 10): In a flask, **(5)**, **(6)**, or **(7)** (0.50 mmol) was placed under vacuum for 20 min and dissolved in anhydrous THF (0.1 M) under nitrogen. Titrated isopropyl magnesium chloride THF solution (0.95 equivalence) was added dropwise over 5-10 min to a light-shielded flask cooled in an ice bath and allowed to stir for 1 hr. Meanwhile, catalyst solution was prepared by ligand exchange in a separate flask by stirring (o-tolyl)bis-(triphenylphosphine)nickel(II) bromide (0.0195 equivalence) and 1,3-bis(diphenylphosphino)propane (0.0389 equivalence) in 1-2 mL of THF at room temperature for 20 min. The catalyst solution was quickly added to the monomer solution at 0° C and stirred at room temperature for 1 hr. The reaction was quenched with 5 M HCl for 5 min and polymer was precipitated in methanol. The product was filtered and rinsed with methanol, then acetone to collect a dark reddish solid of **(8)** only. **(8) ^{1}H NMR** (300 MHz, $CDCl_3$), δ (ppm): 6.98 (s, 1H), 3.43 (t, 2H), 2.82 (t, 2H, *Th-CH_2 head-tail*), 2.63 (t, 2H, *Th-CH_2 head-head*), 2.49 (s, 3H, *α-tol-CH_3*), 1.90 (m, 2H), 1.71(m, 2H), 1.48 (t, 4H).

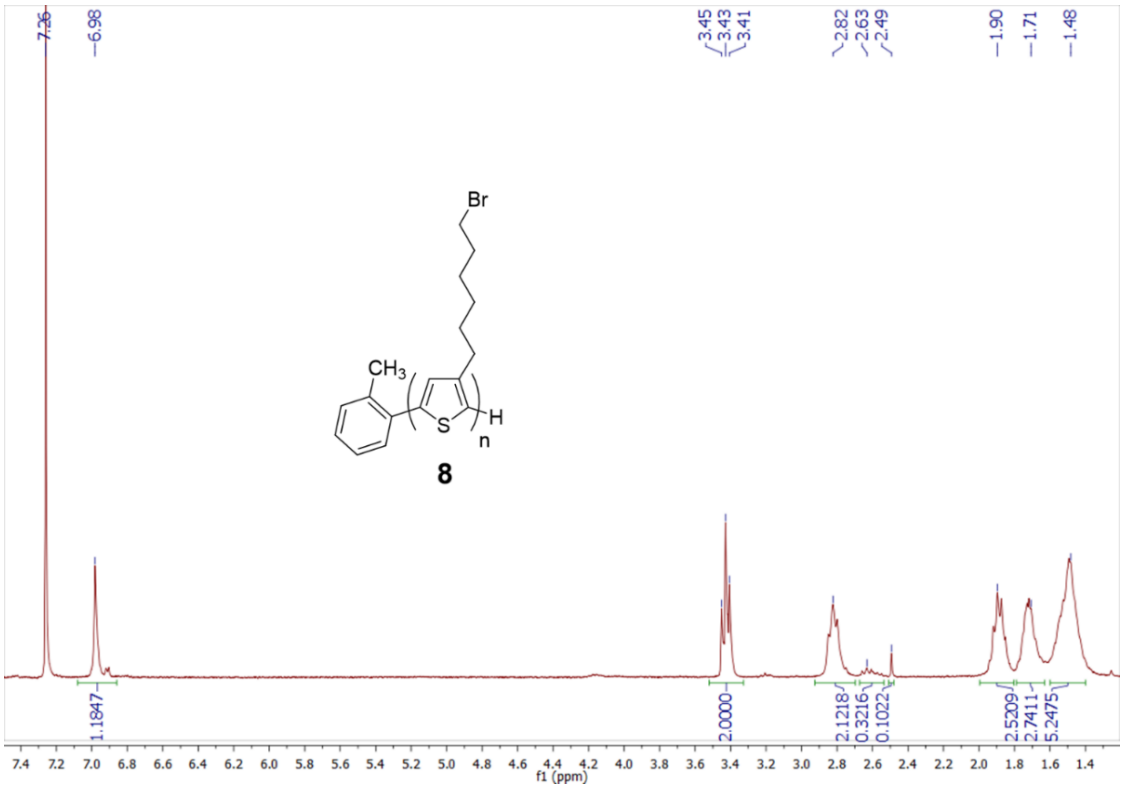

*Figure 33: ^{1}H NMR of **8**, poly(3-(6-bromohexyl)thiophene)), low M.W.*

Poly[(3-(6-bromohexyl)thiophene)-*ran*-(3-hexylthiophene)] (P3Br$_x$HT): In a flask, 0:1, 0.25:0.75, 0.75:0.25, or 1:0 molar ratios of **(5)**: 2-bromo-3-hexyl-5-iodothiophene (0.50 mmol total) were placed under vacuum for at least 30 min. The monomer mixture was dissolved in anhydrous THF (0.1 M) under nitrogen. Titrated isopropyl magnesium chloride THF solution (0.95 equivalence) was added dropwise over 5-10 min to a light-shielded flask cooled in an ice bath and allowed to stir for 1 hr. Meanwhile, catalyst solution was prepared by ligand exchange in a separate flask by stirring (o-tolyl)bis-(triphenylphosphine)nickel(II) bromide (0.0105 equivalence) and 1,3-bis(diphenylphosphino)propane (0.0210 equivalence) in 0.50 mL of THF at room temperature for 1 hr. The catalyst solution was quickly added to the monomer solution at 0° C and the flask was transferred to a pre-heated oil bath at 50° C. As needed, excess THF was added within the first 30 min to prevent polymer precipitation. The reaction was stirred overnight and quenched with 5 M HCl for 5 min. The polymer was precipitated in methanol, then further purified by Soxhlet extraction in methanol, then acetone to collect a dark purple solid. NMR was used to confirm the expected ratio of monomers and determine the percent regioregularity of the polymers. **P3HT ^{1}H NMR** (300 MHz, $CDCl_3$), δ (ppm): 6.98 (s, 1H), 2.81 (t, 2H, *Th-CH_2 head-tail*), 2.61 (t, 2H, *Th-CH_2 head-head*), 2.49 (s, 3H, *α-tol-CH_3*), 1.71 (m, 2H), 1.34-1.46 (m, 6H), 0.91 (t, 3H). **P3Br$_{0.25}$HT ^{1}H NMR** (300 MHz, $CDCl_3$), δ (ppm): 6.98 (s, 1H), 3.43 (t, 2H*0.25), 2.83 (t, 2H, *Th-CH_2 head-tail*), 2.63 (t, 2H, *Th-CH_2 head-head*), 2.49 (s, 3H, *α-tol-CH_3*), 1.90 (m, 2H*0.25), 1.71 (m, 2H), 1.36-1.54 (m, 4H*0.25 + 6H*0.75), 0.92 (t, 3H*0.75). **P3Br$_{0.75}$HT** ^{1}H NMR (300 MHz, $CDCl_3$), δ (ppm): 6.98 (s, 1H), 3.43 (t, 2H*0.75), 2.83 (t, 2H, *Th-CH_2 head-tail*), 2.63 (t, 2H, *Th-CH_2 head-head*), 2.49 (s, 3H, *α-tol-CH_3*), 1.90 (m, 2H*0.75), 1.71 (m, 2H), 1.49 (m, 4H*0.75), 1.35 (m, 6H*0.25), 0.92 (t, 3H*0.25). **P3BrHT ^{1}H NMR** (300 MHz, $CDCl_3$), δ (ppm): 6.98 (s, 1H), 3.43 (t, 2H), 2.83 (t, 2H, *Th-CH_2 head-tail*), 2.63 (t, 2H, *Th-CH_2 head-head*), 2.49 (s, 3H, *α-tol-CH_3*), 1.90 (m, 2H), 1.73 (m, 2H), 1.45-1.54 (m, 4H).

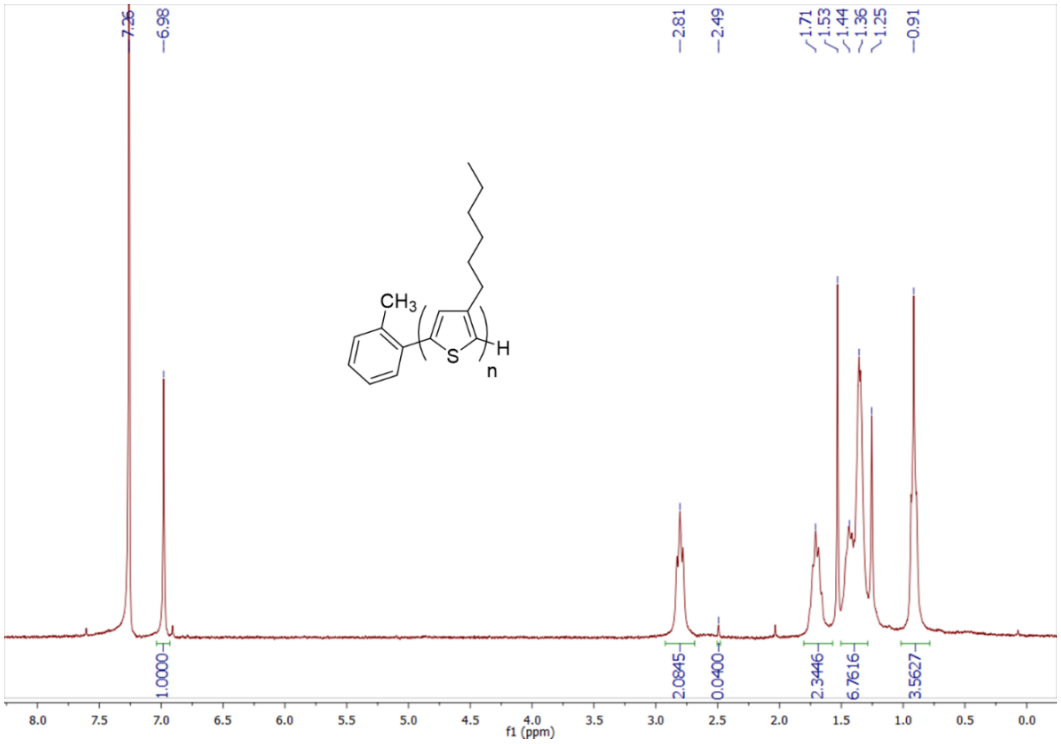

Figure 34: *[1]H NMR of P3HT, poly(3-hexylthiophene)*

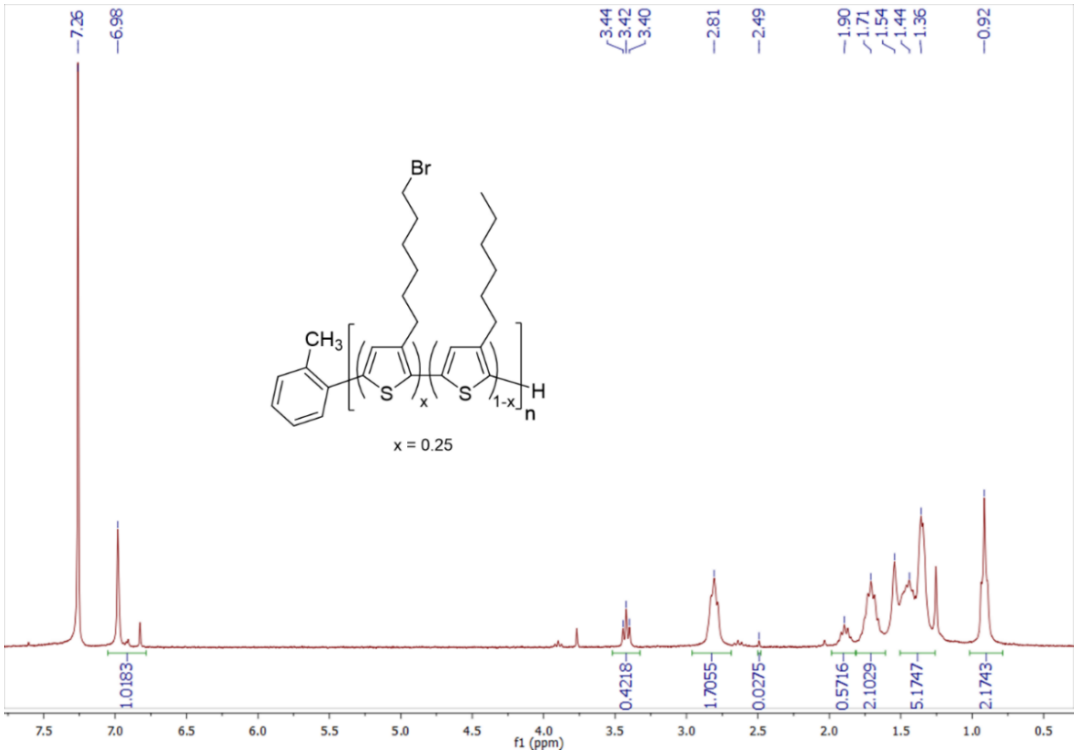

Figure 35: *[1]H NMR of P3Br$_{0.25}$HT, poly[(3-(6-bromohexyl)thiophene)-ran-(3-hexylthiophene)], 25% brominated monomer*

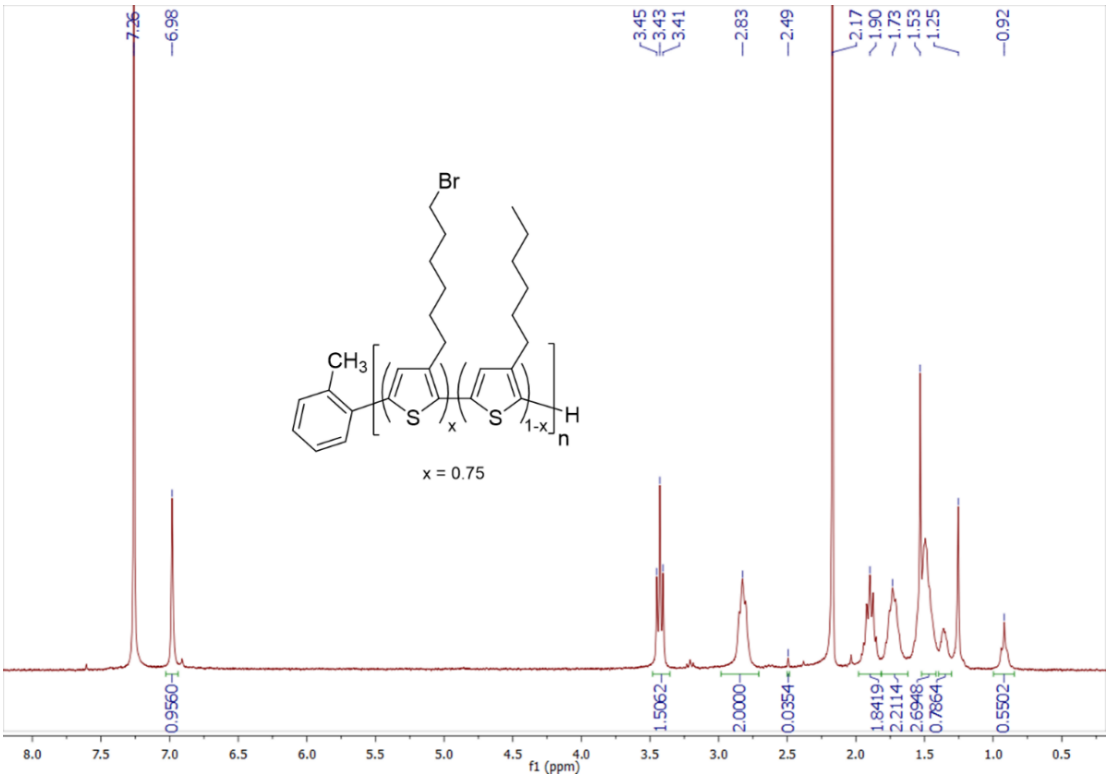

Figure 36: ^{1}H NMR of P3Br$_{0.75}$HT, poly[(3-(6-bromohexyl)thiophene)-ran-(3-hexylthiophene)], 75% brominated monomer

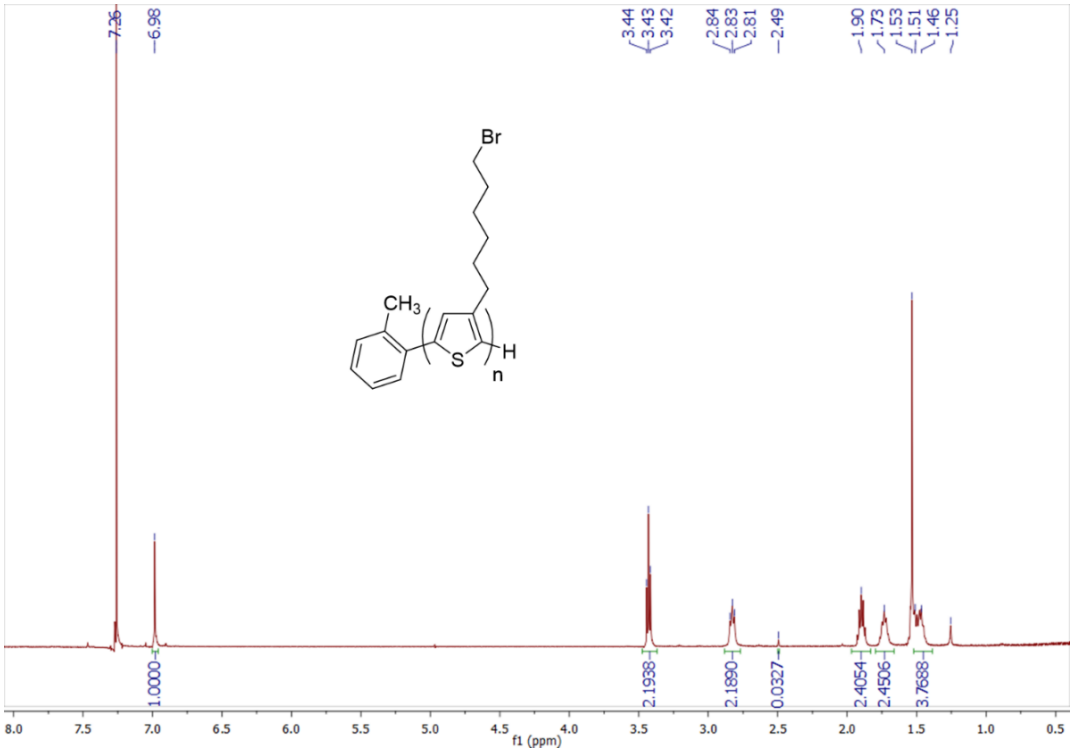

Figure 37: [1]H NMR of P3BrHT, poly(3-(6-bromohexyl)thiophene))

4.2.7 Post-Polymerization Functionalization

Poly(3-(6-hexylthioacetate)thiophene) (9): In a nitrogen atmosphere, (**8**) was dissolved (168 mg) in anhydrous THF (80 mL). Upon addition of potassium thioacetate (336 mg), the mixture was refluxed for 24 hr at 70° C. The reaction was monitored by NMR. Once complete, the crude mixture was filtered through Celite and rinsed with dichloromethane. The filtrate was dried *in vacuo* to afford a dark reddish solid. **^{1}H NMR** (300 MHz, $CDCl_3$), δ (ppm): 6.97 (s, 1H), 2.88 (t, 2H), 2.80 (t, 2H), 2.31 (s, 3H), 1.70 (m, 2H), 1.60 (m, 2H), 1.44 (m, 4H).

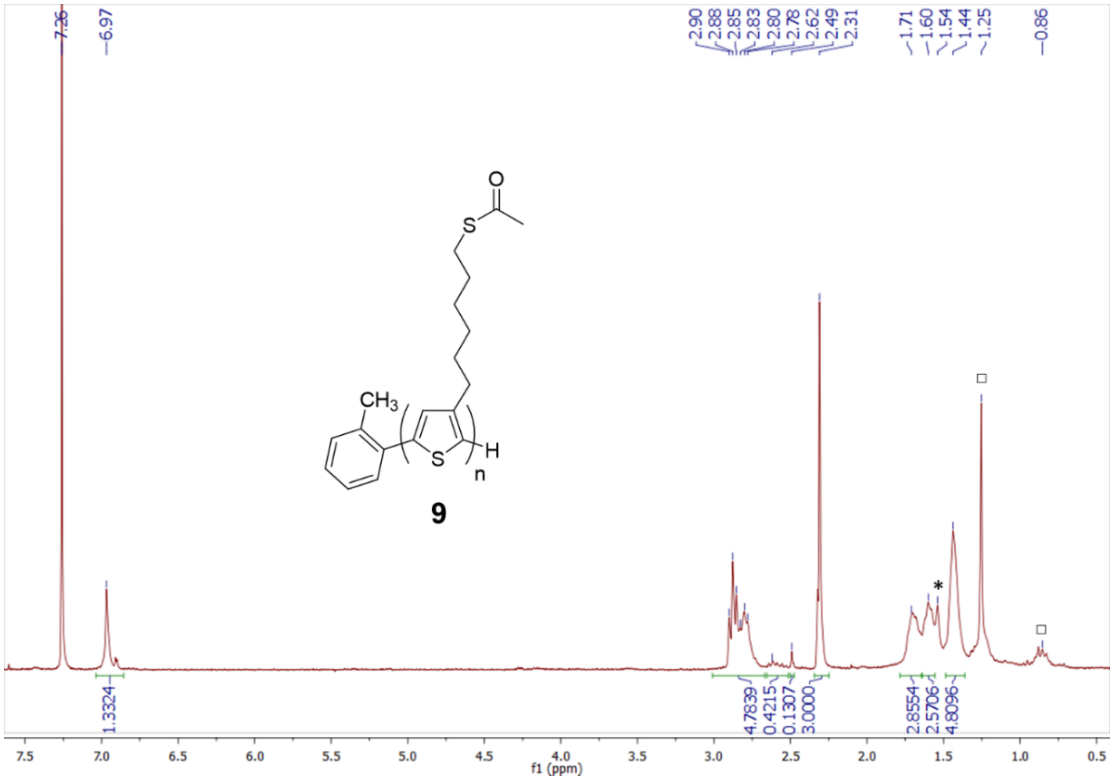

*Figure 38: ^{1}H NMR of **9**, poly(3-(6-hexylthioacetate)thiophene) *water □grease*

Poly(3-(6-mercaptohexylthiophene)) (10): Under nitrogen atmosphere, (**9**) (20 mg) was added to degassed THF (20 mL). Anhydrous methanol (0.6 mL) and sodium hydride (50 mg) were added at 0° C in an ice bath and stirred 1 hr. Acetic acid was added dropwise (0.4 mL) at room temperature. After addition of DI water, the organic layer was extracted with dichloromethane. Precipitate (**9**) was removed by filtration and the organic layer was dried by Na_2SO_4 and dried *in vacuo*. In the glovebox, the dried organic layer was redissolved in a minimum amount of chloroform, precipitated in methanol and filtered to afford a deep red solid in 65% yield. **^{1}H NMR** (300 MHz, $CDCl_3$), δ (ppm): 6.97 (s, 1H), 2.81 (t, 2H), 2.53 (t, 2H), 1.70 (m, 4H), 1.45 (m, H).

(10), disulfide reduction: Under nitrogen atmosphere, (**11**) (26 mg) was added to a 2.0 M solution of dimethylamine in THF (18 mL). Several conditions were tested (A-C). A: dithiothreitol (DTT) (39 mg) was added and stirred for 1 hr at room temperature. B: DTT (39 mg) was added and stirred at 40° C for 48 hr. C: An excess of DTT (64 mg) was added and stirred 48 hr at room temperature. Under condition C, an orange solution appeared, indicative of solubilized P3SHT while undissolved (**11**) was removed by filtration. The filtrate containing (**10**) was precipitated by methanol and filtered to collect dark red solid in 10% yield.

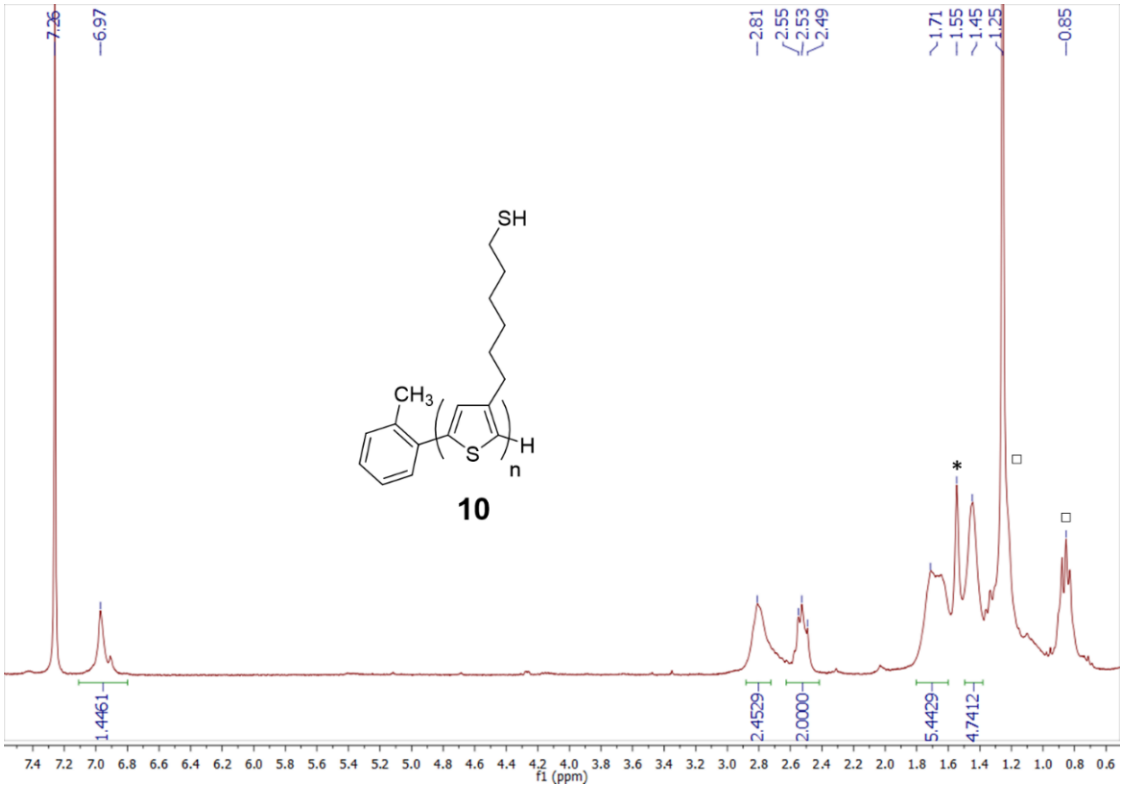

*Figure 39: [1]H NMR of **10**, poly(3-(6-mercaptohexylthiophene)) *water □grease*

4.2.8 Gel Fractions

Thick films for gel fraction studies were prepared from 15 mg/mL SBco or PB solutions in toluene with the following mass ratios: 100/1/0-2 SBco/I819/BIS, 100/1/0-20 SBco/I819/SH-P3HT-SH, 100/0-20 PB/P3BrHT, or 100/25/0-12.5 PB/$BrC_6H_{12}Br$/BHT. Samples were drop casted on tared glass slides, yielding films ~1 µm thickness, as determined by profilometry. Individual slides were exposed to UV light up to 60 s for SBco films and 10 min for PB films. Each sample was soaked in a petri dish of toluene for 24 hours and shielded from light to dissolve uncrosslinked polymer. Gel fractions were recovered, air-dried and weighed. Gel fractions were calculated by **Equation 1** where M_d is the mass of a dried gel fraction and M_i is the initial film mass.

$$Gel\ Fraction = \frac{M_d}{M_i} \qquad \textit{Equation 1}$$

4.2.9 General Thin Film Preparation

Neat $P3Br_xHT$ thin film samples were prepared from 5 mg/mL chlorobenzene solutions stirred at 100 °C under nitrogen overnight. Thin films of polymer blends were prepared similarly in 50/50 mass ratios of PB/P3HT with a total polymer concentration of 10 mg/mL. Molar equivalences of $P3Br_xHT$ were used with respect to degree of polymerization in order to retain equal conjugated backbone amounts to P3HT in blended samples. All glass and silicon substrates were cut to 1.5 cm x 1.5 cm squares and cleaned by first scrubbing with detergent, and then ultrasonicated 15 min each in DI water, acetone and isopropanol. Substrates were then rinsed with clean isopropanol and dried with a stream of air and further cleaned by 15 min of oxygen plasma. $P3Br_xHT$ solutions were filtered by a 0.45 µm syringe filters and blends were filtered with both 0.8 µm and 0.45 µm syringe filters before spin coating for 60 s at 2000 RPM. Films were annealed at 120 °C for 15 min on a hot plate. Appropriate samples were UV cured for 10 min by a UVGL-25 Compact 4 W UV lamp equipped with 254 nm light at a 3 cm distance from the source.

4.2.10 Film Imaging

An Olympus OLS4100 laser microscope was used to measure film thicknesses by profilometry, collect optical images for morphological analysis (100X zoom), and view films to determine crack onset strains (20x zoom). Image coloring was modified for clarity.

4.2.11 DSC

DSC was performed on the Mettler Toledo DSC in standard 40 µL aluminum pans with a heat-cool cycle between 25 °C and 330 °C at a heating/cooling rate of 15 °C/min with a 50 mL/min nitrogen flow. DSC samples were first tested by thermogravimetric analysis (TGA) on the Mettler Toledo TGA 3+ to ensure stability up to 330 °C. TGA measurements were carried out in standard 40 µL aluminum pans at a 15 °C/min heating rate with sample weights of 2.5-3.0 mg under a 50 mL/min nitrogen flow.

4.2.12 Crack Onset Strain

Glass substrates were cleaned according to above procedure. An aqueous dispersion of PEDOT/PSS was syringe filtered through a 0.45 µm filter and spin coated onto the glass substrates for 60 s at 2000 RPM as the sacrificial transfer layer of 30 nm thickness. Films were then annealed in air at 140 °C for 20 min. A second layer of the neat or blend solution was spin coated, annealed and UV cured in air as described. PDMS slabs were prepared to a 2-3 mm thickness in 10/1 (v/v) silicone/curing agent ratio by pouring a thoroughly blended mixture over glass substrates in a metal pan. Air bubbles were removed with 2 hours of vacuum and the PDMS was cured under low heat overnight in ambient air. PDMS was trimmed and peeled from the glass to yield free standing slabs. The neat and blended polymer layers were transferred onto PDMS substrates by directly contacting the film to PDMS and submerging in water for 90 min, allowing the PEDOT/PSS layer to dissipate in the water, and separate from the glass substrate. Crack onset strain measurements were viewed by loading samples on a lab-assembled strain stage and incrementally straining

under a microscope until cracks of at least 20 µm length appeared on the film. Results were averaged over 3 samples.

4.2.13 OFETs

Bottom gate top contact OFETs were prepared on silicon substrates, which were cleaned according to procedure. The substrate surface was modified with hexamethyldisilazane by spin coating in air for 60 s at 3000 RPM and annealing in a nitrogen atmosphere for 10 min at 120 °C. The following steps were performed under nitrogen. Spin coating and annealing were performed as described. Gold electrodes were evaporated onto the films from an alumina-coated Mo boat through shadow masks at a rate of 2 Å/s to 2 kÅ thickness producing devices with 1000 µm length (L) and 50 µm width (W). A portion of the surface was etched to reveal silicon onto which an indium gate electrode was applied. Mobility (μ) was calculated in the linear regime by the slope of drain current (I_D) vs gate voltage (V_G) curves under a negative gate bias sweep of 0 V to -100 V with the drain voltage (V_D) set to -40 V. The fit follows the equation using the threshold voltage (V_T) and the dielectric capacitance (C) of 10 nF/cm^2:

$$I_D = \mu\, C\, \frac{W}{L}(V_G - V_T)\, V_D$$

Equation 2

Each sample was tested for 15-20 devices total across 3 substrates.

Strained OFETs were fabricated in the bottom gate bottom contact architecture on silicon substrates which were cleaned according to procedure without oxygen plasma. Gold electrodes were evaporated directly onto the silicon substrates from an alumina-coated Mo boat through shadow masks at a rate of 2 Å/s to reach a 2 kÅ thickness to produce devices 1000 µm long and 50 µm wide. Device performance was found to be unaffected by HMDS surface modification and were thus prepared without a self-assembled monolayer. A portion of the surface was etched to reveal silicon onto which an indium

gate electrode was applied. As for crack onset strain samples, films were prepared on glass substrates and transferred onto ~1 mm thick PDMS cured with 15/1 (v/v) silicone/curing agent. To measure mobility, a PB/P3Br$_x$HT on PDMS was strained by a lab-assembled strain stage and contacted to electrodes on silicon where the strain is parallel to the charge transfer direction. A top glass layer was used to sandwich the device and retain strain using binder clips during measurements. A sample was tested for each strain using 9 ± 3 devices per substrate. Mobility was calculated in the same manner as for the bottom gate top contact OFETs.

4.2.14 UV-vis

UV-Vis spectra were measured by the Varian Cary 5000. Thick films of SBco and PB were prepared from 25 mg/mL toluene and 10 mg/mL chlorobenzene solutions, respectively, and drop casted onto KBr salt plates. Crosslinkable SBco films were prepared with added photoinitiator in 100/1/1 mass ratio of SBco/I819/crosslinker, with crosslinkers being BIS or SH-P3HT-SH. Crosslinkable PB films were prepared in a 100/10 mass ratio of PB/P3BrHT or 100/25/0-12.5 mass ratios of PB/BrC_6H_{12}Br/BHT.

Solution absorption of P3Br$_x$HT was collected in quartz cuvettes with a 1 cm pathlength in a 0.02 mg/mL concentration of chlorobenzene at room temperature. Thin films of neat P3Br$_x$HT and blended PB/P3Br$_x$HT samples were prepared on glass substrates cleaned according to the discussed procedure. Solutions for films were prepared, spin coated, and annealed as described in air. Absorbance spectra of a blank glass slide was subtracted and normalized to zero at 800 nm.

Fits were determined by weakly interacting H-aggregate model as described in literature.[123–126] The coupled vibronic transitions that determine the absorbance spectrum of P3HT were modeled with the following equation based on gaussian fits:

$$A(E) \propto \sum_{m=0}\left(\frac{S^m}{m!}\right) \times \left(1 - \frac{We^{-S}}{2E_p}\sum_{n\neq m}\frac{S^n}{n!(n-m)}\right)^2 \times \exp\left(\frac{-(E-E_{00}-mE_p-\frac{1}{2}WS^m e^{-S})^2}{2\sigma^2}\right)$$ *Equation 3*

where E is photon energy and A is the absorbance spectrum as a function of photon energy. W is the free exciton bandwidth, which is associated with nearest neighbor excitonic coupling. When coupled, the energy is dispersed, and the width of this dispersion is equal to W (which is roughly four times the nearest neighbor coupling). A low value for W indicates better ordering of aggregates, which means that W is inversely correlated to conjugation length.[126] S in the Huang-Rhys factor, which is assumed to be 1 for most forms of P3HT.[123,124] E_p is the intermolecular vibration energy. When $S = 1$, it is the difference in energy between the excited state vibrational levels. A value of 0.179 eV is used based on results from Raman spectroscopy.[127] E_{00} is the energy of the 0 → 0 vibronic transition, which is only allowed if the aggregates are slightly disordered.[123] σ is the gaussian linewidth and the m and n are the ground state and excited state transitions respectively. E_{00}, W, σ and a scaling factor were determined by fitting Equation 3 to the experimentally determined absorption spectra. Fits were performed with a python script that uses SciPy's non-linear least square regression function. The 95% confidence intervals for each parameter were extracted from the least square regression fit. The fit was performed on absorbance data for $\mathrm{E} \in [1.95\ \mathrm{eV}, 2.25\ \mathrm{eV}]$ since higher energy absorbance is dominated by amorphous absorption.[128] The fit used $m = 3$ ground states and $n = 2$ excited states. The fitted integrated aggregate absorbance was determined for $\mathrm{E} \in [1.75\ \mathrm{eV}, 3\ \mathrm{eV}]$ and the integrated amorphous absorbance was determined for $\mathrm{E} \in [2\ \mathrm{eV}, 3\ \mathrm{eV}]$.

Samples for strained UV-vis absorption were prepared as described for crack onset strain. Films were pulled on a strain stage and attached to a glass substrate with binder clips to retain strain during measurement. UV-Vis spectra were measured by the Varian Cary 5000 and absorption was normalized to zero at 800 nm after subtraction of a blank glass slide.

4.3 Composite Material Selection: Synthesis and Crosslinking Proof of Concept

4.3.1 Target π-Conjugated Polymers

Poly(3-hexylthiophene) (P3HT) was chosen as foundational structure for the π-conjugated polymer in the elastomer/π-conjugated polymer system because it can be prepared with a controlled synthesis and is relatively stable, which is suitable for the target processing conditions of this work. We will first discuss the preparation of the three target polymers chosen for potential crosslinking (**Figure 40**). One sample contains end group termination by thiols on P3HT, SH-P3HT-SH. Two target polymers have side chain functionalization by thiol or bromide groups, poly(3-(6-mercaptohexylthiophene)) (P3SHT) and poly(3-(6-bromohexylthiophene)) (P3BrHT), respectively. While end group functionalization is less demanding to synthesize, the concentration of functional groups is limited. Side chains functionalization, however, allows for a higher concentrations and thus greater reactivity and potential for elastomer crosslinking.

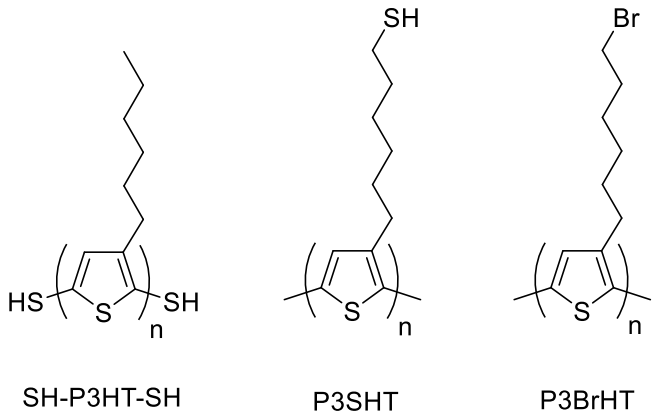

***Figure 40**: Targeted thiophene-based functionalized π-conjugated polymers: thiol-terminated poly(3-hexylthiophene), poly(3-(6-mercaptohexylthiophene)) and poly(3-(6-bromohexylthiophene)).*

Thiols were selected as functional groups for the π-conjugated polymer due to the well-known thiol-alkene "click" chemistry, which can proceed with polymers under UV light in the presence of chemical photoinitiator.[114–117] Any unreacted thiols also have the potential to introduce self-healing properties

through reversible thiol-disulfide reactions.[129–136] While thiols have been used as small molecule crosslinkers in elastomers, they have not been exemplified as crosslinking agents in elastomer/π-conjugated polymer blends, and is explored in this research. An alkyl bromide side chain was chosen because has been demonstrated as an effective UV-activated crosslinking group in conjugated polymers without the use of external chemical initiators.[106–110,137] Its reactivity to alkenes, particularly elastomers, has not been studied and is discussed in this work. With either group, the direct bonding of π-conjugated polymer and elastomer has not previously been reported in literature and has the potential to improve mechanical performance of organic stretchable electronic materials.

Low molecular weight polymers (<5 kg/mol) were synthesized for initial crosslinking studies and are most appropriate for crosslinking tests due to its improved solubility. After presenting proof of concept for crosslinking of π-conjugated polymer with elastomer, high molecular weight polymers were utilized for further study.

4.3.2 End Group Functionalization

Thiol-terminated poly(3-hexylthiophene) (SH-P3HT-SH) was synthesized according to literature procedure from commercial monomer.[122] A shorter polymer chain was advantageous for this polymer because it increases the total concentration of thiols for enhanced crosslinking potential. ^{1}H NMR characterization of SH-P3HT-SH was in agreement with literature and MALDI-TOF was utilized for end group analysis (**Figure 41**). MALDI-TOF indicated that a majority of the polymer contained at least one thiol, with the primary peak containing two. The thiol end group conversion determined by MALDI indicated successful synthesis of target SH-P3HT-SH with sufficient end group functionalization to proceed with further crosslinking tests.

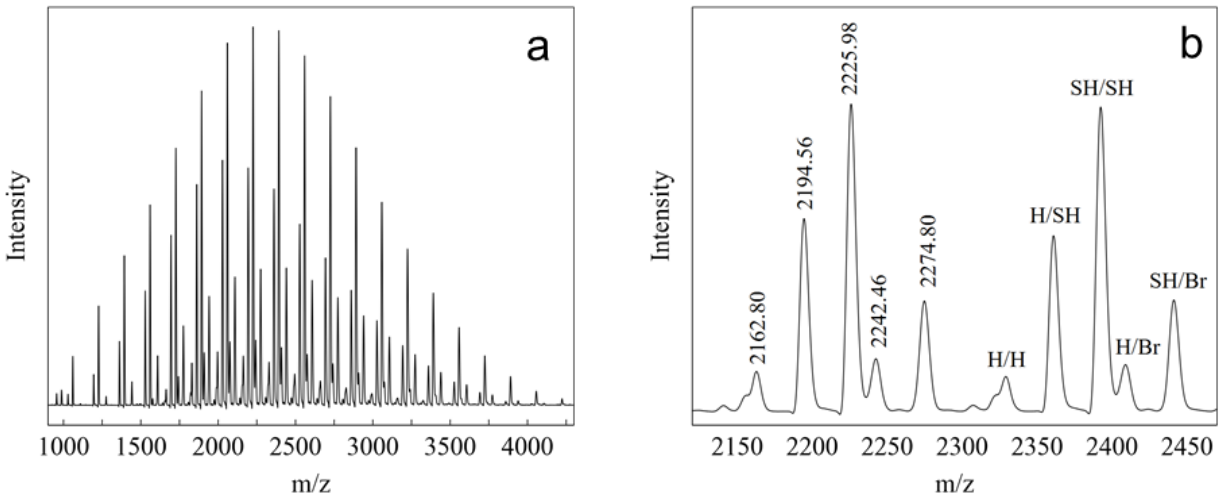

Figure 41: MALDI-TOF of SH-P3HT-SH (a) full spectrum and (b) zoomed to view end groups.

4.3.3 Side Chain Functionalization

To synthesize P3SHT and P3BrHT, a five-step synthesis was performed to yield a common monomer with slight modifications to literature procedures (Scheme 1). First, a methoxyaryl protecting group was added to a dibrominated alkyl chain (**1**) by ether linkage, followed by cross-coupling with the thiophene ring (**2**).[138,139] The protecting group was then replaced (**3**) to generate the UV-active bromide side chain.[3] The thiophene ring was halogenated in preparation for polymerization by bromide (**4**) and iodide groups (**5**) to produce the target monomer.[140–142] Side chain modification proceeded with bromide substitution by thioacetate (**6**), and deprotected to yield thiol (**7**) (Scheme 2).[143] An alternate route to sulfur-functionalized monomers was also pursued with thiophene halogenation following thioacetate substitution, but minimal iodinated thiophene was generated.

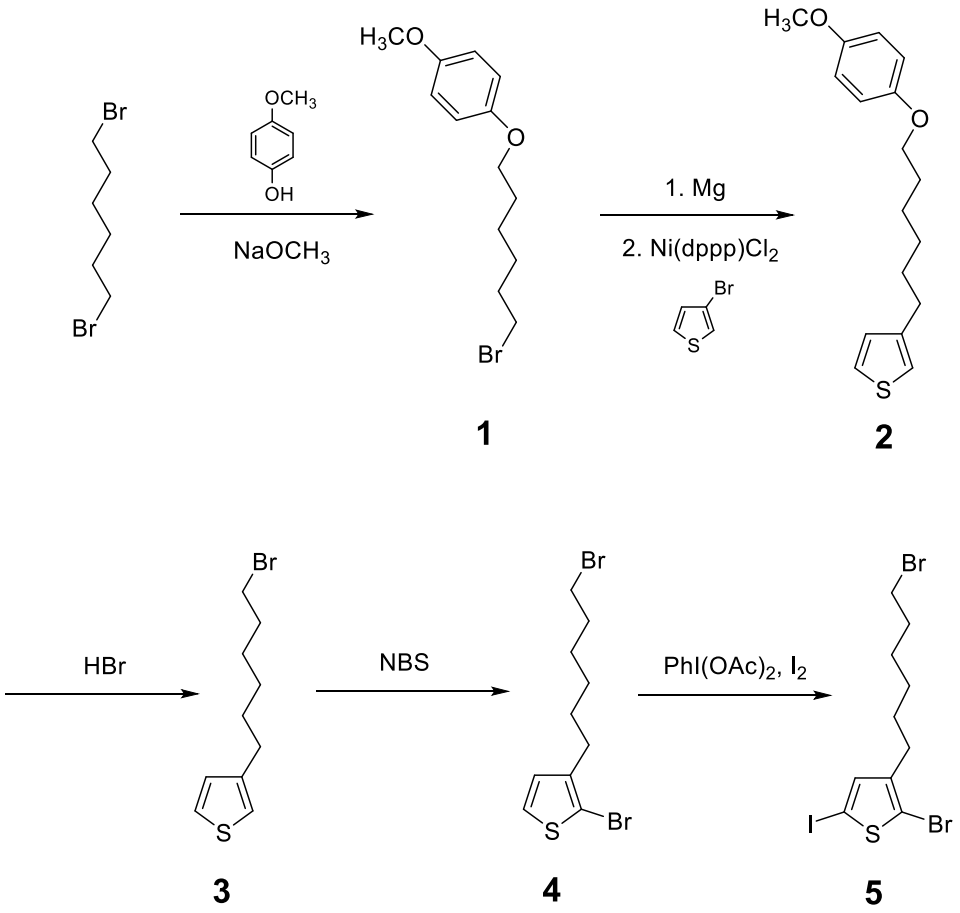

Scheme 1: Synthesis of monomer for side-chain functionalized polymers.

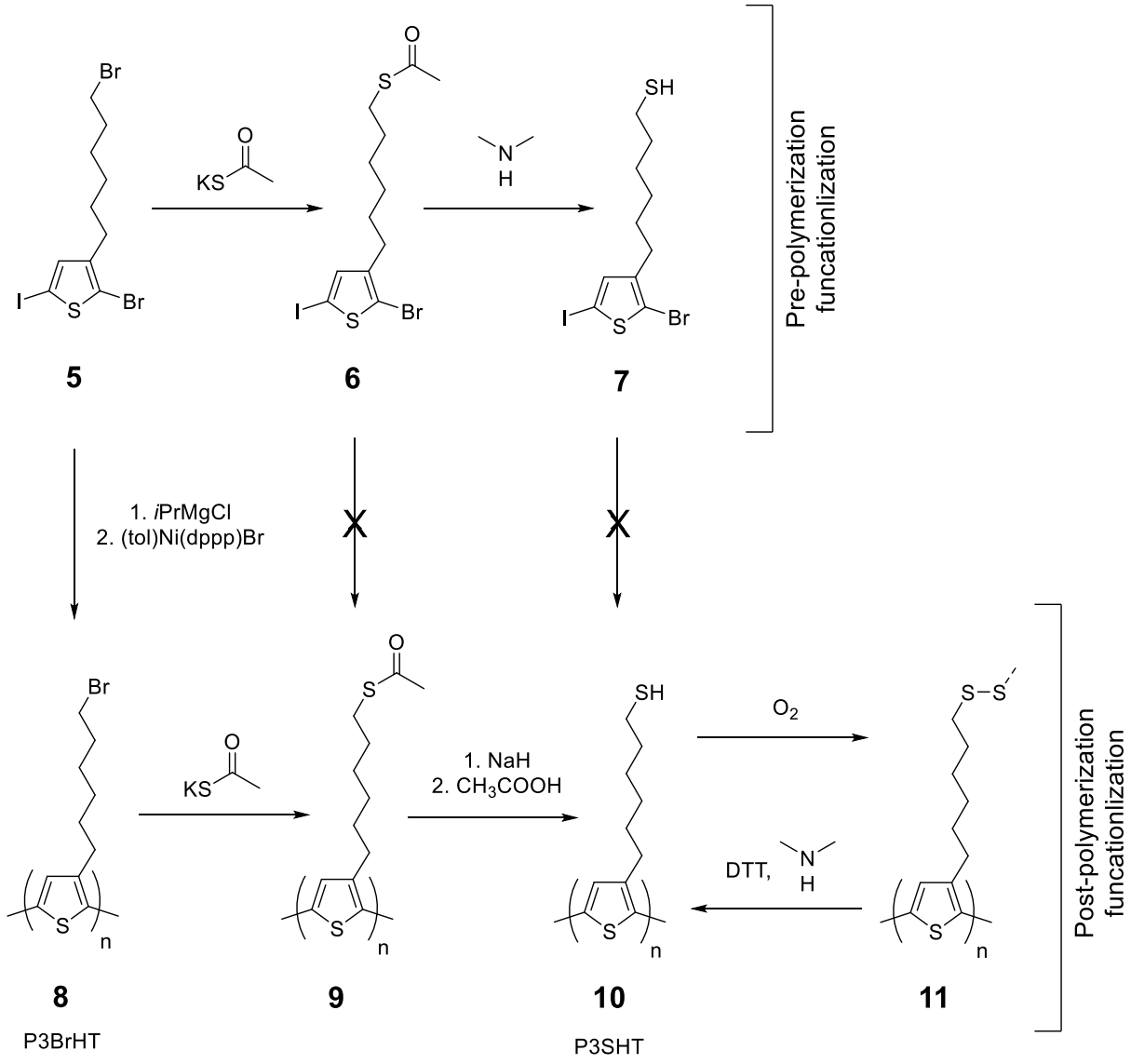

Scheme 2: Polymerization for P3BrHT and routes for synthesis of P3SHT by pre-functionalization and post-functionalization by sulfur.

Polymerization was continued with 3 pre-functionalized monomers containing bromide (**5**), thioacetate (**6**) or thiol (**7**) groups on the hexyl side chain. Polymerization by sulfur pre-functionalized thiophene monomers was not present in literature and was preferred over post-polymerization functionalization. Pre-polymerization has greater control over functional group content due to higher reactivity of monomers and the ability to separate unreacted material. However, attempts to polymerize

thiol pre-functionalized monomer (**7**) or thioacetate protected sulfur (**6**) led to failed polymerizations and was thus not suitable for synthesis of P3SHT. NMR revealed the presence of quenched monomer, indicating that thiophene chain growth was deactivated, likely due to sulfur-nickel activity.[144–151] On the other hand, P3BrHT polymerized successfully and was attainable for elastomer crosslinking tests (**5**).[17,142,152] P3SHT was instead synthesized by post-polymerization functionalization following P3BrHT synthesis.[143] While thioacetate deprotection by an amine was accomplished for the monomer (**7**), hydride proved more effective for the production of thiol for P3SHT.[153] NMR characterization confirmed successful synthesis and post-polymerization conversion of the two target side chain functionalized polymers, P3SHT and P3BrHT.

An important observation made for P3SHT was that it exhibited decreasing solubility during the purification procedure and continuously precipitated in organic solvent. The insoluble precipitate was attributed to the formation of disulfide bonds forming a crosslinked network (**11**).[143] The insolubility of this material and weak spectroscopic signals of thiols and disulfides led to difficulty characterizing the material. Storage of P3SHT in the dark under air or vacuum led to further insolubility over the course of a day, suggesting that the thiols in the polymer underwent oxidation readily. On the other hand, P3BrHT remained soluble after storage in the dark in air for more than a year. Several reaction conditions were performed to reduce the disulfide bond and recover P3SHT. Positive indication of thiol formation was the transition from a red insoluble solid to a clear, bright orange solution. The common disulfide reducing agent dithiothreitol alone did not lead to increased polymer solubility but was modestly successful with the addition of amine. Low yields of solubilized P3SHT were produced while an undissolved portion also remained. Once again, recovered P3SHT was only partially soluble after storage under vacuum, indicating the reformation of self-crosslinked material (**11**). The lack of controllable crosslinking rendered the polymer unusable for elastomer bonding.

The three target polymers, SH-P3HT-SH, P3SHT, and P3BrHT were characterized for molecular weight by several techniques (**Table 4**). ^{1}H NMR was used to quantify the degree of polymerization (DP) for

P3SHT and P3BrHT by tolyl end group analysis. Only P3BrHT was characterized for the number average molecular weight (M_n) and dispersity ($Đ$) by size exclusion chromatography to avoid potentially damaging thiol-binding in the instrument. M_n and DP for P3SHT was determined by its P3BrHT precursor. The average molecular weight for SH-P3HT-SH was assumed to be the peak DP by MALDI. Analysis confirms that three low molecular weight polymers were successfully synthesized and two samples, SH-P3HT-SH and P3BrHT, were chosen for continued study of crosslinking with elastomers.

*Table 4: Characterization of polymer molecular weight. *Determined by MALDI-TOF*

Polymer	M_n kg/mol ($Đ$)	DP
SH-P3HT-SH*	2.4	14
P3BrHT	4.3 (1.3)	31
P3SHT	3.1 (1.3)	24

4.3.4 Crosslinking Feasibility

Once the functionalized π-conjugated polymers SH-P3HT-SH and P3BrHT were synthesized, their ability to covalently bond with elastomers was investigated. The elastomers chosen for the system contain alkenes, which are known to crosslink through radical intermediates.[111–113,154,155] Reactive π-conjugated polymer bonding was also compared to small molecule references containing thiol or bromide functional groups. To confirm the viability of light-initiated crosslinking, these systems were first analyzed by UV-vis spectroscopy. Gel fractions experiments were then executed to quantify the proportion of bonded materials as evidence of covalent bond formation between polymer chains.[47,156,157] Gel fractions also indicated clear visual evidence of crosslinking by decreased solubility compared to its constituent parts. These characterization techniques for the first time validated direct crosslinking between an elastomer and π-conjugated polymer as an approach for developing stretchable electronic materials.

4.3.5 Thiol/Elastomer Crosslinking

The materials required for polymeric thiol-ene crosslinking included an alkene elastomer, thiol crosslinkers and a photoinitiator (**Scheme 3**). A styrene-butadiene copolymer (SBco) was chosen as the elastomer, which is similar to previously thiol-crosslinked polymers.[158–160] Reference tests comparing thiol crosslinkers were performed using 1,4-butanediol bis(thioglycolate) (BIS), a small molecule crosslinker containing two thiols analogous to SH-P3HT-SH. Radicals in the system were introduced by UV irradiation of the photoinitiator phenylbis(2,4,6-trimethylbenzoyl)phosphine oxide, also known as Irgacure 819 (I819), by cleavage of the ketone-phosphorus bond (**Scheme 4**).[156,161]

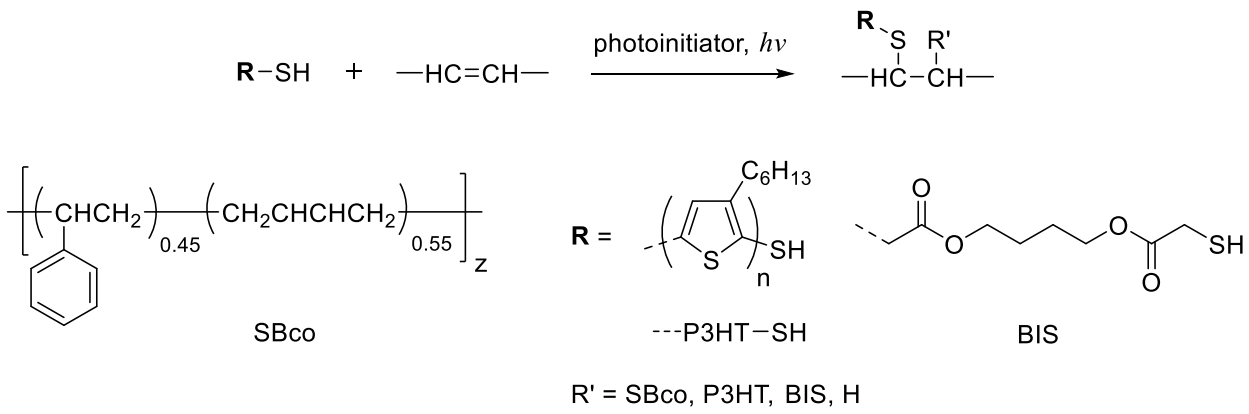

Scheme 3: UV-activated crosslinking between an alkene elastomer (SBco) and thiol π-conjugated polymer (SH-P3HT-SH) or thiol small molecule (BIS).

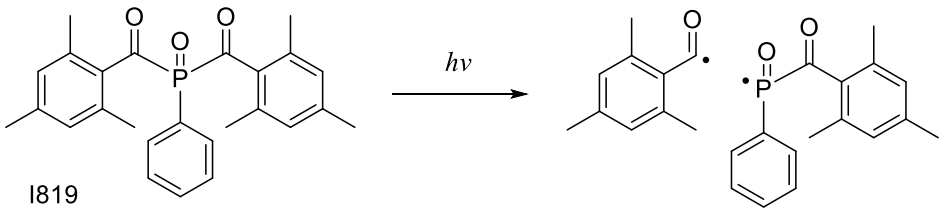

Scheme 4: Radical generation by the photoinitiator (I819) upon UV light exposure.

In order for SH-P3HT-SH to bond effectively with an elastomer under UV light activation, the absorption of materials was considered. Standard UV lamps emit 254 and 365 nm wavelengths and 254 nm was chosen since SH-P3HT-SH fluoresced under 365 nm UV light, which would compete with I819 absorption. A curing time of 60 s was chosen for our studies given that similar light-activated systems exhibited crosslinking after only seconds of UV exposure.[156,159,160] UV-vis spectroscopy of SBco elastomer films containing I189 photoinitiator and either BIS or SH-P3HT-SH crosslinkers indicated distinct absorption of each component except for the BIS crosslinker (**Figure 42**). For these samples, a decreased absorption of I819 was observed after 60 s of UV curing, indicating radical generation and the potential for elastomer crosslinking.

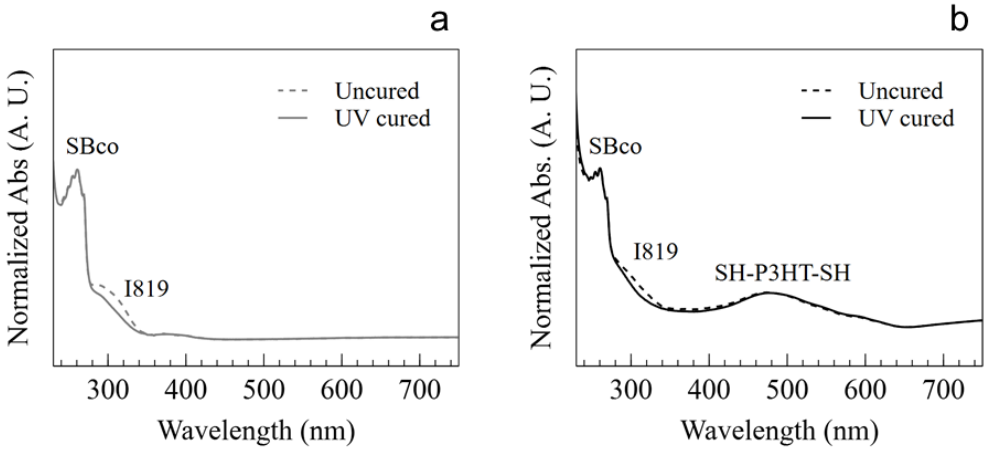

Figure 42: UV-vis absorption of uncured and UV cured films of SBco with 1% I819 and (a) 1% BIS or (b) 1% SH-P3HT-SH crosslinkers.

To confirm crosslinking of thiols with SBco, gel fractions were calculated by comparing the weights of initial films to dried gels. Films were soaked in solvent for 24 hr to allow any uncrosslinked polymers to diffuse into solution while the insoluble gel remained intact. Samples with equimolar thiol content of BIS and SH-P3HT-SH were compared across varied crosslinker concentrations. For both BIS and SH-P3HT-SH, increasing the concentration of thiols increased the insoluble gel fraction, demonstrating greater

crosslinking (**Figure 43**). SH-P3HT-SH, however, had considerably lower gel fractions than BIS. This may be because liquid BIS is better dispersed into SBco whereas the semicrystallinity of SH-P3HT-SH leads to separation from SBco. The crosslinking of SH-P3HT-SH to SBco is evident by the presence of an insoluble polymer network from gel fraction results, signifying successful covalent bonding between a π-conjugated polymer and elastomer.

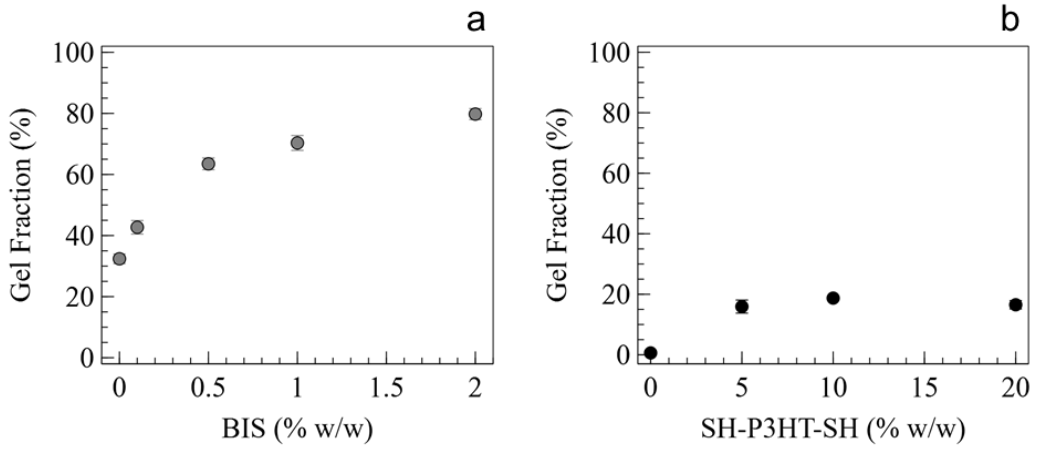

Figure 43: Gel fractions of SBco films with 1% I819 and (a) 0-2% BIS or (b) 0-20% SH-P3HT-SH.

Attempts to verify crosslinking by FTIR did not yield fruitful results due to the weak intensity and low concentration of sulfur bonds. More intense sulfur bond peaks were also undetected by Raman spectroscopy due the fluorescence of SH-P3HT-SH. One observation made between the gel fraction tests of SBco/BIS and SBco/SH-P3HT-SH is the inconsistent solubility of SBco without crosslinker. This variability was attributed to SBco's only moderate solubility and the fluctuating consistency of films associated with the drop cast processing. To address this issue, following experiments used solid *cis*-PB as the elastomer which had greater solubility and the same alkene groups available for radical crosslinking.

4.3.6 Bromide/Elastomer Crosslinking

The use of P3BrHT as a crosslinkable π-conjugated polymer comes with a few advantages over SH-P3HT-SH. Firstly, functionalization on the side chain allows for a higher concentration of functional groups per polymer chain, which is independent of polymer molecular weight. This concentration can be tuned by copolymerization with non-functionalized monomers. Functional group concentration for end groups, however, is dependent on polymer molecular weight, which decreases with longer chains. This is important to consider since higher P3HT molecular weights are correlated with improved electrical properties.[12,13,162] Furthermore, bromide functionalization does not require the use of an external photoinitiator since the bromide group acts as both a radical initiator and crosslinker, simplifying the crosslinking system to only the elastomer and π-conjugated polymer (**Scheme 5**).

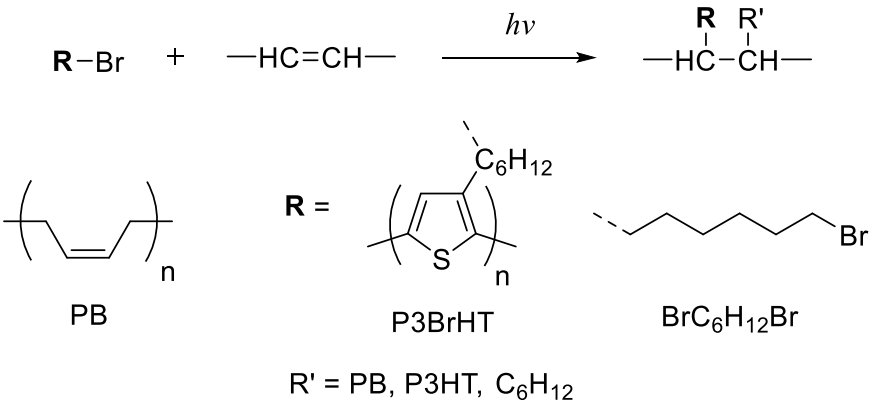

Scheme 5: UV-activated crosslinking between an alkene elastomer (PB) and bromide π-conjugated polymer (P3BrHT) or bromide small molecule ($BrC_6H_{12}Br$).

In line with literature, bromide-functionalized curing with PB was performed using 254 nm light with up to 10 min of UV exposure.[106] The non-conjugated reference crosslinker tested was 1,6-dibromohexane ($BrC_6H_{12}Br$). UV-vis spectroscopy of PB with $BrC_6H_{12}Br$ or P3BrHT indicates no competing absorption at 254 nm implying adequate material choices for light-activated crosslinking (**Figure 44**). Previously, alkylbromide crosslinking has only been demonstrated for π-conjugated polymers with

functionalized side chains and not for unsaturated elastomers.[106–110,137] To test the ability of an alkylbromide group to bond to PB, gel fraction tests were performed for PB using $BrC_6H_{12}Br$ as the crosslinker. Gel fractions were observed for samples UV cured for 10 min, but insoluble gels were not found for uncured PB/$BrC_6H_{12}Br$. This illustrates that a bromoalkyl molecule is an appropriate choice for photo-activated crosslinking with an alkene polymer.

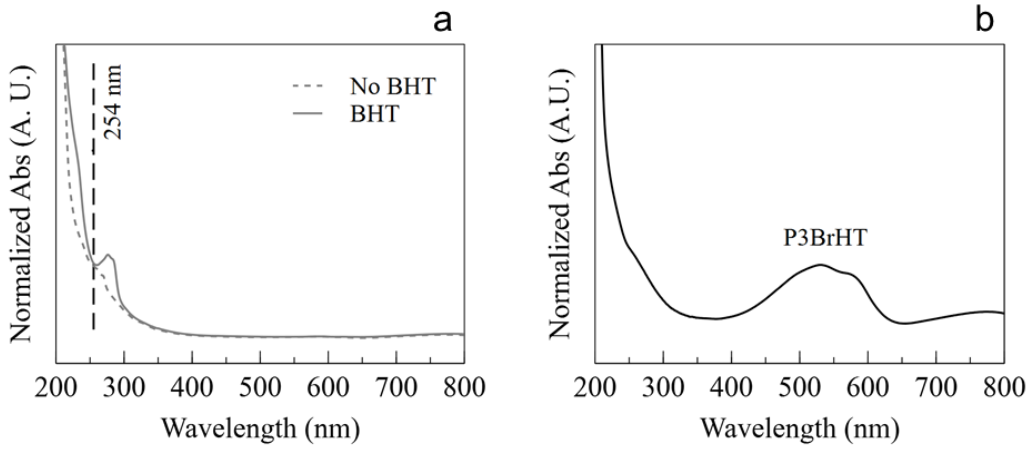

Figure 44: UV-vis absorption of (a) PB/$Br_6H_{12}Br$ film with and without BHT and (b) PB/P3BrHT film.

Crosslinking by alkylbromide side chains is thought to occur by homolytic cleavage of the C-Br bond under UV light, but has not been studied in detail with functionalized π-conjugated polymers.[106,118–120] To explore the presence of radicals and their efficacy on crosslinking, PB/$BrC_6H_{12}Br$ films were tested for gelation with an added radical scavenger, 3,5-di-*tert*-butyl-4-hydroxytoluene (BHT). UV cured films with BHT had not formed gel fractions, indicating successful inhibition of crosslinking. To ensure that the lack of gelation was not due to aromatic light absorption by BHT, UV-vis spectra was collected revealing no absorption at 254 nm by BHT (**Figure 44**). This reinforces the notion that crosslinking in the explored system occurs by a radical-mediated process.

With crosslinking of PB established by $BrC_6H_{12}Br$, gel fraction studies were carried out for PB/P3BrHT to introduce the conductive component for a stretchable electronic material. Attempts to

characterize crosslinking in films by dynamic mechanical analysis did not lead to conclusive results due to the highly segregated nature of the materials and the associated surface roughness. Films for gel fractions were prepared with varying P3BrHT concentration and curing time (**Figure 45**). Higher gel fraction percentages were correlated to higher proportions of P3BrHT, specifically higher proportions of crosslinkable bromide groups. With a P3BrHT proportion as little as 1% and as much as 20%, curing led to 17.4% and 70.6% gel fractions, respectively. In both cases, gel fractions had masses larger than the initial P3BrHT composition, revealing that crosslinking must have occurred between both polymers and not solely P3BrHT. With varied UV curing time, greater fractions were found for longer exposure, likely allowing for greater bromide side chain initiation and insoluble polymer network formation. As a reference, PB-only films formed no gels, showing that P3BrHT is indeed the bonding source. In comparison to gel fractions of SBco/SH-P3HT-SH (**Figure 43**), PB/P3BrHT had notably greater crosslinking as quantified by gel fractions. Between SH-P3HT-SH and P3BrHT, the latter was the favorable material chosen for continued for study of a crosslinkable elastomer/π-conjugated polymer system. The gel fraction results of PB/P3BrHT demonstrate evidence of covalently linked π-conjugated polymer and elastomer via UV curing applicable to stretchable electronics.

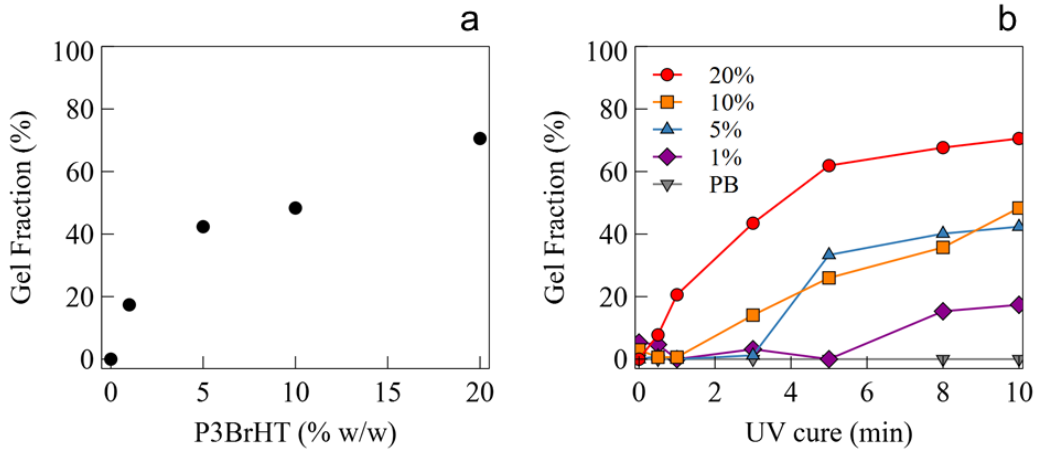

Figure 45: Gel fractions of PB/P3BrHT as a function of (a) P3BrHT concentration and (b) UV curing time.

4.4 Composite Analysis: Mechanical Behavior, Electrical Properties, and Polymer Packing

4.4.1 π-Conjugated Polymer Synthesis

Compatibilization analysis was completed with the selection of PB elastomer and P3BrHT functionalized π-conjugated polymer. To control the degree of order and crosslinking, four semiconducting polymers were synthesized: poly(3-hexylthiophene), two sets of poly[(3-(6-bromohexyl)thiophene)-*ran*-(3-hexylthiophene)], and poly(3-(6-bromohexyl)thiophene) (**Scheme 6**). The random copolymer was prepared with 25% and 75% proportions of bromohexyl side chain monomer relative to the non-functionalized hexyl side chain monomer. Polymers are denoted as $P3Br_xHT$, where x is the fraction of bromide-functionalized monomer feed ratio (x = 0-1), as confirmed by NMR characterization. To account for the electrical performance of the π-conjugated polymer, the molecular weight was increased to ~20 kg/mol to improve charge mobility in devices.[12,30] Characterization by SEC and NMR confirmed the monomer feed ratio and indicated comparable number-average molecular weight (M_n) and regioregularity (RR) of polymers (**Table 5**). These factors are important considerations to isolate the effects of side chain functionalization and reduce the structural influence of molecular weight and RR on electrical and mechanical properties.

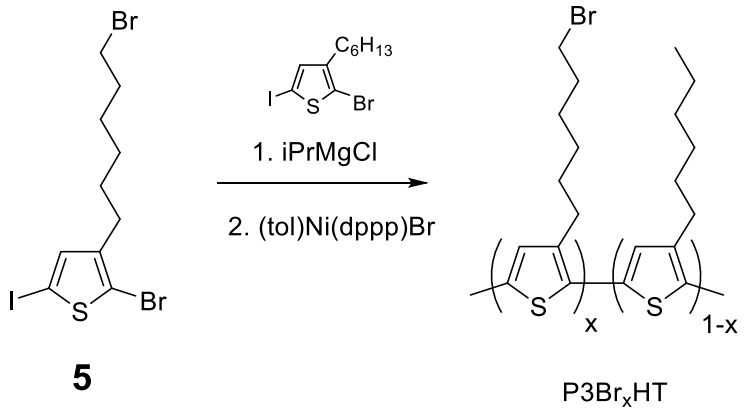

Scheme 6: Polymerization of poly[(3-(6-bromohexyl)thiophene)-ran-(3-hexylthiophene)] (P3BrxHT) where x = 0, 0.25, 0.50, 0.75, 1.

Table 5: Number-average molecular weight (M_n) and dispersity (Đ) of P3Br$_x$HT characterized via SEC. Regioregularity (RR) was determined by NMR. †L denotes low molecular weight.

Polymer	M_n	Đ	RR
P3HT	19.1	1.2	95%
P3Br$_{0.25}$HT	20.7	1.2	95%
P3Br$_{0.75}$HT	24.7	<1.1	95%
P3BrHT	15.6	1.2	>99%
P3BrHT-L†	4.3	1.3	92%

This polymer system uses scalable techniques, requiring only solvent for simple solution processability to produce the composite and low intensity UV-light to crosslink the film. Blended polymer composites were prepared by spin coating thin films to a 30 nm thickness at a constant 50/50 PB/P3Br$_x$HT weight ratio. Observations for the annealing steps are described in the appendix. Subsequent studies explore the intermolecular interaction and packing of the polymers through morphology, thermal measurements, and UV-vis spectroscopy. The effects of compatibilization in these materials are analyzed electrically in organic field-effect transistors (OFETs) and mechanically by crack onset strain measurements.

4.4.2 Optical Morphology

Clearly discernable segregation between PB and P3Br$_x$HT was found in blended thin films by optical microscopy (**Figure 46**). This is unsurprising considering the highly amorphous and semicrystalline nature of the elastomer and π-conjugated polymer, respectively. For PB/P3Br$_x$HT where x = 0.25, 0.75, a dispersed morphology of light PB phases in a dark P3Br$_x$HT matrix was formed. For x = 1, segregation appeared in a co-continuous arrangement, while the largest domain sizes were observed for x = 0. The poorer miscibility of PB/P3HT suggests that the smaller domains of side chain functionalized samples are a result of weaker intermolecular interactions between π-conjugated polymers. This was supported by differential scanning

calorimetry (DSC) which showed a linear dependence of the melting point (T_m) on the bromide concentration in P3Br$_x$HT (**Figure 47**). As x increased, the decreasing T_m indicated weaker intermolecular interactions and less π-π stacking. Higher interfacial surface area for x = 0.25, 0.75 blends allowed for more radicals to contact PB and crosslink with P3Br$_x$HT to reinforce the composite. No changes in morphology were observed by optical imaging after strengthening the polymer interfaces by UV-activated crosslinking. Overall, side chain functionalization in P3Br$_x$HT successfully led to improved miscibility with PB by controlled bromide concentration. Further compatibilization across crosslinked domains was for influence of mechanical properties.

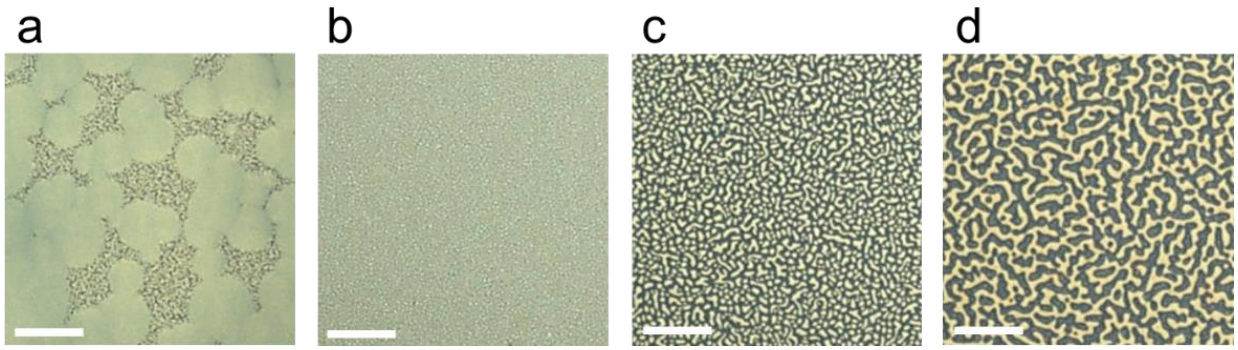

Figure 46: Optical images of PB/P3Br$_x$HT blend thin film morphologies for a) x = 0, b) x = 0.25, c) x = 0.75, and d) x = 1. Scale bar: 10 µm.

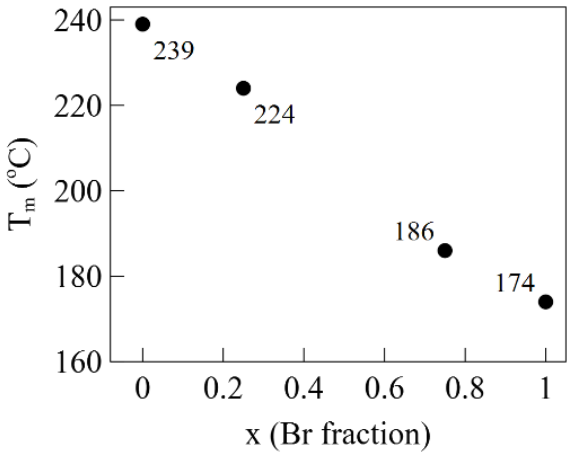

Figure 47: Melting points (T_m) of P3Br$_x$HT polymers determined by DSC.

4.4.3 Crack Onset Strain

The mechanical performance of PB/P3Br$_x$HT blends was measured by crack onset strains and referenced to neat PB and P3HT films (**Table 6**). Thin film samples were transferred onto an elastic polydimethylsiloxane (PDMS) substrate and strain was applied until cracks were observed. A minimum crack length of 20 μm was chosen to define the crack onset strain for clear microscopic crack determination as referenced in literature.[163] Results indicated that uncured PB/P3Br$_x$HT blends with uniform side chains where x = 0, 1 cracked under low strains <10%. We link the lower crack onset strains of x = 0, 1 to larger phase separation, which may also explain the marginal differences in crack onset strain between neat and blended P3HT. On the other hand, uncured samples where x = 0.25, 0.75 were able to withstand substantially larger strains before cracking, up to 39.7%. This finding suggests that crack onset strains are improved by blending PB with the random copolymers of mixed side chains rather than with homopolymers, which is in alignment with morphological observations (**Figure 46**). This further corresponds with previous works where brittleness in polythiophenes was reduced by irregular side chains.[10,102–104,164,165] These results demonstrate that increased crack onset strain was achieved in PB/P3Br$_x$HT through improved compatibility by side chain functionalization as compared to neat P3HT.

Table 6: Crack onset strains of uncured and UV cured PB/P3Br$_x$HT blended thin films and their corresponding substituents. ‡Measurements were limited to 80.4% by the capacity of the strain stage.

Sample	Uncured	UV Cured
PB/P3HT	7.3 ± 2.2 %	9.5 ± 2.6 %
PB/P3Br$_{0.25}$HT	22.9 ± 2.1 %	>80.4 %‡
PB/P3Br$_{0.75}$HT	39.7 ± 10.9 %	>80.4 %‡
PB/P3BrHT	1.8 ± 0.5 %	52.2 ± 5.7 %
PB	>80.4 %‡	>80.4 %‡
P3HT	5.7 ± 1.0 %	7.3 ± 1.4 %

Upon UV curing, all crosslinkable blends where x > 0, had at least a 40% improvement in crack onset strain, with some samples, including neat PB, possessing values above the threshold of the strain stage. Despite a higher bromide concentration for x = 1, its lower crack onset strain compared to x = 0.25, 0.75 is attributed to the larger phase domains. Upon further examination, it is also evident that crosslinking prevented crack propagation, which is most apparent for PB/P3BrHT (Figure 48). Uncured and UV cured x = 0 blends exhibited similar cracking patterns at low strains. A slight crack onset increase for cured PB/P3HT may be due to UV-activated backbone rearrangement.[166] Without UV curing, the x = 1 blend formed long cracks that quickly propagated across the sample at only 2% strain. In contrast, the crosslinked counterpart formed much shorter cracks that did not propagate as readily due to the crosslinked areas surrounding it. It is clear that crosslinking elastomer/π-conjugated polymer blend interfaces improves resistance to strain cracking, which is an important consideration for stretchable electronic materials.

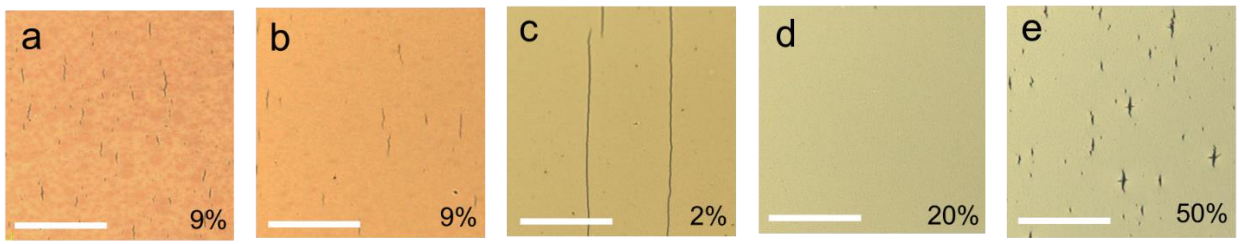

Figure 48: Optical images of PB/P3Br$_x$HT blend films for (a) x = 0 uncured, (b) x = 0 cured, and (c) x = 1 uncured (d-e) x = 1 cured under indicated strains. Scale bar: 100 µm.

4.4.4 Organic Field Effect Transistors (OFETs)

While mechanical improvement in elastomer/π-conjugated polymer blends is important for developing durable, stretchable devices, it is equally as important to consider the electrical properties of such materials. To further investigate the electrical effects of blending, neat P3Br$_x$HT and blended PB/P3Br$_x$HT OFETs were fabricated in a bottom gate top contact architecture (**Figure 49**). Representative transfer and output curves of these devices are provided in the appendix, averaging reliability factors of 68% and 79% for neat and blended films, respectively (**Figure 56**-**Figure 57**).[167] Effects of crosslinking on electrical performance were tested using a strained active layer for OFETs. Neat films consistently had a greater mobility (μ) than the blended counterparts, possibly due to decreased percolation pathways by the addition of PB. In both neat and blended data sets, the highest average μ was observed for x = 0, with a high standard deviation attributed to its larger phase separation discussed previously (**Figure 46**). As x values increased, μ of neat P3Br$_x$HT OFETs declined, while μ of blended PB/P3Br$_x$HT had nearly equal performance for all x>0, showing minor dependence on bromide concentration (**Table 7**). Though mechanical performance of blends is impacted significantly by non-zero concentrations of bromide groups, electrical performance does not show this correlation. Consequently, this minimizes the direct exchange between mechanical and electrical properties for more targeted tuning of material behavior by bromide concentration.

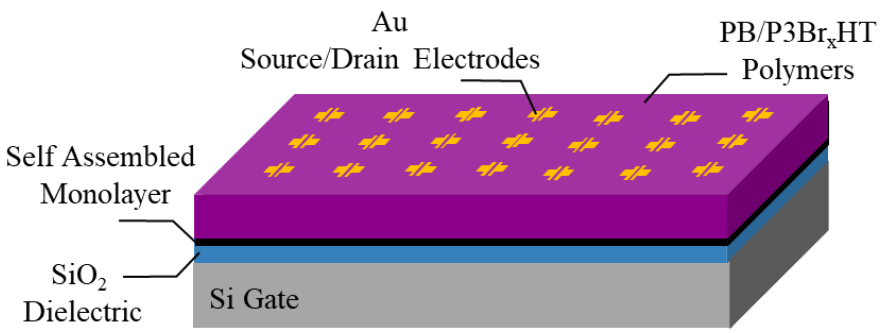

Figure 49: Bottom gate top contact architecture used for the fabrication and testing of neat P3Br$_x$HT and blended PB/P3Br$_x$HT OFETs.

Table 7: OFET mobility (μ), current on-off ratio ($I_{on/off}$), and threshold voltage (V_T) of neat P3Br$_x$HT and blended PB/P3Br$_x$HT films.

	μ (cm^2 / V s)		$I_{on/off}$		V_T (V)	
x	**Neat**	**Blend**	**Neat**	**Blend**	**Neat**	**Blend**
0	(8.8 ± 3.5) x 10^{-4}	(1.5 ± 1.5) x 10^{-4}	10^5	10^3	10	17
0.25	(9.4 ± 3.5) x 10^{-5}	(4.8 ± 1.9) x 10^{-5}	10^3	10^2	5	19
0.75	(7.3 ± 3.4) x 10^{-5}	(4.7 ± 1.1) x 10^{-5}	10^2	10^2	10	4
1	(4.7 ± 1.8) x 10^{-5}	(4.5 ± 0.9) x 10^{-5}	10^3	10^3	4	15

In order to develop proper materials for stretchable devices, it is essential to consider the electrical performance of the composite under strain. The electrical behavior of PB/P3Br$_x$HT blends was tested for OFETs in a construction where the active layer was strained on an elastic PDMS substrate and contacted to the source and drain electrodes in a bottom gate bottom contact architecture, as adapted from literature (**Figure 50**).[168] In accordance with crack onset strains, μ was calculated for blended and cured samples at strains up to 80% (**Figure 51**). Differences in μ at 0% strain compared to top contact OFETs are attributed to modified device architecture and processing methods. It was observed for these data sets that μ decreased with the increase of strain for all samples, independent of x value and sample curing. In this trend, μ was also unaffected by strains above the crack onset strains, which revealed that electrical

performance degraded before the appearance of cracks. Finally, these results show that the crosslinking by brominated side chains brought no negative effect on μ to strained OFETs. As such, the markedly higher crack onset strain of crosslinked materials is preferred over the uncured sample due to its less severe material damage, which is desirable for maintaining the mechanical integrity of a stretchable device.

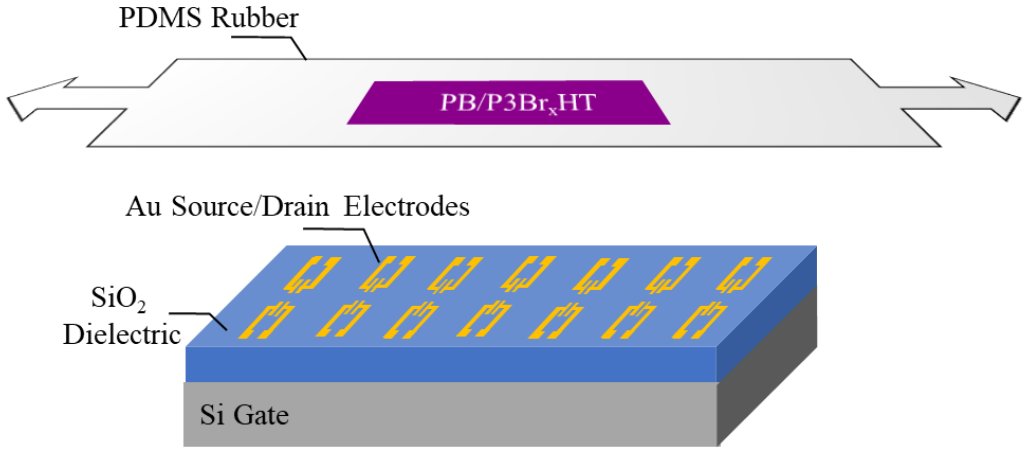

Figure 50: Bottom gate bottom contact OFET architecture used for the fabrication and testing of strained PB/P3Br$_x$HT with and without crosslinking.

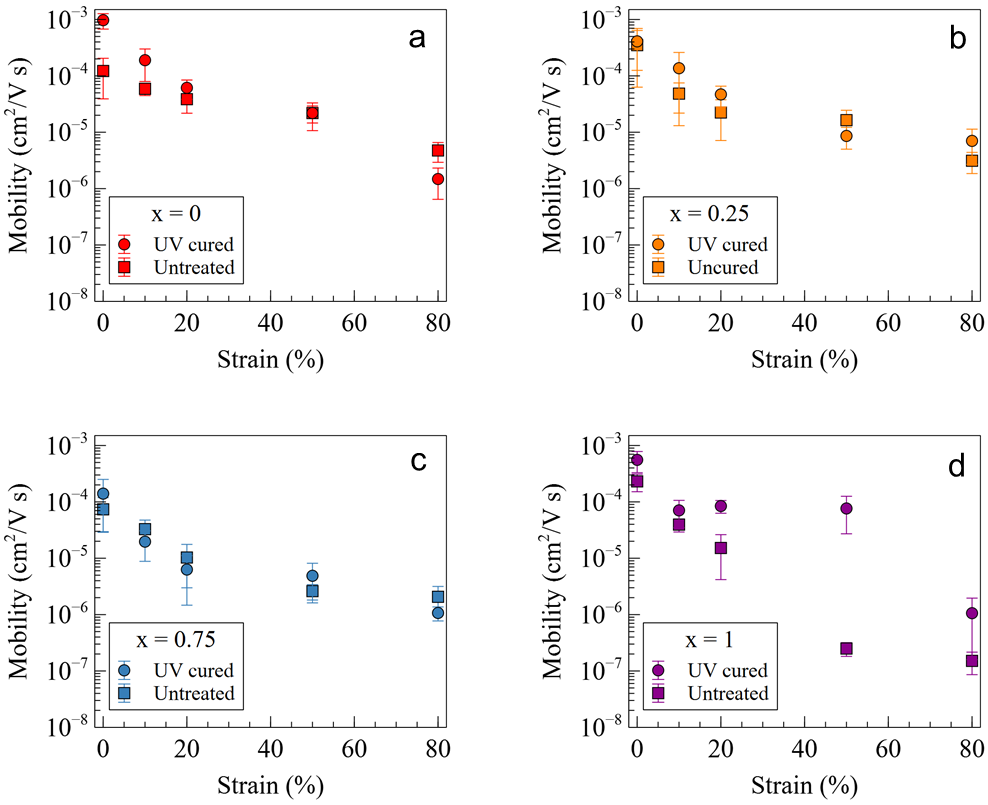

Figure 51: Mobilities of uncured and UV cured PB/P3Br$_x$HT blend OFETs for (a) x = 0, (b) x = 0.25, (c) x = 0.75, (d) x = 1 with a strained active layer. Each point was calculated from an average 9 devices.

4.4.5 UV-vis Spectroscopy

Trends for neat P3Br$_x$HT and blended PB/P3Br$_x$HT were further probed by UV-vis spectroscopy. Analyzed samples include P3Br$_x$HT solutions in chlorobenzene, P3Br$_x$HT neat films and blended PB/P3Br$_x$HT films (**Figure 52**). UV-vis was also used for analysis of aged films, as found in the appendix. Absorption for all P3Br$_x$HT solutions were identical exhibiting a single maximum absorption wavelength (λ_{max}) peak at 456 nm with no aggregation features which denotes equal, high disorder. In comparison, all samples in the film state exhibited higher λ_{max} with three distinct aggregate absorption peaks attributed to P3Br$_x$HT since PB does not absorb in the visible range. These aggregate peaks are a shoulder at ~600 nm corresponding to the 0-0 vibronic transition, the central maximum absorption peak at ~550 nm corresponding to the 0-1

transition, and a shoulder at ~520 nm corresponding to the 0-2 transition.[123,169] Films were analyzed by fitting experimental spectra to its contributing vibronic transitions and amorphous peak absorptions according to the P3HT aggregate model.[123–126]

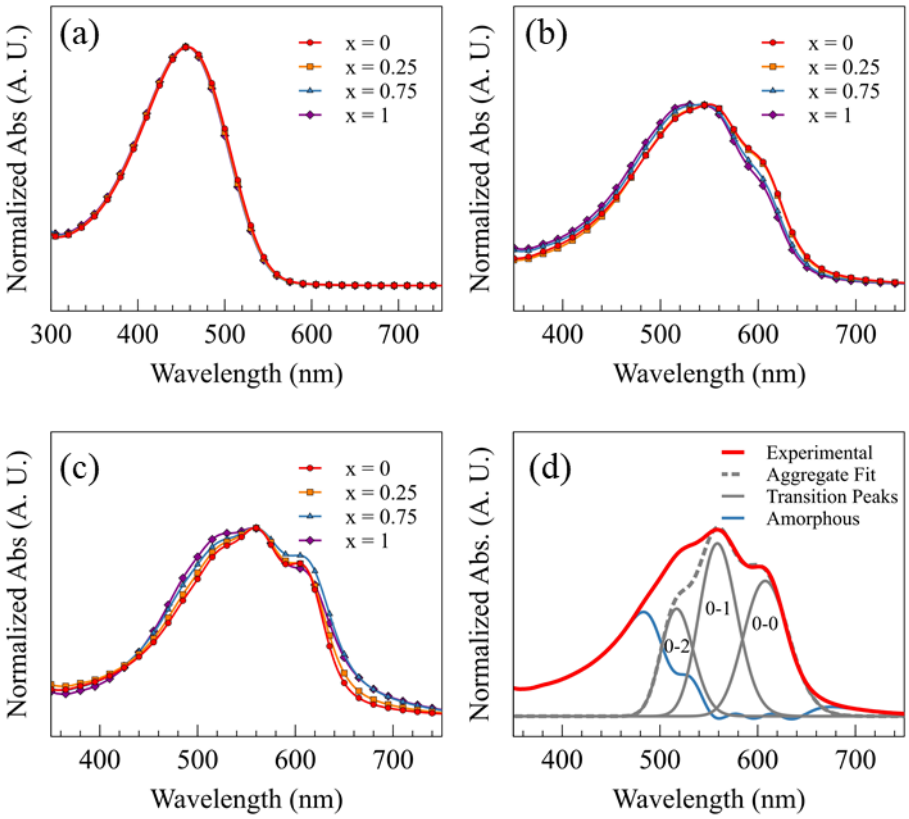

Figure 52: UV-vis absorption of P3Br$_x$HT (a) solutions, (b) films, (c) blended PB/P3Br$_x$HT films, and (d) fit of experimental UV-vis absorption to P3HT aggregate model and its constituent 0-0, 0-1, 0-2 vibronic transitions and amorphous peaks.

Insight into the packing structure of P3Br$_x$HT can be extracted from the ratio of the 0-0 and 0-1 peak transitions ($A_{0\text{-}0}/A_{0\text{-}1}$) and is a key piece for elucidating functionalization effects on backbone arrangement because a larger ratio is tied to improved electrical performance.[7,170,171] All absorbance spectra of films exhibited H-aggregate character with $A_{0\text{-}0}/A_{0\text{-}1}<1$ indicating greater interchain interactions by π-π stacking, whereas J-aggregate character with $A_{0\text{-}0}/A_{0\text{-}1}>1$ would be attributed to dominant intrachain interactions by planar, long-range order (**Table 8**).[123] $A_{0\text{-}0}/A_{0\text{-}1}$ was smaller for P3Br$_x$HT than for PB/P3Br$_x$HT,

indicating that the π-conjugated polymers are less ordered in neat films than in blends and that the addition of PB led to more organized local arrangement of P3Br$_x$HT. This is in agreement with the relative area of the amorphous transition peak, which was greater for neat films than for blended films. With increasing x, P3Br$_x$HT films exhibited a decrease in the $A_{0\text{-}0}/A_{0\text{-}1}$ ratio, while PB/P3Br$_x$HT had only a slight decrease of $A_{0\text{-}0}/A_{0\text{-}1}$. This illustrates that while neat films became more disordered with increasing x and that polymer packing in blended films had considerably weaker correlation to x.

***Table 8**: UV-vis spectroscopy analysis of neat P3Br$_x$HT and blended PB/P3Br$_x$HT films depicting ratio of 0-0 to 0-1 vibronic transition absorption peaks ($A_{0\text{-}0}/A_{0\text{-}1}$), maximum absorption wavelength (λ_{max}), and relative integration of amorphous peak absorption ($A_{amorphous}$).*

	$A_{0\text{-}0}/A_{0\text{-}1}$		λ_{max} (nm)		$A_{amorphous}$ (%)	
x	**Neat**	**Blend**	**Neat**	**Blend**	**Neat**	**Blend**
0	0.69	0.79	550	559	43.8	36.9
0.25	0.69	0.79	549	560	43.5	38.4
0.75	0.62	0.77	545	559	43.8	41.7
1	0.59	0.76	527	558	44.7	42.0

These trends give insight into our OFET μ trends. While blended films may have more order in P3Br$_x$HT, their lower mobility compared to neat films may be due to disrupted charge pathways in the presence of insulating PB, or fewer connections between P3Br$_x$HT crystallites.[37] These trends however, are contrary to the amorphous peak areas, which remained similar for neat films but increased for the blended films as x increased. This indicates that changes in the charge mobility are not due to total contribution of the amorphous region, but rather the type of aggregation in the ordered regions and their connectivity. Together, this data shows that adjusting the bromide concentration in PB/P3Br$_x$HT blends had a lesser effect on electrical output than on the mechanical performance, and that the composite's resistance to strain is primarily driven by its micron scale morphology rather than individual chain order.

To explore the mechanism of electrical failure in strained OFETs, samples were analyzed by UV-vis under strain. Uncured and UV cured PB/P3Br$_{0.25}$HT were examined at 0, 20, 50, and 80% strains and no trends were found in the absorbance spectra (**Figure 53**). This denotes that the P3Br$_{0.25}$HT crystallites remained intact even beyond the crack onset strain and that mechanical failure was indeed likely occurring at PB/P3Br$_x$HT interfaces. The cause of μ degradation in strained OFETs is then attributed not to the breaking of π-π stacks within crystallites, but to the loss of interconnecting tie chains between semiconducting crystallites as their distance increased under strain.[31,37,38,172] UV-vis of strained films further supports that P3Br$_x$HT backbone packing is associated predominantly with electrical properties and that compatibility with PB is the chief influence for mechanical property trends.

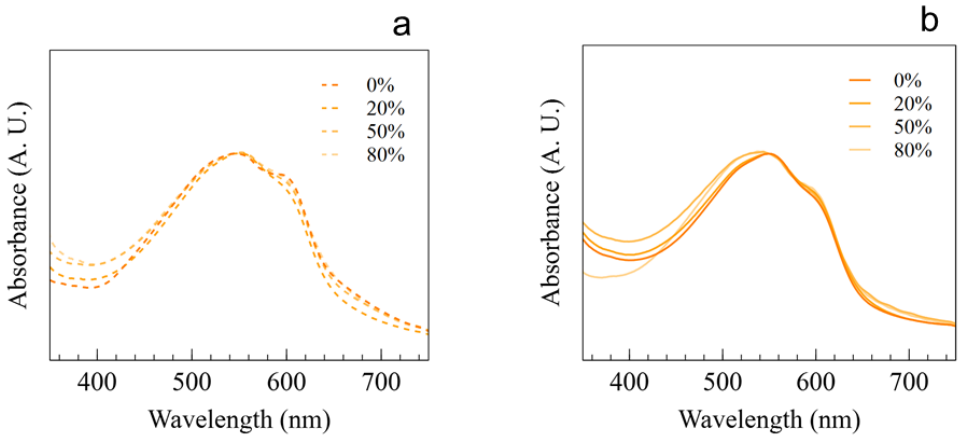

Figure 53: UV-vis of (a) uncured and (b) cured PB/P3Br$_{0.25}$HT on elastic substrate under indicated strains.

4.5 Concluding Remarks

This work presents the first studies of a blended elastomer/π-conjugated polymer system whose mechanical performance is drastically improved by compatibilization which is achieved through side chain functionalization. An alkylbromide side chain on the π-conjugated polymer was found to be an effective group for altering intermolecular interactions between polymers and for crosslinking with an unsaturated

elastomer. While thiol-functionalized P3HT showed evidence of elastomer bonding at low concentrations, high thiol content was prone to self-crosslinking, and thus bromide functionalization was the focus of the study. A set of poly[(3-(6-bromohexyl)thiophene)-*ran*-(3-hexylthiophene)] ($P3Br_xHT$, x = 0-1) with successive increase in bromide concentration were synthesized to study its effects on electrical and mechanical performance in neat $P3Br_xHT$ and blended PB/$P3Br_xHT$ films. Viable crosslinking was demonstrated by gel fraction experiments with potential to tailor crosslinking for specific device properties. Morphological analysis demonstrated improved compatibility through smaller domain sizes for blends with mixed side chains (x = 0.25, 0.75) which was reflected in greater crack onset strains up to 40%, as opposed to <10% for homogeneous side chains (x = 0, 1). Furthermore, crosslinking with PB led to at least an additional 40% increase in the crack onset strain by bonding the elastomer and PB at their domain interfaces. Correlated OFET and UV-vis spectroscopy data designated the mechanical property effects primarily to compatibility between polymers which was influenced by π-conjugated polymer packing. For strained OFETs, both blended and crosslinked materials performed similarly under strain, signifying that crosslinking did not lead to a tradeoff between electrical and mechanical performance. This work has demonstrated that increased compatibility through functionalization is a successful means to significantly reduce the brittleness of a polymeric elastomer/π-conjugated polymer composite.

Future work of the system entails a few possible routes. Characterization of crosslinked films can be supplemented by elemental analysis to verify bromide loss upon UV curing. This would provide information about the extent of activation from $P3Br_xHT$ and can be obtained by surface analysis with X-ray photoelectron spectroscopy, or alternatively with energy dispersive x-ray spectrometry. Additional mechanical testing can also provide insight into the durability of the composite. Fatigue with repeated strain measurements can be applied for crack onset strain and stretched OFET mobility. Also, full stress-strain measurements would provide a fuller understanding of the material, which have previously been reported for thin films of π-conjugated polymers.[10,173] Attempts to apply this approach to heterogeneous

composite films proved more challenging and further optimization may lead to adequate methodology for stress-strain measurement of elastomer/π-conjugated polymer blends. Another direction for future work would entail a more detailed understanding of P3Br$_x$HT packing by exploring nanoscale order by X-ray diffraction techniques. This may be accompanied by higher resolution morphology by atomic force microscopy as well as computational simulations probing polymer conformation and intermolecular interactions. Overall, crosslinking between an unsaturated elastomer and bromide-functionalized π-conjugated polymer may be applied to a broad range of rubber and semiconducting materials in order to tune properties to their target stretchable electronic applications.

Appendix

Annealing Effects

It was observed that the annealing step in film processing led to similar packing for all neat P3Br$_x$HT and blended PB/P3Br$_x$HT films, a step used to enhance electrical performance.[174,175] Films with higher x values showed an increasing red tint which was lost after annealing to produce a uniform purple color (**Figure 54**). UV-vis analysis of PB/P3Br$_x$HT films supports this change in absorption with a lower maximum absorption wavelength (λ_{max}) down to 537 nm for more red color films compared to 561 nm for PB/P3HT (**Figure 55**). This lower λ_{max} is associated with a shorter extent of conjugation and greater disorder.[176,177] After annealing, all PB/P3Br$_x$HT showed a consistent λ_{max} of 560 nm post annealing indicating that the annealing step affected all polymer blend samples similarly.

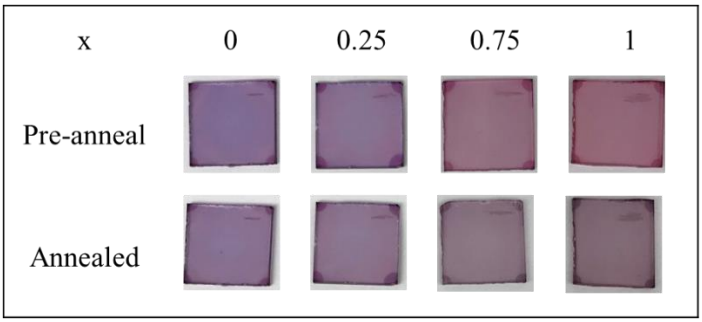

Figure 54: Photographs of PB/P3Br$_x$HT before and after annealing.

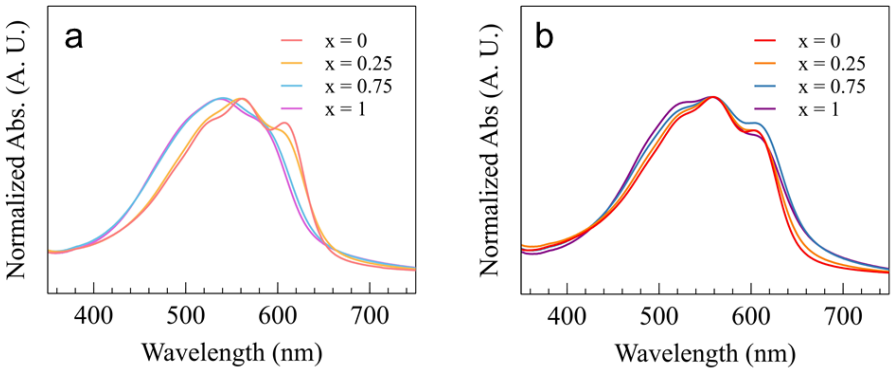

Figure 55: UV-vis of PB/P3Br$_x$HT blends (a) before and (b) after annealing.

Representative OFET Curves

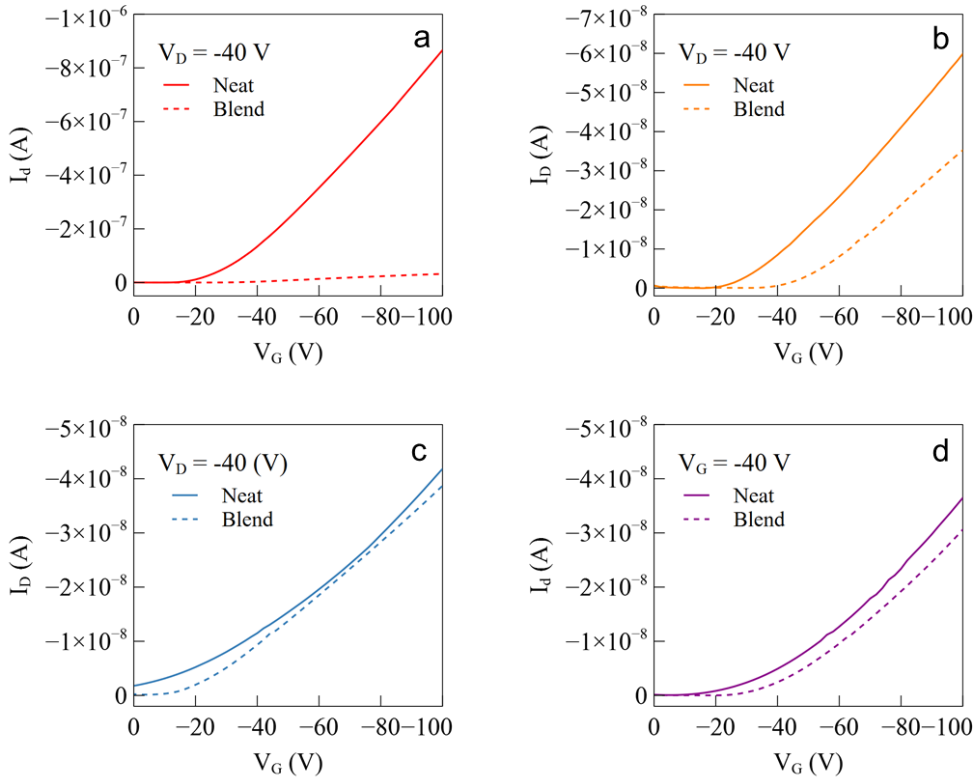

Figure 56: Representative transer curves of neat P3Br$_x$HT and blended PB/P3Br$_x$HT OFETs where (a) x = 0, (b) x = 0.25, (c) x = 0.75, (d) x = 1.

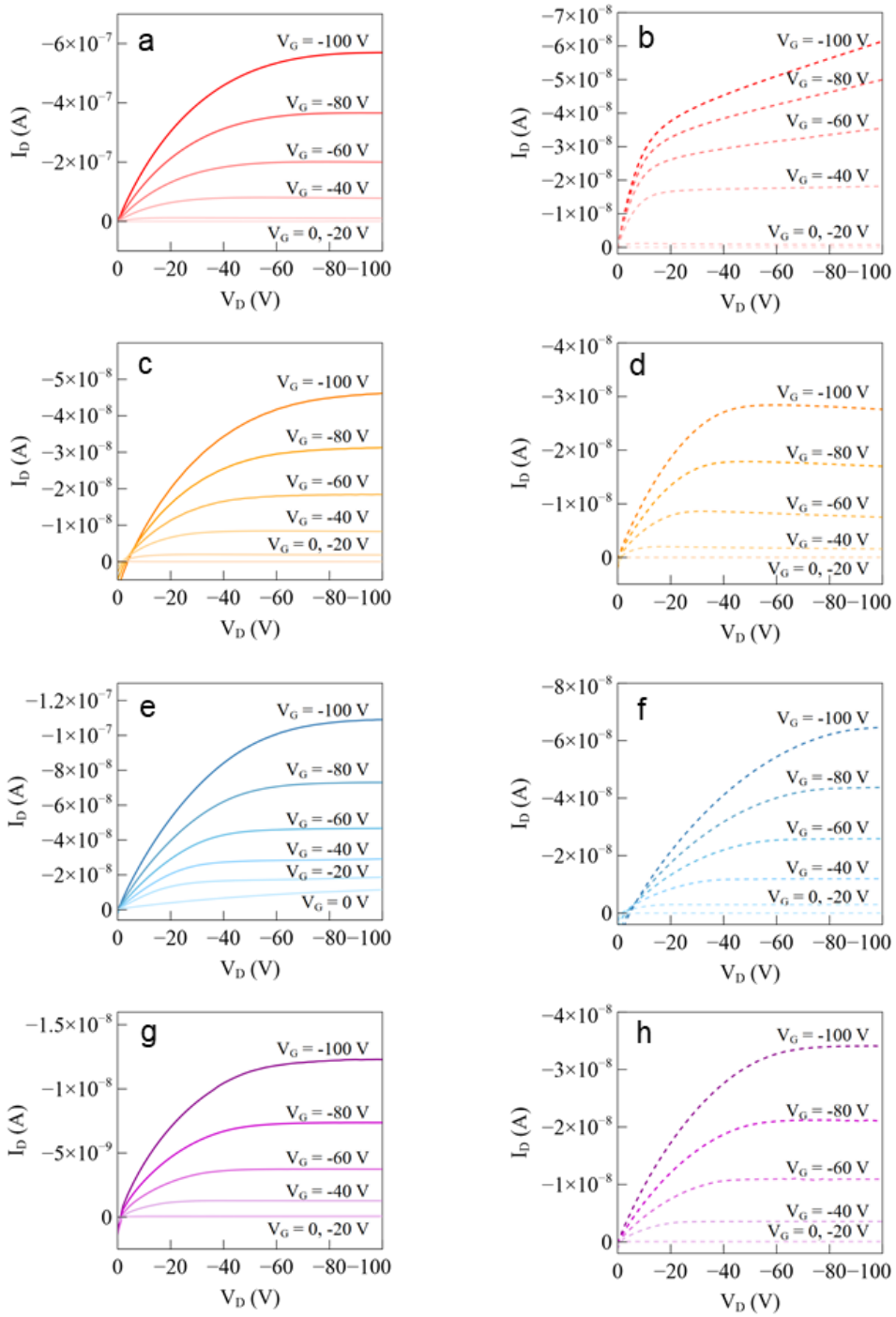

Figure 57: *Representative output curves of neat P3Br$_x$HT (solid) and blended PB/P3Br$_x$HT (dashed) OFETs where (a-b) x = 0, (c-d) x = 0.25, (e-f) x = 0.75 and (g-h) x = 1.*

Aging Studies

Some exploratory work was performed to test the aging behavior of PB/P3Br$_x$HT blends with OFET and UV-vis properties. Films were aged up to 6 weeks under continuous exposure to ambient laboratory light to monitor stability against photooxidation. Aged OFETs were tested for 2 blends of PB/P3Br$_x$HT where x = 0, 1 (**Figure 58**). PB/P3HT degraded losing 99.8% of its original mobility after 6 weeks. In contrast, the mobility of PB/P3BrHT remained relatively constant. Both films experienced an increase in mobility, the origins of which require further investigation. PB/P3BrHT may be showing greater environmental resistance than PB/P3HT due to the functionalized side chain acting as an alternative oxidation site to the thiophene backbone.

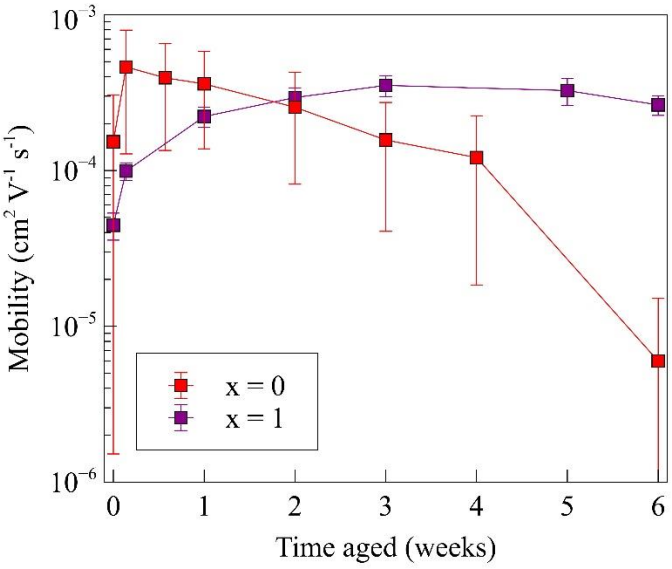

Figure 58: OFET mobility of PB/P3Br$_x$HT blends for x = 0, 1 aged in air and light up to 6 weeks.

Aged films of PB/P3Br$_x$HT were also analyzed by UV-vis with and without UV-activated crosslinking (**Figure 59**). Changes in the spectra over time were quantified by the difference in the maximum absorption wavelength, λ_{max} (**Table 9**). All samples experienced a blue-shift, indicating conjugation loss, with no

distinction between UV cured and uncured films. The extent of degradation was dependent on the bromide concentration, which was best maintained with an increasing x value. The greatest loss was found for x = 0 with a ~100 nm λ_{max} blue-shift and peak absorption loss of 95%, whereas the PB/P3BrHT demonstrated an absorption loss as low as 10% with a 4 nm blueshift. The photobleaching of films was also visible macroscopically, which is most evident for PB/P3HT and becomes less distinct as x increases (Figure 60). These results indicate that the proportion of bromide monomer has a greater effect on aging than UV curing in a film's resistance to environmental degradation.

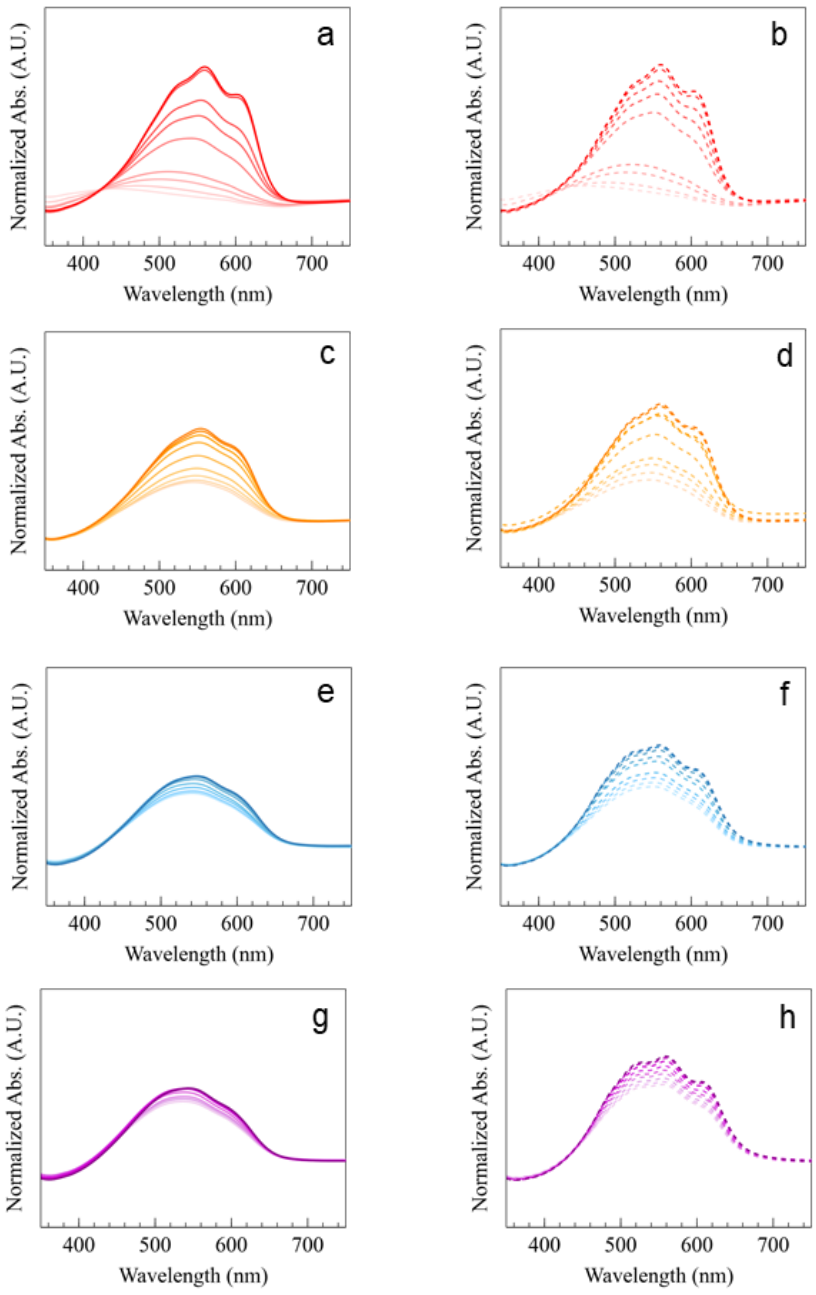

Figure 59: Normalized UV-vis absorption of UV cured (solid lines) and untreated (dashed lines) PB/P3Br$_x$HT films from initial spectra (darkest) to 6 weeks of aging (lightest) where (a-b) x = 0, (c-d) x = 0.25, (e-f) x = 0.75, (g-h) x = 1. Spectra collected at 0, 1, 4 days and 1, 2, 3, 4, 5, 6 weeks of aging.

Table 9: Change in maximum peak absorbance wavelength (Δ λ_{max}) of uncured and UV cured PB/P3Br$_x$HT films aged for 6 weeks.

	$\Delta\lambda_{max}$ (nm)	
x	**UV cured**	**Untreated**
0	-116	-98
0.25	-11	-15
0.75	-5	-8
1	-8	-4

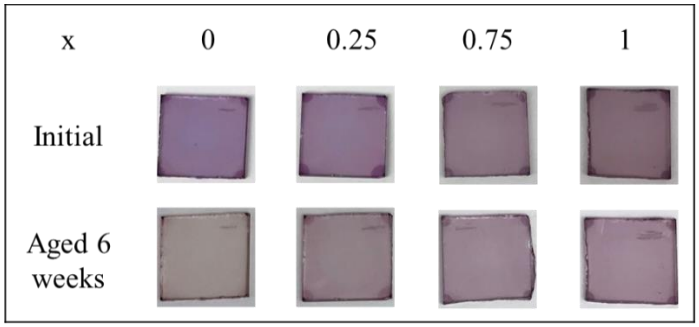

Figure 60: Photographs of aged PB/P3Br$_x$HT films.

References

1. Qian, Y. *et al.* Stretchable Organic Semiconductor Devices. *Adv. Mater.* **28**, 9243–9265 (2016).
2. Shaw, J. M. & Seidler, P. F. Organic Electronics: Introduction. *IBM J. Res. Dev.* **45**, 3–9 (2001).
3. Abdulrazzaq, O. A., Saini, V., Bourdo, S., Dervishi, E. & Biris, A. S. Organic Solar Cells: A Review of Materials, Limitations, and Possibilities for Improvement. *Part. Sci. Technol.* **31**, 427–442 (2013).
4. Himmelberger, S. *et al.* Role of Side-Chain Branching on Thin-Film Structure and Electronic Properties of Polythiophenes. *Adv. Funct. Mater.* **25**, 2616–2624 (2015).
5. Zhang, Z.-G. & Li, Y. Side-Chain Engineering of High-Efficiency Conjugated Polymer Photovoltaic Materials. *Sci. China Chem.* **58**, 192–209 (2015).
6. Shi, L., Guo, Y., Hu, W. & Liu, Y. Design and Effective Synthesis Methods for High-Performance Polymer Semiconductors in Organic Field-Effect Transistors. *Mater. Chem. Front.* **1**, 2423–2456 (2017).
7. Mazzio, K. A., Rice, A. H., Durban, M. M. & Luscombe, C. K. Effect of Regioregularity on Charge Transport and Structural and Excitonic Coherence in Poly(3-hexylthiophene) Nanowires. *J. Phys. Chem. C* **119**, 14911–14918 (2015).
8. Kim, Y. *et al.* A Strong Regioregularity Effect in Self-Organizing Conjugated Polymer Films and High-Efficiency Polythiophene:Fullerene Solar Cells. *Nat. Mater.* **5**, 197–203 (2006).
9. Aiyar, A. R., Hong, J.-I. & Reichmanis, E. Regioregularity and Intrachain Ordering: Impact on the Nanostructure and Charge Transport in Two-Dimensional Assemblies of Poly(3-hexylthiophene). *Chem. Mater.* **24**, 2845–2853 (2012).
10. Kim, J. S. *et al.* Tuning Mechanical and Optoelectrical Properties of Poly(3-hexylthiophene) through Systematic Regioregularity Control. *Macromolecules* **48**, 4339–4346 (2015).
11. Kline, R. J., McGehee, M. D., Kadnikova, E. N., Liu, J. & Fréchet, J. M. J. Controlling the Field-Effect Mobility of Regioregular Polythiophene by Changing the Molecular Weight. *Adv. Mater.* **15**, 1519–1522
12. Kline, R. J. *et al.* Dependence of Regioregular Poly(3-hexylthiophene) Film Morphology and Field-Effect Mobility on Molecular Weight. *Macromolecules* **38**, 3312–3319 (2005).
13. Zhang, R. *et al.* Nanostructure Dependence of Field-Effect Mobility in Regioregular Poly(3-hexylthiophene) Thin Film Field Effect Transistors. *J. Am. Chem. Soc.* **128**, 3480–3481 (2006).
14. Zen, A. *et al.* Effect of Molecular Weight and Annealing of Poly(3-hexylthiophene)s on the Performance of Organic Field-Effect Transistors. *Adv. Funct. Mater.* **14**, 757–764 (2004).
15. Dixon, A. G. *et al.* Molecular Weight Dependence of Carrier Mobility and Recombination Rate in Neat P3HT Films. *J. Polym. Sci. Part B Polym. Phys.* **56**, 31–35 (2018).
16. Ballantyne, A. M. *et al.* The Effect of Poly(3-hexylthiophene) Molecular Weight on Charge Transport and the Performance of Polymer:Fullerene Solar Cells. *Adv. Funct. Mater.* **18**, 2373–2380 (2008).
17. Bronstein, H. A. & Luscombe, C. K. Externally Initiated Regioregular P3HT With Controlled Molecular Weight and Narrow Polydispersity. *J. Am. Chem. Soc.* **131**, 12894–12895 (2009).
18. Quagliotto, P. & Fin, A. Advances in Synthetic Methods for the Preparation of Poly(3- hexylthiophene) (P3HT). *Lett. Org. Chem.* **15**, 991–1006 (2018).
19. Junior, M. L. P., Júnior, R. T. de S., Silva, G. M. e & Júnior, L. A. R. Stationary Polaron Properties in Organic Crystalline Semiconductors. *Phys. Chem. Chem. Phys.* **21**, 2727–2733 (2019).
20. Lu, N., Li, L., Geng, D. & Liu, M. A Review for Polaron Dependent Charge Transport in Organic Semiconductor. *Org. Electron.* **61**, 223–234 (2018).
21. Brown, P. J., Sirringhaus, H., Harrison, M., Shkunov, M. & Friend, R. H. Optical Spectroscopy of Field-Induced Charge in Self-Organized High Mobility Poly(3-hexylthiophene). *Phys. Rev. B* **63**, 125204 (2001).

22. Chang, J.-F., Sirringhaus, H., Giles, M., Heeney, M. & McCulloch, I. Relative Importance of Polaron Activation and Disorder on Charge Transport in High-Mobility Conjugated Polymer Field-Effect Transistors. *Phys. Rev. B* **76**, 205204 (2007).
23. Tadaki, D. *et al.* Molecular Doping of Regioregular Poly(3-hexylthiophene) Layers by 2,3,5,6-tetrafluoro-7,7,8,8-tetracyanoquinodimethane Investigated by Infrared Spectroscopy and Electrical Measurements. *Jpn. J. Appl. Phys.* **54**, 091602 (2015).
24. Nightingale, J., Wade, J., Moia, D., Nelson, J. & Kim, J.-S. Impact of Molecular Order on Polaron Formation in Conjugated Polymers. *J. Phys. Chem. C* **122**, 29129–29140 (2018).
25. Facchetti, A. π-Conjugated Polymers for Organic Electronics and Photovoltaic Cell Applications. *Chem. Mater.* **23**, 733–758 (2011).
26. *Organic Optoelectronic Materials*. (Springer International Publishing, 2015).
27. Kar, P. *Doping in Conjugated Polymers*. (Wiley, 2013).
28. Chew, A. R. *et al.* Unraveling the Effect of Conformational and Electronic Disorder in the Charge Transport Processes of Semiconducting Polymers. *Adv. Funct. Mater.* **28**, 1804142 (2018).
29. Ghosh, R. *et al.* Spectral Signatures and Spatial Coherence of Bound and Unbound Polarons in P3HT Films: Theory Versus Experiment. *J. Phys. Chem. C* **122**, 18048–18060 (2018).
30. Zen, A. *et al.* Effect of Molecular Weight on the Structure and Crystallinity of Poly(3-hexylthiophene). *Macromolecules* **39**, 2162–2171 (2006).
31. Koch, F. P. V. *et al.* The Impact of Molecular Weight on Microstructure and Charge Transport in Semicrystalline Polymer Semiconductors–Poly(3-hexylthiophene), a Model Study. *Prog. Polym. Sci.* **38**, 1978–1989 (2013).
32. Assadi, A., Svensson, C., Willander, M. & Inganäs, O. Field-Effect Mobility of Poly(3-hexylthiophene). *Appl. Phys. Lett.* **53**, 195–197 (1988).
33. Liu, C.-H. *et al.* Effects of Amorphous Poly(3-hexylthiophene) on Active-Layer Structure and Solar Cells Performance. *J. Polym. Sci. Part B Polym. Phys.* **54**, 975–985 (2016).
34. Österbacka, R., An, C. P., Jiang, X. M. & Vardeny, Z. V. Two-Dimensional Electronic Excitations in Self-Assembled Conjugated Polymer Nanocrystals. *Science* **287**, 839–842 (2000).
35. McCulloch, B. *et al.* Polymer Chain Shape of Poly(3-alkylthiophenes) in Solution Using Small-Angle Neutron Scattering. *Macromolecules* **46**, 1899–1907 (2013).
36. Duong, D. T. *et al.* Mechanism of Crystallization and Implications for Charge Transport in Poly(3-ethylhexylthiophene) Thin Films. *Adv. Funct. Mater.* **24**, 4515–4521 (2014).
37. Noriega, R. *et al.* A General Relationship Between Disorder, Aggregation and Charge Transport in Conjugated Polymers. *Nat. Mater.* **12**, 1038–1044 (2013).
38. Himmelberger, S., Vandewal, K., Fei, Z., Heeney, M. & Salleo, A. Role of Molecular Weight Distribution on Charge Transport in Semiconducting Polymers. *Macromolecules* **47**, 7151–7157 (2014).
39. Itoh, E., Terashima, K., Nagai, H. & Miyairi, K. Evaluation of Poly(3-hexylthiophene)/Polymeric Insulator Interface by Charge Modulation Spectroscopy Technique. *Thin Solid Films* **518**, 810–813 (2009).
40. Sirringhaus, H. *et al.* Two-Dimensional Charge Transport in Self-Organized, High-Mobility Conjugated Polymers. *Nature* **401**, 685 (1999).
41. Jiang, X. *et al.* Spectroscopic Studies of Photoexcitations in Regioregular and Regiorandom Polythiophene Films. *Adv Funct Mater* 11 (2002).
42. Hamidi-Sakr, A. *et al.* A Versatile Method to Fabricate Highly In-Plane Aligned Conducting Polymer Films with Anisotropic Charge Transport and Thermoelectric Properties: The Key Role of Alkyl Side Chain Layers on the Doping Mechanism. *Adv. Funct. Mater.* **27**, 1700173 (2017).
43. Orlandi, G. & Siebrand, W. Theory of Vibronic Intensity Borrowing. Comparison of Herzberg-Teller and Born-Oppenheimer Coupling. *J. Chem. Phys.* **58**, 4513–4523 (1973).
44. Scholes, D. T. *et al.* The Effects of Crystallinity on Charge Transport and the Structure of Sequentially Processed F4TCNQ-Doped Conjugated Polymer Films. *Adv. Funct. Mater.* **27**, 1702654 (2017).

45. Chew, A. R., Ghosh, R., Shang, Z., Spano, F. C. & Salleo, A. Sequential Doping Reveals the Importance of Amorphous Chain Rigidity in Charge Transport of Semi-Crystalline Polymers. *J. Phys. Chem. Lett.* **8**, 4974–4980 (2017).
46. Pingel, P. & Neher, D. Comprehensive Picture of P-Type Doping of P3HT with the Molecular Acceptor F4 TCNQ. *Phys. Rev. B* **87**, 115209 (2013).
47. Koch, F. P. V., Heeney, M. & Smith, P. Thermal and Structural Characteristics of Oligo(3-hexylthiophene)s (3HT)n, n = 4–36. *J. Am. Chem. Soc.* **135**, 13699–13709 (2013).
48. Jacobs, I. E. *et al.* Comparison of Solution-Mixed and Sequentially Processed P3HT:F4TCNQ Films: Effect of Doping-Induced Aggregation on Film Morphology. *J Mater Chem C* **4**, 3454–3466 (2016).
49. Obrzut, J. & Page, K. A. Electrical Conductivity and Relaxation in Poly(3-hexylthiophene). *Phys. Rev. B* **80**, 195211 (2009).
50. Paternó, G., Cacialli, F. & García-Sakai, V. Structural and Dynamical Characterization of P3HT/PCBM Blends. *Chem. Phys.* **427**, 142–146 (2013).
51. Etampawala, T. *et al.* Monitoring the Dynamics of Miscible P3HT:PCBM blends: A Quasi Elastic Neutron Scattering Study of Organic Photovoltaic Active Layers. *Polymer* **61**, 155–162 (2015).
52. Guilbert, A. A. Y., Zbiri, M., Jenart, M. V. C., Nielsen, C. B. & Nelson, J. New Insights into the Molecular Dynamics of P3HT:PCBM Bulk Heterojunction: A Time-of-Flight Quasi-Elastic Neutron Scattering Study. *J. Phys. Chem. Lett.* **7**, 2252–2257 (2016).
53. Djurado, D. *et al.* Counter-Ions Dynamics in Highly Plastic and Conducting Compounds of Poly(aniline). A Quasi-Elastic Neutron Scattering Study. *Phys. Chem. Chem. Phys.* **7**, 1235–1240 (2005).
54. Djurado, D. *et al.* Disorder Effects in "Plastic" and Highly Conducting Compounds of Poly(aniline). *Macromol. Symp.* **241**, 28–33 (2006).
55. Sniechowski, M. & djurado, luzny. Structure and Dynamics of Plast-Doped Conducting Polyaniline Compounds. *Fibres Text. East. Eur.* **13**, 96–99 (2005).
56. Guilbert, A. A. Y. *et al.* Temperature-Dependent Dynamics of Polyalkylthiophene Conjugated Polymers: A Combined Neutron Scattering and Simulation Study. *Chem. Mater.* **27**, 7652–7661 (2015).
57. Guilbert, A. A. Y., Zbiri, M., Dunbar, A. D. F. & Nelson, J. Quantitative Analysis of the Molecular Dynamics of P3HT:PCBM Bulk Heterojunction. *J. Phys. Chem. B* **121**, 9073–9080 (2017).
58. Bhatta, R. S., Yimer, Y. Y., Perry, D. S. & Tsige, M. Improved Force Field for Molecular Modeling of Poly(3-hexylthiophene). *J. Phys. Chem. B* **117**, 10035–10045 (2013).
59. Schwarz, K. N., Kee, T. W. & Huang, D. M. Coarse-Grained Simulations of the Solution-Phase Self-Assembly of Poly(3-hexylthiophene) Nanostructures. *Nanoscale* **5**, 2017–2027 (2013).
60. Moreno, M., Casalegno, M., Raos, G., Meille, S. V. & Po, R. Molecular Modeling of Crystalline Alkylthiophene Oligomers and Polymers. *J. Phys. Chem. B* **114**, 1591–1602 (2010).
61. M. Wolf, C. *et al.* Assessment of Molecular Dynamics Simulations for Amorphous Poly(3-hexylthiophene) Using Neutron and X-ray Scattering Experiments. *Soft Matter* **15**, 5067–5083 (2019).
62. Shen, X., Hu, W. & Russell, T. P. Measuring the Degree of Crystallinity in Semicrystalline Regioregular Poly(3-hexylthiophene). *Macromolecules* **49**, 4501–4509 (2016).
63. Shen, X., Duzhko, V. V. & Russell, T. P. A Study on the Correlation Between Structure and Hole Transport in Semi-Crystalline Regioregular P3HT. *Adv. Energy Mater.* **3**, 263–270 (2013).
64. Tashiro, K. *et al.* Structure and Thermochromic Solid-State Phase Transition of Poly(3-alkylthiophene). *J. Polym. Sci. Part B Polym. Phys.* **29**, 1223–1233 (1991).
65. Tashiro, K. *et al.* Structural Changes in the Thermochromic Solid-State Phase Transition of Poly(3-alkylthiophene. *Synth. Met.* **41**, 571–574 (1991).
66. Trung, T. Q. & Lee, N.-E. Recent Progress on Stretchable Electronic Devices with Intrinsically Stretchable Components. *Adv. Mater.* **29**, 1603167 (2016).
67. Lipomi, D. J. & Bao, Z. Stretchable, Elastic Materials and Devices for Solar Energy Conversion. *Energy Environ. Sci.* **4**, 3314–3328 (2011).

68. Yan, C. & Lee, P. S. Stretchable Energy Storage and Conversion Devices. *Small* **10**, 3443–3460 (2014).
69. Vosgueritchian, M., Tok, J. B.-H. & Bao, Z. Stretchable LEDs: Light-Emitting Electronic Skin. *Nat. Photonics* **7**, 769–771 (2013).
70. Liu, Y., Pharr, M. & Salvatore, G. A. Lab-on-Skin: A Review of Flexible and Stretchable Electronics for Wearable Health Monitoring. *ACS Nano* **11**, 9614–9635 (2017).
71. Zeng, W. *et al.* Fiber-Based Wearable Electronics: A Review of Materials, Fabrication, Devices, and Applications. *Adv. Mater.* **26**, 5310–5336 (2014).
72. Gong, S. & Cheng, W. Toward Soft Skin-Like Wearable and Implantable Energy Devices. *Adv. Energy Mater.* **7**, 1700648 (2017).
73. Hammock, M. L., Chortos, A., Tee, B. C.-K., Tok, J. B.-H. & Bao, Z. 25th Anniversary Article: The Evolution of Electronic Skin (E-Skin): A Brief History, Design Considerations, and Recent Progress. *Adv. Mater.* **25**, 5997–6038 (2013).
74. Yang, J., Zhao, Z., Wang, S., Guo, Y. & Liu, Y. Insight into High-Performance Conjugated Polymers for Organic Field-Effect Transistors. *Chem* **4**, 2748–2785 (2018).
75. Shan, B. & Miao, Q. Molecular Design of n-Type Organic Semiconductors for High-Performance Thin Film Transistors. *Tetrahedron Lett.* **58**, 1903–1911 (2017).
76. Gao, X. & Zhao, Z. High Mobility Organic Semiconductors for Field-Effect Transistors. *Sci. China Chem.* **58**, 947–968 (2015).
77. Dong, H., Fu, X., Liu, J., Wang, Z. & Hu, W. 25th Anniversary Article: Key Points for High-Mobility Organic Field-Effect Transistors. *Adv. Mater.* **25**, 6158–6183 (2013).
78. Po, R. *et al.* From Lab to Fab: How Must the Polymer Solar Cell Materials Design Change? – An Industrial Perspective. *Energy Environ. Sci.* **7**, 925–943 (2014).
79. Guo, X. *et al.* Current Status and Opportunities of Organic Thin-Film Transistor Technologies. *IEEE Trans. Electron Devices* **64**, 1906–1921 (2017).
80. Yu, D., Yang, Y.-Q., Chen, Z., Tao, Y. & Liu, Y.-F. Recent Progress on Thin-Film Encapsulation Technologies for Organic Electronic Devices. *Opt. Commun.* **362**, 43–49 (2016).
81. Choi, D. *et al.* Elastomer-Polymer Semiconductor Blends for High-Performance Stretchable Charge Transport Networks. *Chem. Mater.* **28**, 1196–1204 (2016).
82. Li, P., Sun, K. & Ouyang, J. Stretchable and Conductive Polymer Films Prepared by Solution Blending. *ACS Appl. Mater. Interfaces* **7**, 18415–18423 (2015).
83. Printz, A. D. & Lipomi, D. J. Competition Between Deformability and Charge Transport in Semiconducting Polymers for Flexible and Stretchable Electronics. *Appl. Phys. Rev.* **3**, 021302 (2016).
84. Shin, M. *et al.* Polythiophene Nanofibril Bundles Surface-Embedded in Elastomer: A Route to a Highly Stretchable Active Channel Layer. *Adv. Mater.* **27**, 1255–1261 (2015).
85. Onorato, J., Pakhnyuk, V. & Luscombe, C. K. Structure and Design of Polymers for Durable, Stretchable Organic Electronics. *Polym. J.* **49**, 41–60 (2017).
86. Gazotti, W. A., Faez, R. & De Paoli, M.-A. Thermal and Mechanical Behaviour of a Conductive Elastomeric Blend Based on a Soluble Polyaniline Derivative. *Eur. Polym. J.* **35**, 35–40 (1999).
87. Samui, A. B., Manoj, N. R., Raut, R. & Patankar, A. S. Thermoplastic Blend of Polyaniline with Polyvinyl Chloride-Nitrile Rubber. *J. Appl. Polym. Sci.* **101**, 1217–1222 (2006).
88. Hansen, T. S., West, K., Hassager, O. & Larsen, N. B. Highly Stretchable and Conductive Polymer Material Made from Poly(3,4-ethylenedioxythiophene) and Polyurethane Elastomers. *Adv. Funct. Mater.* **17**, 3069–3073 (2007).
89. Kausar, A. Design, Synthesis and Physical Properties of Poly(styrene-butadiene-styrene)/Poly(thiourea-azo-sulfone) blends. *Bull. Mater. Sci.* **37**, 917–923 (2014).
90. Vallim, M. R., Felisberti, M. I. & De Paoli, M. A. Blends of Polyaniline with Nitrilic Rubber. *J. Appl. Polym. Sci.* **75**, 677–684 (2000).

91. Barra, G. M. O., Jacques, L. B., Orefice, R. L. & Carneiro, J. R. G. Processing, Characterization and Properties of Conducting Polyaniline-Sulfonated SEBS Block Copolymers. *Eur. Polym. J.* **40**, 2017–2023 (2004).
92. Barra, G. M. O. *et al.* Thermoplastic Elastomer/Polyaniline Blends: Evaluation of Mechanical and Electromechanical Properties. *Polym. Test.* **27**, 886–892 (2008).
93. Soares, B. G., Amorim, G. S., Oliveira, M. G. & Pereira da Silva, J. e. Conducting Elastomer Blends Based on Nitrile Rubber and Pani.DBSA. *Macromol. Symp.* **233**, 95–101 (2006).
94. Taroni, P. J. *et al.* Toward Stretchable Self-Powered Sensors Based on the Thermoelectric Response of PEDOT:PSS/Polyurethane Blends. *Adv. Funct. Mater.* **28**, 1704285 (2018).
95. Roth, B. *et al.* Mechanical Properties of a Library of Low-Band-Gap Polymers. *Chem. Mater.* **28**, 2363–2373 (2016).
96. Robeson, L. Historical Perspective of Advances in the Science and Technology of Polymer Blends. *Polym. 20734360* **6**, 1251–1265 (2014).
97. Utracki, L. A. Compatibilization of Polymer Blends. *Can. J. Chem. Eng.* **80**, 1008–1016 (2002).
98. *Nanostructured Polymer Blends*. (Elsevier, 2014).
99. Freudenberg, J., Jänsch, D., Hinkel, F. & Bunz, U. H. F. Immobilization Strategies for Organic Semiconducting Conjugated Polymers. *Chem. Rev.* **118**, 5598–5689 (2018).
100. Rumer, J. W. & McCulloch, I. Organic Photovoltaics: Crosslinking for Optimal Morphology and Stability. *Mater. Today* **18**, 425–435 (2015).
101. Kahle, F.-J., Saller, C., Köhler, A. & Strohriegl, P. Crosslinked Semiconductor Polymers for Photovoltaic Applications. *Adv. Energy Mater.* **7**, 1700306 (2017).
102. Chu, P.-H. *et al.* Synergistic Effect of Regioregular and Regiorandom Poly(3-hexylthiophene) Blends for High Performance Flexible Organic Field Effect Transistors. *Adv. Electron. Mater.* **2**, 1500384 (2016).
103. Kim, H. J. *et al.* Solution-Assembled Blends of Regioregularity-Controlled Polythiophenes for Coexistence of Mechanical Resilience and Electronic Performance. *ACS Appl. Mater. Interfaces* **9**, 14120–14128 (2017).
104. Savagatrup, S., Printz, A. D., Rodriquez, D. & Lipomi, D. J. Best of Both Worlds: Conjugated Polymers Exhibiting Good Photovoltaic Behavior and High Tensile Elasticity. *Macromolecules* **47**, 1981–1992 (2014).
105. Yau, C. P. *et al.* Investigation of Radical and Cationic Cross-Linking in High-Efficiency, Low Band Gap Solar Cell Polymers. *Adv. Energy Mater.* **5**, 1401228 (2015).
106. Kim, B. J., Miyamoto, Y., Ma, B. & Fréchet, J. M. J. Photocrosslinkable Polythiophenes for Efficient, Thermally Stable, Organic Photovoltaics. *Adv. Funct. Mater.* **19**, 2273–2281 (2009).
107. Carlé, J. E. *et al.* Comparative Studies of Photochemical Cross-Linking Methods for Stabilizing the Bulk Hetero-Junction Morphology in Polymer Solar Cells. *J. Mater. Chem.* **22**, 24417 (2012).
108. Griffini, G. *et al.* Long-Term Thermal Stability of High-Efficiency Polymer Solar Cells Based on Photocrosslinkable Donor-Acceptor Conjugated Polymers. *Adv. Mater.* **23**, 1660–1664 (2011).
109. Qian, D. *et al.* Stabilization of the Film Morphology in Polymer: Fullerene Heterojunction Solar Cells with Photocrosslinkable Bromine-Functionalized Low-Bandgap Copolymers. *J. Polym. Sci. Part Polym. Chem.* **51**, 3123–3131 (2013).
110. Chen, X., Chen, L. & Chen, Y. The Effect of Photocrosslinkable Groups on Thermal Stability of Bulk Heterojunction Solar Cells Based on Donor–Acceptor Conjugated Polymers. *J. Polym. Sci. Part Polym. Chem.* **51**, 4156–4166 (2013).
111. Arslan, M., Kiskan, B. & Yagci, Y. Post-Modification of Polybutadienes by Photoinduced Hydrogen Abstraction from Benzoxazines and Their Thermally Activated Curing. *Macromolecules* **49**, 5026–5032 (2016).
112. Clough, R. S. & Koenig, J. L. Solid-State Carbon-13 NMR Studies of Vulcanized Elastomers. VII. Sulfur-Vulcanized Cis-1,4 Polybutadiene at 75.5 Mhz. *Rubber Chem. Technol.* **62**, 908–927 (1989).

113. Sakdapipanich, J., Kowitteerawut, T., Seiichi, K. & Tanaka, Y. Structural Characterization of Highly Cis-1,4-polybutadiene: A Comparing Study in Swollen and Solid State Using NMR Technique. *Polym. Bull.* **46**, 479–485 (2001).
114. Cramer, N. B. & Bowman, C. N. Thiol–Ene Chemistry. in *Chemoselective and Bioorthogonal Ligation Reactions* 117–145 (John Wiley & Sons, Ltd, 2017). doi:10.1002/9783527683451.ch5
115. Mutlu, H. *et al.* Sulfur Chemistry in Polymer and Materials Science. *Macromol. Rapid Commun.* **40**, 1800650 (2019).
116. Machado, T. O., Sayer, C. & Araujo, P. H. H. Thiol-ene Polymerisation: A Promising Technique to Obtain Novel Biomaterials. *Eur. Polym. J.* **86**, 200–215 (2017).
117. Neindre, M. L. & Nicolaÿ, R. Polythiol copolymers with Precise Architectures: A Platform for Functional Materials. *Polym. Chem.* **5**, 4601–4611 (2014).
118. Lee, K.-S., Yeon, K. Y., Jung, K.-H. & Kim, S. K. Direct Observation of the Primary and Secondary C−Br Bond Cleavages from the 1,2-Dibromopropane Photodissociation at 234 and 265 nm Using the Velocity Map Ion Imaging Technique. *J. Phys. Chem. A* **112**, 9312–9317 (2008).
119. Lee, Y.-R., Chen, C.-C. & Lin, S.-M. Photodissociation of CH2Br2, 1,1- and 1,2-C2H4Br2 at 248 nm: A Simple C–Br Bond Fission Versus a Concerted Three-Body Formation. *J. Chem. Phys.* **118**, 10494–10501 (2003).
120. Tang, Y., Ji, L., Zhu, R., Wei, Z. & Zhang, B. Photodissociation Study of 1,3-Dibromopropane at 234 nm via an Ion Velocity Imaging Technique. *J. Phys. Chem. A* **109**, 11123–11126 (2005).
121. Krasovskiy, A. & Knochel, P. Convenient Titration Method for Organometallic Zinc, Magnesium, and Lanthanide- Reagents. *Synthesis* **2006**, 0890–0891 (2006).
122. Okamoto, K. & Luscombe, C. K. Simple Procedure for Mono- and Bis-End-Functionalization of Regioregular Poly(3-hexylthiophene)s Using Chalcogens. *Chem. Commun.* **50**, 5310–5312 (2014).
123. Spano, F. C. Modeling Disorder in Polymer Aggregates: The Optical Spectroscopy of Regioregular Poly(3-hexylthiophene) Thin Films. *J. Chem. Phys.* **122**, 234701 (2005).
124. Clark, J., Chang, J.-F., Spano, F. C., Friend, R. H. & Silva, C. Determining Exciton Bandwidth and Film Microstructure in Polythiophene Films Using Linear Absorption Spectroscopy. *Appl. Phys. Lett.* **94**, 163306 (2009).
125. Printz, A. D., Chiang, A. S.-C., Savagatrup, S. & Lipomi, D. J. Fatigue in Organic Semiconductors: Spectroscopic Evolution of Microstructure Due to Cyclic Loading in Poly(3-heptylthiophene). *Synth. Met.* **217**, 144–151 (2016).
126. Savagatrup, S. *et al.* Viability of Stretchable Poly(3-heptylthiophene) (P3HpT) for Organic Solar Cells and Field-Dffect Transistors. *Synth. Met.* **203**, 208–214 (2015).
127. Louarn, G. *et al.* Raman Spectroscopic Studies of Regioregular Poly(3-alkylthiophenes). *J. Phys. Chem.* **100**, 12532–12539 (1996).
128. Pingel, P. *et al.* Temperature-Resolved Local and Macroscopic Charge Carrier Transport in Thin P3HT Layers. *Adv. Funct. Mater.* **20**, 2286–2295 (2010).
129. Rekondo, A. *et al.* Catalyst-Free Room-Temperature Self-Healing Elastomers Based on Aromatic Disulfide Metathesis. *Mater. Horiz.* **1**, 237–240 (2014).
130. Deng, G. *et al.* Dynamic Hydrogels with an Environmental Adaptive Self-Healing Ability and Dual Responsive Sol–Gel Transitions. *ACS Macro Lett.* **1**, 275–279 (2012).
131. Fiore, G. L., Rowan, S. J. & Weder, C. Optically Healable Polymers. *Chem. Soc. Rev.* **42**, 7278–7288 (2013).
132. Fairbanks, B. D., Singh, S. P., Bowman, C. N. & Anseth, K. S. Photodegradable, Photoadaptable Hydrogels via Radical-Mediated Disulfide Fragmentation Reaction. *Macromolecules* **44**, 2444–2450 (2011).
133. Canadell, J., Goossens, H. & Klumperman, B. Self-Healing Materials Based on Disulfide Links. *Macromolecules* **44**, 2536–2541 (2011).

134. Yoon, J. A. *et al.* Self-Healing Polymer Films Based on Thiol–Disulfide Exchange Reactions and Self-Healing Kinetics Measured Using Atomic Force Microscopy. *Macromolecules* **45**, 142–149 (2012).
135. Pepels, M., Filot, I., Klumperman, B. & Goossens, H. Self-Healing Systems Based on Disulfide–thiol Exchange Reactions. *Polym. Chem.* **4**, 4955–4965 (2013).
136. Kloxin, C. J., Scott, T. F. & Bowman, C. N. Stress Relaxation via Addition–Fragmentation Chain Transfer in a Thiol-ene Photopolymerization. *Macromolecules* **42**, 2551–2556 (2009).
137. Yau, C. P. *et al.* Investigation of Radical and Cationic Cross-Linking in High-Efficiency, Low Band Gap Solar Cell Polymers. *Adv. Energy Mater.* **5**, 1401228 (2015).
138. Mueller, C. J., Klein, T., Gann, E., McNeill, C. R. & Thelakkat, M. Azido-Functionalized Thiophene as a Versatile Building Block to Cross-Link Low-Bandgap Polymers. *Macromolecules* **49**, 3749–3760 (2016).
139. Bäuerle, P., Würthner, F. & Heid, S. Facile Synthesis of 3-(ω-haloalkyl)thiophenes as Key Building Blocks for Functionalized Thiophenes and Polythiophenes. *Angew. Chem. Int. Ed. Engl.* **29**, 419–420 (1990).
140. Nguyen, H. T. *et al.* Synthesis and Characterization of Three-Arm Star-Shaped Conjugated Poly(3-hexylthiophene)s: Impact of the Core Structure on Optical Properties. *Polym. Int.* **64**, 1649–1659 (2015).
141. Yokoyama, A., Miyakoshi, R. & Yokozawa, T. Chain-Growth Polymerization for Poly(3-hexylthiophene) With a Defined Molecular Weight and a Low Polydispersity. *Macromolecules* **37**, 1169–1171 (2004).
142. Verswyvel, M., Goossens, K. & Koeckelberghs, G. Amphiphilic Chiral Block-Poly(thiophene)s: Tuning the Blocks. *Polym. Chem.* **4**, 5310–5320 (2013).
143. Hammer, B. A. G. *et al.* Reversible, Self Cross-Linking Nanowires from Thiol-Functionalized Polythiophene Diblock Copolymers. *ACS Appl. Mater. Interfaces* **6**, 7705–7711 (2014).
144. Sikari, R. *et al.* Achieving Nickel Catalyzed C–S Cross-Coupling under Mild Conditions Using Metal–Ligand Cooperativity. *J. Org. Chem.* **84**, 4072–4085 (2019).
145. Guo, F.-J. *et al.* C-S Cross-Coupling of Aryl Halides with Alkyl Thiols Catalyzed by In-Situ Generated Nickel(II) N-Heterocyclic Carbene Complexes. *Catal. Commun.* **96**, 11–14 (2017).
146. Venkanna, G. T., Arman, H. D. & Tonzetich, Z. J. Catalytic C–S Cross-Coupling Reactions Employing Ni Complexes of Pyrrole-Based Pincer Ligands. *ACS Catal.* **4**, 2941–2950 (2014).
147. Ishitobi, K. *et al.* Decarbonylative Aryl Thioether Synthesis by Ni Catalysis. *Chem. Lett.* **47**, 756–759 (2018).
148. Zhang, J., Medley, C. M., Krause, J. A. & Guan, H. Mechanistic Insights into C–S Cross-Coupling Reactions Catalyzed by Nickel Bis(phosphinite) Pincer Complexes. *Organometallics* **29**, 6393–6401 (2010).
149. Xu, X.-B., Liu, J., Zhang, J.-J., Wang, Y.-W. & Peng, Y. Nickel-Mediated Inter- and Intramolecular C–S Coupling of Thiols and Thioacetates with Aryl Iodides at Room Temperature. *Org. Lett.* **15**, 550–553 (2013).
150. Oderinde, M. S., Frenette, M., Robbins, D. W., Aquila, B. & Johannes, J. W. Photoredox Mediated Nickel Catalyzed Cross-Coupling of Thiols With Aryl and Heteroaryl Iodides via Thiyl Radicals. *J. Am. Chem. Soc.* **138**, 1760–1763 (2016).
151. Zhang, Y., Ngeow, K. C. & Ying, J. Y. The First N-Heterocyclic Carbene-Based Nickel Catalyst for C–S Coupling. *Org. Lett.* **9**, 3495–3498 (2007).
152. Smeets, A. *et al.* Incorporation of Different End Groups in Conjugated Polymers Using Functional Nickel Initiators. *Macromolecules* **42**, 7638–7641 (2009).
153. Luscombe, C. K., Proemmel, S., Huck, W. T. S., Holmes, A. B. & Fukushima, H. Synthesis of Supercritical Carbon Dioxide Soluble Perfluorinated Dendrons for Surface Modification. *J. Org. Chem.* **72**, 5505–5513 (2007).

154. Zhang, G. Q., Zhou, M. H., Ma, J. H. & Liang, B. R. Preparation and Swelling Properties of Solution Crosslinked Poly(cis-1,4-butadiene) Gels. *J. Appl. Polym. Sci.* **90**, 2241–2245 (2003).
155. Decker, C. Light-Induced Crosslinking Polymerization. *Polym. Int.* **51**, 1141–1150 (2002).
156. Decker, C. & Viet, T. N. T. Photocrosslinking of Functionalized Rubbers. X. Butadiene–Acrylonitrile Copolymers. *J. Appl. Polym. Sci.* **82**, 2204–2216 (2001).
157. Quagliano, J., Bocchio, J. & Ross, P. Mechanical and Swelling Properties of Hydroxyl-Terminated Polybutadiene-Based Polyurethane Elastomers. *JOM* **71**, 2097–2102 (2019).
158. Decker, C. & Viet, T. N. T. Photocrosslinking of Functionalized Rubbers, 7. Styrene-Butadiene Block Copolymers. *Macromol. Chem. Phys.* **200**, 358–367 (1999).
159. Decker, C. & Viet, T. N. T. Photocrosslinking of Functionalized Rubbers, 8. The Thiol-Polybutadiene System. *Macromol. Chem. Phys.* **200**, 1965–1974 (1999).
160. Decker, C. & Nguyen Thi Viet, T. Photocrosslinking of Functionalized Rubbers IX. Thiol-ene Polymerization of Styrene-Butadiene-Block-Copolymers. *Polymer* **41**, 3905–3912 (2000).
161. Balan, L., Melinte, V., Buruiana, T., Schneider, R. & Vidal, L. Controlling the Morphology of Gold Nanoparticles Synthesized Photochemically in a Polymer Matrix Through Photonic Parameters. *Nanotechnology* **23**, 415705 (2012).
162. Kline, R. J., McGehee, M. D., Kadnikova, E. N., Liu, J. & Fréchet, J. M. J. Controlling the Field-Effect Mobility of Regioregular Polythiophene by Changing the Molecular Weight. *Adv. Mater.* **15**, 1519–1522 (2003).
163. Alkhadra, M. A. *et al.* Quantifying the Fracture Behavior of Brittle and Ductile Thin Films of Semiconducting Polymers. *Chem. Mater.* **29**, 10139–10149 (2017).
164. Smith, Z. C. *et al.* Increased Toughness and Excellent Electronic Properties in Regioregular Random Copolymers of 3-Alkylthiophenes and Thiophene. *Adv. Electron. Mater.* **3**, 1600316 (2017).
165. Son, S. Y. *et al.* Exploiting π–π Stacking for Stretchable Semiconducting Polymers. *Macromolecules* **51**, 2572–2579 (2018).
166. Park, J. H., Kwon, O. J., Kim, T.-H., Mun, J. & Park, Y. D. Ultraviolet Irradiation Creates Morphological Order via Conformational Changes in Polythiophene Films. *Org. Electron.* **62**, 394–399 (2018).
167. Choi, H. H., Cho, K., Frisbie, C. D., Sirringhaus, H. & Podzorov, V. Critical Assessment of Charge Mobility Extraction in FETs. *Nat. Mater.* **17**, 2–7 (2017).
168. Song, E. *et al.* Stretchable and Transparent Organic Semiconducting Thin Film with Conjugated Polymer Nanowires Embedded in an Elastomeric Matrix. *Adv. Electron. Mater.* **2**, 1500250 (2016).
169. Spano, F. C., Clark, J., Silva, C. & Friend, R. H. Determining Exciton Coherence from the Photoluminescence Spectral Line Shape in Poly(3-hexylthiophene) Thin Films. *J. Chem. Phys.* **130**, 074904 (2009).
170. Kleinhenz, N. *et al.* Ordering of Poly(3-hexylthiophene) in Solutions and Films: Effects of Fiber Length and Grain Boundaries on Anisotropy and Mobility. *Chem. Mater.* **28**, 3905–3913 (2016).
171. Pereira, V. S., Leal, L. A., Ribeiro Junior, L. A. & Blawid, S. Inferring Changes in π-Stack Mobility Induced by Aging from Vibronic Transitions in Poly(3-hexylthiophene-2,5-diyl) Films. *Synth. Met.* **247**, 276–284 (2019).
172. O'Connor, B. T. *et al.* Morphological Origin of Charge Transport Anisotropy in Aligned Polythiophene Thin Films. *Adv. Funct. Mater.* **24**, 3422–3431 (2014).
173. Zhang, S. *et al.* Probing the Viscoelastic Property of Pseudo Free-Standing Conjugated Polymeric Thin Films. *Macromol. Rapid Commun.* **39**, 1800092 (2018).
174. Xue-Yan, T. *et al.* Effects of Concentration and Annealing on the Performance of Regioregular Poly(3-hexylthiophene) Field-Effect Transistors. *Chin. Phys. B* **18**, 3568 (2009).
175. Cho, S. *et al.* Thermal Annealing-Induced Enhancement of the Field-Effect Mobility of Regioregular Poly(3-hexylthiophene) Films. *J. Appl. Phys.* **100**, 114503 (2006).
176. *Conjugated Polymers: Properties, Processing, and Applications*. (CRC Press, 2019).

177. Hintz, H. *et al.* Photodegradation of P3HT–A Systematic Study of Environmental Factors. *Chem. Mater.* **23**, 145–154 (2011).